PLANETARY ATMOSPHERES RESEARCH PROJECT

Department of Earth & Atmospheric Sciences

Saint Louis University

EFFECTIVE MIE-SCATTERING AND CO_2-ABSORPTION IN THE DUST-LADEN MARTIAN ATMOSPHERE AND ITS IMPACT ON RADIATIVE-CONVECTIVE TEMPERATURE CHANGES IN THE LOWER SCALE HEIGHTS

by

Albert J. Pallmann

Sponsored by NASA under Grant No. NGR 26-006-042

PLATMOS Research Report No. 10

MARCH 1976

Title:	Effective Mie-Scattering and CO_2-Absorption in the Dust-Laden Martian Atmosphere and Its Impact on Radiative-Convective Temperature Changes in the Lower Scale Heights
Report Date:	March 1976
Author:	A. J. Pallmann
Performing Organization Report No.:	PLATMOS Research Rpt. #10
Performing Organization Name and Address:	Saint Louis University 221 N. Grand Saint Louis, Missouri 63103
Grant No.:	NGR 26-006-042-2
Sponsoring Agency Name and Address:	National Aeronautics and Space Administration Washington, D. C. 20546
Type of Report:	Contractor Report (Final) covering the Period December 1974-March 1976

Supplementary Notes:

This report presents further findings developed in continuation of research effort of several years, sponsored by NASA. See Contractor Report CR-2318.

ABSTRACT

A time-dependent computer model of radiative-convective-conductive heat transfer in the Martian ground-atmosphere (G-A) system was refined by incorporating an intermediate line strength CO_2 band absorption which together with the strong- and weak-line approximation closely simulated the radiative transmission through a vertically inhomogeneous stratification. About 33,000 CO_2 lines were processed to cover the spectral range of solar and planetary radiation. Effective absorption by silicate dust particulates, with height-dependent polydisperse concentration functions, was built into the model to study the impact of dust on the ground-atmosphere temperature field as a function of time.

This model was subsequently attuned to IRIS, IR-radiometric and S-band occultation data for representative dates during the time period November 1971 through February 1972. Very satisfactory simulations of the measured Iris spectra were accomplished for the dust-free condition. In the case of variable dust-loads, the simulations turned out to be sufficiently fair such that some inferences into the effect of dust on temperature were justified.

The numerical model simulated at high spatial and temporal resolution (52 atmospheric and 30 subsurface levels; with time-steps between 4 and 10 min) the heat transports in the G-A system. The algorithm was based on the solution of the radiative transfer and enthalpy rate equations. Ground and atmosphere were coupled by an internal thermal boundary condition.

Basic findings were that high-resolution temperature soundings and their diurnal histories, generated by the attuned model, serve to adjust IRIS-inverted and S-band occultation-inverted temperature soundings together with IR-radiometric data.

Key Words (Suggested by Author)

- Martian Atmosphere
- Dust-laden Atmosphere
- Radiative-Convective Heat Transfer
- Ground-Atmosphere Interface Energetics
- Simulation attuned to Satellite Data

LIST OF FIGURES AND TABLES

Page

TABLE OF CONTENTS

FOREWARD AND ACKNOWLEDGEMENTS

This is a final report of a fifteen-month research sponsored by the Planetary Atmospheres Program, Office of Space Science, NASA Headquarters, under grant No. NGR 26-006-042. The author is indebted to Dr. Robert F. Fellows, Chief of Planetary Atmospheres, NASA, who served as the technical officer for this grant.

By refining an existing computer model and attuning it to Mariner 9 data, an investigative tool of quantitative simulation was available to generate a host of time-dependent information which serves to re-interpret IRIS, IRR and S-band occultation data.

The author wishes to express his gratitude to Dr. R. A. McClatchey of AFCRL Optical Physics Laboratories for making a tape of absorption line data available. Very special thanks are due to Mr. Harvey Ferdman, my research assistant who saw to it with unusual dedication and persistence thatthe project was brought to a successful completion. Mr. Eric Bram's assistance in scientific computing is greatfully acknowledged. Last but not least, the author is thankful for Mrs. Fran Brummell's typing and other secretarial help.

1.0 INTRODUCTION

In a previous study, the feasibility of reinterpreting Mariner 9 IRIS data by a radiative-convective-conductive transfer (R.C.C.T.) model was demonstrated for the case of a dust-laden Martian atmosphere (Pallmann, 1974). The findings of this modeling effort stimulated the proposal of an extended investigation into attuning the R.C.C.T. model to several modes of Mariner 9 data such as the IR-radiometric and the S-band occultation data together with the IRIS measurements.

Various refinements of the CO_2-transmission function were envisioned, attunable to the prevailing atmospheric conditions on Mars. Based on recent developments of the computational treatment of radiative transfer in Mie-scattering and absorbing planetary atmospheres (Canosa and Penafiel, 1973: Dave and Canosa, 1974; Dave, 1975) an improved algorithm was incorporated into the R.C.C.T. model in order to represent the effective absorption of radiative energy by the silicate particulates during the major dust storm of 1971 (Martin, 1974). Various components of the dust algorithm were quantitatively adjusted to the findings of Conrath (1974) and the simulations of polydispersions offered by Deirmendjian (1969).

An additional computer program, labeled "FLUXOUT", generated the numerical values of the upwardly directed

hemispherical flux at the top of the atmosphere, of the thermal emissions from the ground surface and all atmospheric layers, after due transmission through the intervening layers, within the spectral range 200-2,000 cm^{-1}.

A particular subroutine for convective heat transport was incorporated into the R.C.C.T. model with the provision that wherever the vertical transfer of (solar and planetary) radiative energy generated a superadiabatic lapse rate, the excess enthalpy was transported upward into the next higher layer. This process repeated itself until a zero-gradient of potential temperature was established in all layers involved in convective overturn.

The National Space Science Date Center (G.S.F.C., Greenbelt, Md.) provided the specific data sets of the IRIS, IR-Radiometry, and S-band occultation measurements. Magnetic tapes and microfilms were made available from which the particular dates were retrieved. The project utilized the rather unique occasion that the Mariner 9 experiments monitored Mars during three consecutive periods, i.e., (a) when the planet was enshrouded by dust, (b) in the transitional phase, and (c) after clearing. By running backward in time, the expanded computer model was attuned to Mariner 9 data first under dust-free conditions. Once this attunement was achieved, extrapolation into the transitional and fully dust-laden phases followed.

The basic objective of the investigation, reported herein, is to attune an expanded radiative-conductive-convective heat transfer model of the (CO_2 and dust) absorbing and scattering Martian atmosphere to IRIS, IRR, and S-band occultation data, individually and concertedly, for the purpose of generating highly time-dependent atmospheric and subsurface temperature soundings. These sets of tautochrones provided the basis for a reinterpretation of the aforementioned data as they permit to approximate the vertical temperature distribution on Mars.

A second objective is to contribute toward elucidating the interaction of Martian dust-aerosol and thermal energy transfer processes.

2.0 ANALYTICS OF RADIATIVE TRANSFER IN A MIE-SCATTERING AND ABSORBING MARTIAN ATMOSPHERE

2.1 BASIC CONSIDERATIONS

For the transfer of radiative energy through a planetary atmosphere with vertically heterogeneous dust distribution, the physical processes of interest are the (particulate and molecular) absorption and multiple Mie-scattering of down- and upwardly directed solar radiative flux and the absorption, scattering and emission of Martian atmospheric and surface heat radiation under the condition of a given inhomogeneous stratification of aerosol and gases.

In order to determine how the thermal structure on the planet Mars is modified by a given aeolian particulate load, one must compute the flux divergence for a specified number of layers, in atmosphere and soil, and a wide spectral range which includes both short- and long-wave radiation. Although the solution of the radiative transfer equation for a specific atmosphere is principally known (Chandrasekhar, 1960; Sekera, 1963a, b; Deirmendjian, 1965),the problem of computing-time economy arises. The exploration of the radiation field to any degree of completeness and accuracy would lead to an unacceptably large computational load (Braslau and Dave, 1973a, b).

Recently, Canosa and Penafiel (1973) have shown that the spherical harmonics approximation to the radiative transfer equation represents a highly efficient method of numerically solving the transport problem for atmospheric models with highly anisotropic phase functions. The essential limitation in this approach is the restriction to homogeneous atmospheres. In 1974, Dave and Canosa discussed a direct solution of the transfer equation for heterogeneous atmospheres by the spherical harmonics approximation. They applied this method to atmospheric models with arbitrary vertical inhomogeneities due to variations in the scattering and absorption characteristics of the atmospheric constituents. In their formulation, the spherical harmonics equations represent a two-point boundary value problem for a system of first-order, linear differential equations with variable coefficients. Through an extensive study, these analytics have been adapted to the needs of our project.

2.2 GENERAL MATHEMATICAL FORMULATION

In the two-point boundary value problem, Dave and Canosa (1974) introduced as independent variable the optical depth, measured from the top of the atmosphere, in the form of a linear combination of three distinct optical depths, i.e.,

$$\tau = \tau^{(s,r)} + \tau^{(s,m)} + \tau^{(a,m)} + \tau^{(a)} \qquad (1)$$

The normal Rayleigh-scattering optical depth $\tau^{(s,r)}$ at any atmospheric level can be taken to be proportional to the pressure at that level. Values of this optical depth at the bottom of the atmosphere, $\tau_b^{(s,r)}$, are given by Howard et alii (1961). Values of the Mie-scattering and particle-absorption optical depths, $\tau^{(s,m)}$ and $\tau^{(a,m)}$ respectively, can be obtained by following Deirmendjian's procedure (1969). Details for computing values of the CO_2-gas optical depth $\tau^{(a)}$, pertaining to the Martian atmosphere, have been developed previously (Pallmann, 1968· Pallmann et alii, 1973). Obviously, the optical depth is highly wave-number dependent.

The appropriate starting equation of radiative transfer for a general phase function,

$$p(\cos\Theta) = \sum_{\ell=0}^{L} \omega_\ell P_\ell(\cos\Theta) \tag{2}$$

is offered by Chandrasekhar (1960, on page 150, eq. 92) with m = o (average intensity $I^{(o)}$) and making the coefficients ω_ℓ in the Legendre polynomials series expansion in eq. (2) space-dependent. The average intensity is expanded in another finite series of Legendre polynomials with (L + 1) terms, i.e.

$$I^{(o)}(\tau,\mu) = \sum_{\ell=0}^{L} \frac{2\ell+1}{2} f_\ell(\tau) P_\ell(\mu) \tag{3}$$

with f_ℓ being the Legendre moment

$$f_\ell(\tau) = \int_{-1}^{+1} I^{(0)}(\tau,\mu)\, P_\ell(\mu)\, d\mu \tag{4}$$

and μ representing the cosine of the zenith angle measured with respect to the positive t-axis (inward normal!). By utilizing the orthogonality property of Legendre polynomials, i.e.,

$$\int_{-1}^{+1} P_\ell(\mu')\, P_n(\mu')\, d\mu' = \begin{cases} \frac{2}{2\ell+1} & \text{for } \ell = n \\ 0 & \text{for } \ell \neq n \end{cases} \tag{5}$$

one obtains an intermediate form of the transfer equation which if multiplied successively by the Legendre polynomials $P_\ell(\mu)$, with $\ell = 0, 1, \ldots L$, and integrated over $-1 \leq \mu \leq 1$, yields the spherical harmonics equations. In matrix notion, they can be written as

$$\mathbf{A}\frac{d\mathbf{f}(\tau)}{d\tau} + \mathbf{C}(\tau)\,\mathbf{f}(\tau) = \mathbf{S}(\tau) \tag{6}$$

The appropriate boundary conditions were developed by Marshak (1947) and have the form

$$\mathbf{f}^{(0)}_{odd} = -\,\mathbf{G}\,\mathbf{f}^{(0)}_{even}$$

$$\mathbf{f}^{(\tau_\ell)}_{odd} = +\,\mathbf{G}\,\mathbf{f}^{(\tau_\ell)}_{even} \tag{7}$$

Dave and Canosa (1974) offer an explicit discussion of these expressions in the Appendix A of their paper. In addition, they explain in the main text of their paper what the bold-face letters in eq. (6) signify. For convenience, they are restated here:

$$(8)\quad \mathbf{A} \equiv \begin{bmatrix} 0 & 1 & & & & 0 & 0 \\ 1/3 & 0 & 2/3 & 0 & & & 0 \\ 0 & 2/5 & 0 & 3/5 & & & \\ \cdot & \cdot & \cdot & \cdot & & & \cdot \\ 0 & & & & \frac{L-1}{2L-1} & 0 & \frac{L}{2L-1} \\ 0 & 0 & & \cdot & & \frac{L}{2L+1} & 0 \end{bmatrix}$$

$$\mathbf{C}(\tau) = \begin{bmatrix} \sigma_0(\tau) & 0 & & 0 \\ 0 & \sigma_1(\tau) & & \\ & & & \\ 0 & & & \sigma_L(\tau) \end{bmatrix}; \quad \mathbf{f}(\tau) = \begin{bmatrix} f_0(\tau) \\ f_1(\tau) \\ \cdot \\ \cdot \\ f_L(\tau) \end{bmatrix}; \quad \mathbf{S}(\tau) = \begin{bmatrix} S_0(\tau) \\ S_1(\tau) \\ \vdots \\ S_L(\tau) \end{bmatrix}$$

with

$$\sigma_\ell(\tau) \equiv 1 - \frac{1}{2\ell+1}\omega_\ell(\tau); \quad S_\ell(\tau) \equiv \frac{1}{4} F e^{-\tau/\mu_0} P_\ell(\mu_0) \frac{2}{2\ell+1} \omega_\ell(\tau)$$

and (πF) being the flux of a beam of solar radiation, per unit area normal to it, incident at the top of the plane-parallel atmosphere in the specified direction (μ_0, φ_0) as stated by Chandrasekhar (1960, p. 20, 145, 161, 216).

The spherical harmonics equations (6) and (7) can be transformed by the finite difference method into an

equivalent algebraic problem which is particularly suited to treat transfer in nonhomogeneous atmospheres (see also Dave, 1975a, b). It is worthwhile to mention that the adoption of vertical heterogeneity poses additional problems which are not taken care of by just assuming the atmosphere to be divisible into a given number of layers each with constant radiative properties. In their aforementioned paper, Dave and Canosa emphasize that their algebraic problem is essentially different from that presented by Canosa and Penafiel (1973) although the method of solution is almost identical.

Considering some of the computational aspects, Dave and Canosa discuss the spatial structure of the model atmosphere which is very similar to that adopted earlier in our research project. The upper-limit parameter L in the series of eqs. (2) and (3) is prescribed in practice through the numerical evaluation of the magnitude of $\sigma_\ell(\tau)$ in the $\mathbf{C}(\tau)$ matrix. If dust is absent $\sigma_\ell=1$ for all $\ell>2$. Continuity of the column vectors $\mathbf{f}$ is assured by choosing L odd (or equal to 3 for dust-free conditions).

By inspecting eq. (3) above, one realizes on the one hand that a very small number for L introduces strong oscillations which are not realistic. On the other hand, a large numerical value for L will substantially enhance the computer time. Time calculations have been made which

permitted to optimize the problem. It is helpful to recognize that the spherical harmonics method is far less dissipative in nature than the iterative scheme for the transfer equation.

2.3 SPECIFIC ANALYTICS OF A LOW-COST SIMULATION

Chandrasekhar (1960; sec. 2.2) defined the downward and upward diffuse fluxes at a level τ_n, which we adjusted to the condition of the normal pointing downward, i.e.,

$$F_d(\tau_n) = 2\pi \int_0^1 I^{(0)}(\tau_n; +\mu)\, \mu\, d\mu \tag{9}$$

and

$$F_u(\tau_n) = 2\pi \int_{-1}^{0} I^{(0)}(\tau_n; -\mu)\, \mu\, d\mu \,. \tag{10}$$

The expressions indicate that these two flux functions which determine the spectral net flux at the level τ_n can be found by just computing the azimuth-independent $I^{(0)}$. This is an important simplification for any simulation procedure directed toward the determination of the net flux divergence and, finally, the time-rate of change of temperature at given levels τ_n.

A numerical value for the parameter L was adopted. i.e., L=11. Although this might seem to be rather oscillatory, it is through the integration in the flux expressions (9) and (10) that a smoothing process is applied. A systematic smoothing technique is available for various types of scattering (Kourganoff, 1952; Dave and Armstrong, 1974), which was not adopted in this project.

Since the Dave-Canosa algorithm permits to treat heterogeneous conditions, the actual computation of the solution to the algebraic problem (Dave and Canosa's eq. (13), 1974) is a much more involved problem. The numerical computation is unstable against the accumulation of round-off errors. The instability can be eliminated by carrying out stabilizing transformations on the matrix and vector sequences, involved in the algebraic system, at several conditioning points. Its number was chosen to be $N_c \leq \frac{\tau_b \cdot (L+1)}{10} + 3$. With $L = 11$ and $0 < \tau_b < 3$, the number N_c of conditioning points ranged between 3 and 6.

The specific analytics for a low-cost simulation were

$$I^{(0)}(\tau,\mu) = \sum_{\ell=0}^{11} \frac{2\ell+1}{2} f_\ell(\tau) P_\ell(\mu) \tag{11}$$

as the azimuth-independent spectral radiance,

$$F_d(\tau) = 2\pi \sum_{\ell=0}^{11} \frac{2\ell+1}{2} f_\ell(\tau) \int_0^1 \mu P_\ell(\mu) d\mu \tag{12}$$

as the spectral downward flux, and

$$F_u(\tau) = 2\pi \sum_{\ell=0}^{11} \frac{2\ell+1}{2} f_\ell(\tau) \int_{-1}^0 \mu P_\ell(\mu) d\mu \tag{13}$$

as the spectral upward flux. Marshak's boundary conditions,

as discussed by Dave and Canosa (1974; Appendix A), can readily be specified for $L = 11$.

Computer time estimates indicate that for $L = 11$, the spherical harmonics approximation is one to two orders of magnitude faster on the equivalent of an IBM 360 computing system, model 195 with FORTRAN-H compiler, than the Gauss-Seidel iterative technique. A single precision generates numerical results accurate to the first 4 figures. Incorporating this algorithm into our RCCT-model and running the enhanced program to generate, over a period of 24 Martian hours, 192 temperature soundings require several hours of computer time.

3.0 REFINEMENT OF TRANSMISSION FUNCTIONS IN "FLUX-OUT" AND "MARSTEMP" PROGRAMS

Continued work with the CO_2-absorption-line data, compiled by McClatchey et alii (1973), facilitated an essential improvement of the quasi-random CO_2-transmission function in both the FLUX-OUT (F/O) and MARSTEMP (M/T) programs. It was found that band transmission modeling was superior to single-line approximation because of the well-known difficulties in line-overlapping, - asymmetry, and - shape factor (Kondratyev, 1965, 1969; Goody, 1964). Consequently, an appropriate simulation of band absorption for Martian-atmospheric CO_2 was computerized (sect. 3.1). An improved absorption capability was modeled which better represented intermediate line-intensities (sect. 3.2). Temperature- and pressure dependence of half-width, line intensity, and shape factor found renewed attention (sect. 3.3) as well as the computational arrangement of spectral increments (sect. 3.4). Finally, the proper fitting of the band model to gaseous absorption was made utilizing the measurements of the Mariner 9 IRIS and IRR experiments (sect. 3.5).

3.1 BAND ABSORPTION MODEL

Goody (1964) has offered a rather detailed discussion on absorption band models. For computing numerical problems, it is desirable to develop averaging techniques which smooth over the finest structure in the bands without distorting the

band contour. Previously, we used the Ladenberg and Reiche (L-R) function as the basic mathematical form for CO_2 absorption. Since we adopted a quasi-random model (Pallmann et alii, 1973), the L-R function appeared in the negative argument of an exponential function representing the transmission function.

More recently, it was found that this type of transmission function does not optimally represent transfer of radiative energy under Martian atmospheric conditions since it does not take care of the many weak lines present. In order to correct for this shortcoming, another transmission function was adopted which made allowance for independent lines of unequal intensity and many weak lines before the strong-line region was reached.

Basically, the analytical form of this transmission function is derived as follows:

Assume a given wave-number range of N lines and each of these N lines as one member of an infinite array of randomly spaced lines. Let p(S).dS be the probability that a line has an intensity between S and (S + dS). The adopted distribution function is

(14) $$p(S) = \frac{K}{S} \qquad \text{for } S \leq S'.$$

The cumulative probability of lines with intensity greater than S is

(15) $$\int_{S}^{S'} p(S)\,dS = K \log\left(\frac{S'}{S}\right)$$

Laboratory measurements have indicated that eq. (15) is fairly well satisfied. This indicates that the expression (14) accommodates a large number of weak lines (Godson, 1954).

The statistically averaged absorption function reads

$$\bar{A}(u;\Delta n \mid p(S)=\frac{K}{S}) = \frac{2\pi\alpha K}{d}\left[e^{-u}\cdot I_0(u)+2ue^{-u}\left\{I_0(u)+I_1(u)\right\}-1\right] \tag{16}$$

for the Lorentz-line shape and (α) being half-width, $u = \frac{\tilde{S}.\tilde{a}}{2\pi\alpha}$ ($\tilde{a}$: amount of absorber mass), and $\Delta n = 5\ cm^{-1}$. The designations I_o and I_1 stand for the zeroth and first order Bessel functions of the first kind with imaginary arguments.

The mean transmission function averaged over N superposed arrays of lines is

$$\bar{\tau} = \exp\left\{-\bar{A}\right\} \tag{17}$$

The restriction due to the Lorenz line shape is discussed in Sec. 3.3.

3.2 MODELING INTERMEDIATE-LINE ABSORPTION

The quasi-random transmission function, as given by eqs. (16) and (17), has two asymptotes, i.e., the weak-line and the strong-line approximations, for small and large u-values, respectively. Previously, we used this dual approach

to model the whole u-range. A threshold value for u was prescribed, and the computer determined which approximation to use. Goody (1964; sects. 4.2.1) demonstrated by means of the Matheson diagram that the intermediate u-range suffers fairly large inaccuracies.

In applying this line of arguing to Martian atmospheric conditions, we decided that the intermediate range from 0.05 to 50.0, of optical path for the line centers needed further attention. In eq. (16), the modified Bessel functions with imaginary argument lent themselves to a direct numerical evaluation. Lewin and Grosberg (1952) offer a series expansion for this type of Bessel function, i.e.,

$$I_p(x) = i^{-p} J_p(ix) = \sum_{k=0}^{\infty} \frac{\left(\frac{x}{2}\right)^{2k+p}}{k!\,\Gamma(k+p+1)} \tag{18}$$

with

i: imaginary unit $\sqrt{-1}$

Γ: gamma function

Particularly, one obtains for the zeroth order function

$$I_0(x) = \sum_{k=0}^{\infty} \frac{\left(\frac{x}{2}\right)^{2k}}{(k!)^2} \tag{19}$$

Klerer and Korn (1967) have given a numerical approximation combined with estimates for the truncation error.

Computer runs were made for the purpose of determining the optimal form of representation of I_o and I_1 in the transmission function. Acceptable forms were used first in our F/O-program for dust-free conditions. The simulation of the IRIS spectra was quite satisfactory. It was inferred that the former combination of weak-/strong-line absorption only was an insufficient means of representing CO_2 band absorption. The intermediate-line representation appeared to be a necessary refinement without which rather large differences between measurement and simulation of the IRIS spectra occurred.

The subsequent incorporation of the intermediate-line absorption capability of the interval $0.05 \leq u \leq 50.0$, into the M/T-program is considered to be one essential procedure in the attunement of the model to Mariner 9 data.

3.3 TEMPERATURE AND PRESSURE DEPENDENCE OF LINE INTENSITY, HALF-WIDTH AND SHAPE FACTOR

In McClatchey's absorption data compilation, the line intensity $S(T_s)$ is given for all known CO_2 lines and T_s=296K. Without the induced emission term, the temperature-dependent line intensity S(T) at temperature T reads

$$S(T) = \frac{S(T_s)\, Q_v(T_s)\, Q_r(T_s)}{Q_v(T)\, Q_r(T)} \times \left[\exp\left\{ + \frac{1.4388\, E''(T-T_s)}{T \cdot T_s} \right\} \right] \qquad (20)$$

with

E": energy in cm^{-1} of the lower state of transition,

Q_v, Q_r: vibrational and rotational partition functions, respectively.

Numerical information about the vibrational and rotational partition functions of CO_2 (isotope 6-2-6) has been provided by McClatchey et alii (1973; Table 2). In addition, Goody (1964) has discussed some aspects surrounding the rotational partition function (in his sect. 3.2). On the basis of these discussions, it can be shown that eq. (20) may be replaced by

$$S(T) = S(T_s)\frac{T}{T_s}\left[\exp\left\{\frac{1.4388\,E''(T-T_s)}{T.T_s}\right\}\right] \qquad (21)$$

This formula was subsequently used to compute integrated line intensities S for CO_2 at given temperatures T. Expression (20) indicates that S does not depend on pressure.

The line half-width at half maximum, , depends on both temperature and pressure. McClatchey et alii (1973) suggest the following relationship,

$$\alpha(p,T) = \alpha_s \frac{p}{p_s}\sqrt{\frac{T_s}{T}} \qquad (22)$$

with

T_s = 296K; p_s = 1 atm; and α_s: Lorentz line with at standard

conditions. Although the temperature dependence T_s/T is not certain, measurements made with a CO_2 laser (Ely and McCubbin, 1970) indicate a linear factor (T_s/T) for the P20-line of the 10.4 μm CO_2 band.

Concerning the line shape, some uncertainty exists. In the aforementioned absorption line compilation, the Lorentz shape was used. Due to Goody (1964), the spectral absorption coefficient can be expressed by

$$k(n) = S \cdot f_L(n-n_o) = \frac{S \cdot \alpha_L}{\pi\left[(n-n_o)^2 + \alpha_L^2\right]} \tag{23}$$

where the Lorentz shape factor f_L is normalized, i.e.

$$\int f_L(n-n_o)\,d(n-n_o) = 1 \tag{24}$$

with n: wave-number, cm^{-1}.

The true line shape is not always given by the Lorentz shape which depends on pressure as discussed above. For Martian atmospheric pressures of less than 10 mb, the Doppler line shape is not negligible. The Doppler effect is associated with molecular thermal motion. If an absorbing or emitting molecule has a velocity component w in the line of sight, a frequency shift $\Delta n = \frac{w}{c} \cdot n_o$ about n_o is generated. As a consequence, the Doppler line shape adopts the form

$$f_D(n-n_o) = \frac{1}{\alpha_D\sqrt{\pi}} \exp\left\{-\left(\frac{n-n_o}{\alpha_D}\right)^2\right\} \tag{25}$$

with the Doppler line width being

$$\alpha_D = \frac{n_o}{c}\left(\frac{2kT}{m}\right)^{1/2} \quad \text{in } cm^{-1}. \tag{26}$$

Calculations with numerical values, typical for Martian conditions, indicate that the Doppler width has about equal footing with the Lorentz width in the lower atmosphere gaining gradually with elevation. This is indicative of a combined Lorentz and Doppler broadening. Nevertheless, we have decided against the usage of such a combination since due to Goody (1964) the mixed Doppler and Lorentz line shape is too complex for analytical solution. Furthermore, the far wings of a line are always influenced by molecular collisions; if the absorbing path is long enough absorption will finally be controlled by the line-wing profile. Consequently the absorption will be given by eq. (16).

Recently, it was pointed out by Rodgers (1976) that if both Doppler and collision broadening are significant the detailed line shape depends on the nature of the collisions. For most atmospheric gases, the Voigt line shape is adequate. Assuming that the two broadening processes are uncorrelated, one averages the Doppler shifted Lorentz lines weighted with the distribution of velocities. As a result, one obtains a convolution of the Doppler and Lorentz shapes, i.e.,

$$f_\nu(n') \propto \int_{-\infty}^{+\infty} \frac{e^{-n^2/\alpha_D^2}}{(n-n'+n_o)^2+\alpha_L^2}\,dn \tag{27}$$

For the numerical evaluation of the Voigt profile, see Kielkopf (1973). It is planned to accommodate this profile in the near future although no efficient numerical approximation exists.

3.4 ARRANGEMENT OF SPECTRAL INCREMENTS

The numerical treatment of the random transmission function (see eq. (17)) requires each time an appropriate averaging procedure for N lines taken from the CO_2 absorption bands. Since the project has been utilizing the McClatchey data compilation (1973), we had to accommodate about 9,900 lines in the far infrared between 200 and 2,000 cm^{-1} and about 22,700 lines in the near infrared between 2,000 and 10,000 cm^{-1}.

The F/O-program which simulates the upwelling thermal flux at the top of the atmosphere, advantageously operated with a spectral increment of 5 cm^{-1}. However the M/T program needed a more economical structure for these intervals because of the frequent iterations inherent in the time integration (of more than 144 time steps/day). After a careful inspection of the absorption line data, it was found that grouping of CO_2 lines in intervals of variable length, generally between 20 and 50 cm^{-1} was feasible if "lopsided" crowding of lines near either boundary was avoided. The new array consists of 140 spectral increments appropriately covering the near and far infrared.

Instead of the former spectral parameters, which were based on the Stull, Wyatt and Plass (1963) data and calculated

by Prabhakara and Hogan (1965), a new set of parameters were analytically developed and numerically determined. The data base for this set was found in the McClatchey compilation. From eq. (16) and the respective expressions for strong- and weak-line approximations, one obtains in accordance with Goody's procedure (1964)

$$u = \frac{2a}{\pi}\left(\frac{\sum_{i=1}^{N} S(i)}{\sum_{i=1}^{N}\sqrt{S(i)\alpha(i)}}\right)^2 \tag{28}$$

and

$$y = \frac{K\alpha_L}{d} = \frac{K}{4\Delta n}\cdot\frac{\left(\sum_{i=1}^{N}\sqrt{S(i)\cdot\alpha(i)}\right)^2}{\sum_{i=1}^{N} S(i)} \tag{29}$$

with $\Delta n = Nd$ the width of the spectral increment, N the number of lines, and d the average spacing . By inserting eqs. (21) and (22), we arrive at

$$u = 4a\left(\frac{T}{T_s}\right)^{3/2}\cdot\left[\frac{p_s}{2\pi}\cdot\left(\frac{\sum_{i=1}^{N} S_o'(i)\exp\left\{\Gamma_i'\left(\frac{1}{T_o}-\frac{1}{T}\right)\right\}}{\sum_{i=1}^{N}\sqrt{S_o'(i)\exp\left\{\Gamma_i'\left(\frac{1}{T_o}-\frac{1}{T}\right)\right\}\alpha_o(i)}}\right)^2\right]\cdot\frac{1.66}{1.3\cdot p} \tag{30}$$

and

$$(31)\quad y = \frac{K}{8\pi}\cdot\left(\frac{T_s}{T}\right)^{1/2}\cdot 1.3p\left[\frac{2\pi}{\Delta n\cdot p_s}\cdot\frac{\left(\sum_{i=1}^{N}\sqrt{S_o'(i)\exp\left\{\Gamma_i\left(\frac{1}{T_o}-\frac{1}{T}\right)\right\}\alpha_o(i)}\right)^2}{\sum_{i=1}^{N}S_o'(i)\exp\left\{\Gamma_i\left(\frac{1}{T_o}-\frac{1}{T}\right)\right\}}\right]$$

S_o: line intensity at standard pressure p_s = 1 atm and temperature T_s = 296°K, in cm^{-1}/molecule.cm^{-2}, as presented in McClatchey compilation;

α_o: Lorentz line width parameter at p_s, T_s, in cm^{-1}/atm; and

Γ_i: =1.4388.E", energy of the lower molecular state in cm^{-1}.

The temperature factor $(T_s=/T)^{1/2}$ represents the dependence of α on T in eqs. (31) and (30). The additional ratio (T/T_s) is derived from the temperature-dependent expression for the line intensity (see sect. 3.3; eq. (20) and (22)).

The summations over the index "i" in eqs. (30) and (31) would represent a formidable task of computing if they are an integral part of the time-dependent M/T (or the F/0) program. Since these terms are exclusively temperature-dependent with the $S_o'(i)$ and $\alpha_o(i)$ to be read in from the McClatchey compilation, they were submitted to a polynomial approximation. Such a procedure admits a numerical computation, separate from the main program. Subsequently, the approximated terms were stored on tape to be called in to the central processing unit whenever needed.

For convenience, the terms in question are relabeled as

$$F_{o,i} = \sum_{j=1}^{N} \left[S'_{o,j} \exp\left\{ 1.4388 \cdot E2_j \cdot \left(T_s^{-1} - T^{-1} \right) \right\} \right] \tag{32}$$

and

$$G_{o,i} = \left[\sum_{j=1}^{N} \sqrt{ S_{o,j} \cdot \alpha_{o,j} \cdot \exp\left\{ 1.4388 \cdot E2_j \cdot \left(T_s^{-1} - T^{-1} \right) \right\} } \right]^2 \tag{33}$$

where the symbols signify the same variables as before. These two functions were numerically evaluated for all wavenumber increments which have the index "i" for computational convenience. (This was a re-indexing.) Obviously, the values of $F_{o,i}$ and $G_{o,i}$ are not only different for each wavenumber interval, they are also temperature-dependent.

The method of approximating by polynomials was determined as follows:

- Generate a second-order polynomial, dependent on temperature, to approximate $\ln\left(F_{o,i}\right)$ and $\ln\left(G_{o,i}\right)$.
- Find for all Martian temperatures from 140°K to 320°K and for each interval "i", $A \equiv \ln\left(F_{o,i}\right)$ and $BS \equiv \ln\left(G_{o,i}\right)$.

The data for all CO_2-lines in a particular i-segment were read-in each time from the McClatchey tape. The program-run produced for M/T 137 segment values, and for F/O 171 segments, of both $\ln\left(F_{o,i}\right)$ and $\ln\left(G_{o,i}\right)$.

Subsequently, second-degree polynomials P(x) were fitted to both $\ln(F_{o,i})$ and $\ln(G_{o,i})$ with the independent variable x in this case being $1.4388\cdot(T_s^{-1} - T^{-1})$. All numerical values of these logarithmic functions were written in disk file for both the M/T and the F/O programs. With the specific form for P(x) being

$$P(x) = a + bx + cx^2 \tag{34}$$

the functions $F_{o,i}$ and $G_{o,i}$ are approximated by

$$F_{o,i} \quad \text{or} \quad G_{o,i} = \exp\{P(x)\} \tag{35}$$

for all spectral increments of index "i".

In order to test the accuracy of the polynomial approximation, the expressions

$$\text{MAX}\left[\frac{\exp\{P(x)\}}{\exp y}\right] \quad \text{or} \quad \text{MAX}\left[\frac{\exp y}{\exp\{P(x)\}}\right] \tag{36}$$

were calculated and printed for all spectral increments and temperatures in the range $140\text{K} \leqslant T \leqslant 320\text{K}$, with y being either $\ln(F_{o,i})$ or $\ln(G_{o,i})$. The numerical values of the MAX-parameters average about 3%. The largest values usually occur at very low or very high temperatures which in turn appear rather infrequently in the Martian temperature profiles. Therefore, it was concluded that the polynomials P(x) approximate the functions $F_{o,i}$ and $G_{o,i}$ with sufficient accuracy.

3.5 FITTING BAND MODEL TO GASEOUS ABSORPTION CAPABILITY ALONG INHOMOGENEOUS PATH

The analytical expressions (30) and (31) of the previous section imply a coupling with the strong- and weak-line forms of approximation. However, this procedure of anchoring the intermediate-line formula in these two domains requires a quantitative refinement by means of a numerical comparison of various band absorption models. Goody (1964) has discussed the changeover from linear ($u \ll 1$) to square-root ($u > 3$) law regime by utilizing the Matheson diagram. From his discussion, it appears that a scale-shift in the variables u and y permits one to obtain a best fit.

The numerical values of the shift factors were determined through a process of attuning our model to the measured IRIS spectra of the dust-free period after January 1972. We found that a best fit was achieved by multiplying the u-parameter by (.25) and the y-parameter by (4.0). Various other trials of fitting did not generate as close an approximation as that.

The vertical heteorogeneity of the atmosphere required an additional refinement which was to be applied beyond the modeled stratification of 51 atmospheric layers inherent in the existing computer program (Pallmann et alii, 1973). It was decided to make use of the Curtis-Godson approximation as discussed by Goody (1964). The usual aim of scaling

approximations in the case of non-homogeneous path is to reduce the problem to that of a homogeneous path with scaled amount $\tilde{a}$, scaled temperature $\tilde{T}$, and scaled pressure $\tilde{p}$. The scaling adjustments turned out to be minor since they were confined to the respective layer depths, usually 1 km or less (near the ground). Since we recognized the importance of lines of intermediate strength, we were left with an uncertainty in the scaled amount $\tilde{a}$ of the order of $(p/\tilde{p})^{\frac{1}{2}} \leqslant 1.02$.

In conclusion, it was found that for the dust-free condition on Mars our model was closely attunable to the measured IRIS spectra. The further step of attuning the model to the dust-laden situation will be discussed in chapter 6.0.

4.0 SIMULATION OF EFFECTIVE ABSORPTION BY MIE PARTICLES (DUST)

In Chapter 2.0 of this report the analytics of a time-saving computer simulation was specified for the radiative transfer in a Mie-absorbing-scattering atmosphere. However, a detailed time estimate indicated that the incorporation of the scalar Mie-algorithm into our Radiative-Convective-Conductive Transfer (R.C.C.T.) Model would need computing time for a Martian diurnal cycle of 10 hours on the CDC 6600 System 175. To achieve cyclic balance over 24 hours at least twice as many 10 hours of computing time are needed. By repeating this procedure for 3 different dates, the time requirement would rise to more than 60 hours. In the light of such a steep estimation, the project opted for a lower-cost simulation.

The objective of the simulation is to concentrate on the impact of optically dense dust layers on the radiation field, and resultantly on the temperature field, rather than to formulate a sophisticated, but costly, model. Such a model would quantitatively describe the manifold interactions of a heterogeneous CO_2-gas and silicate dust stratification with solar and Martian-planetary radiation. The underlying analytics, as presented in Chapter 2.0, served as a framework for the approach chosen.

Various investigators have come up with findings pertinent to the approach of elucidating the impact of dust on the aforementioned fields. Andres (1971) offered some insight into the mechanics of dust-lifting on Mars. He hypothesized that aeolian dust particles may have rounded shape because of perennial rubbing. Roundedness makes them amenable to Mie theory. Furthermore, Andres showed that the turbulent flow near the surface enhances dust lifting and suspension. Thus, thermal convection, as built into our model, may maintain a kind of randomness which justifies the choice of a Gaussian dust distribution function. The manner by which this Gaussian is related to the dust extinction coefficient, as a function of height, was discussed earlier (Pallmann, 1974).

Subsequent studies of dust saltation, erosion, and suspension by Sagan (1973) established findings consistent with those of Andres, but they failed to explain the great elevation of several scale heights, at which dust was found during the gigantic storm event of 1971. Ajello et alii (1976) reported that limb observations by the Mariner 9 UV spectrometer television camera experiments showed that the dusty atmosphere was optically thick up to an altitude of 50 km with a sharp cut-off and an extinction optical depth of 3. At times, the opaque dust layer was topped by an optically thin haze layer at 70 km. Pang and Hord (1973) estimated a mean

radius of about 2μm for the dust up to 50 km. Most recently, Pang et alii (1976) gave as mean radius a value of 1μm.

Goody and Gierasch (1973) created a model to simulate the incipient stage of a Martian dust storm. They proposed the local generation of free-atmospheric heat via radiative heating in an initial dust cylinder of critical size and subsequent synoptic-scale convective circulation of a vortex (dust hurricane). A dust devil of gigantic extent would begin to suppress turbulence favoring an organized vorticity field (Goody and Gierasch, 1974). The regional lifting of dust by such a circulatory system is likely to be an efficient means of generating high dust concentrations near the top of the atmospheric convection layer (tropopause) which may be more than one scale height in elevation.

As shown by the hourly photography of the International Planetary Patrol (Martin, 1974) the dust storm started locally in the NE periphery of Noachis with another center in the NW quadrant of Hellas. A third dust "mushroom" appeared at about the same latitude over Ausonia but stayed only intermittently. The photographic evidence supports Goody and Gierasch's model. If one assumes the existence of powerful jet streams in the vicinity of the tropopause, the dust would spread enshrouding the globe as fast as it did (15 days).

The combination of gravitational settling and vertical mixing (Conrath, 1974; 1975) contributes toward explaining the

observed time evolution of the silicate particulates in the atmosphere. It is, however, not necessary to assume intense vertical mixing in all atmospheric layers throughout the dust stratum and for all longitudes and latitudes. As discussed in Chapter 7, near-adiabatic lapse rates which appear as a consequence of vigorous convective mixing, may be preferentially present in the lowest scale height and, again, near the top of the dust. In the center of the dust stratum, say, between 15 and 30 km, the atmosphere might be rather stable.

4.1 SOME ANALYTICS AS BASIS FOR A LOWER-COST SIMULATION OF THE DUST IMPACT

In equation (2) of Section 2.2 of this report, the normalized phase function

$$p(\cos\Theta) = \sum_{\ell=0}^{L} \varpi_\ell P_\ell(\cos\Theta) \tag{2}$$

is presented as a series expansion in Legendre polynomials $P_\ell(\cos\Theta)$ with (Θ) being the scattering angle. The series coefficients ϖ_ℓ may be represented by

$$\varpi_\ell = \frac{\lambda^2}{\pi \beta_{sc}} \int_{r_{min}}^{r_{max}} \frac{1}{2} \cdot \left[\lfloor^{(1)}_{\ell+1}(x,m) + \lfloor^{(2)}_{\ell+1}(x,m) \right] n(r)\,dr \tag{37}$$

(Canosa, J. and H. R. Penafiel, 1973). In this form, the following designations are used:

r : radius of aerosol particle,

$n(r)$: number of particles per cm^3 per unit radius interval at the radius r,

X: $\frac{2\pi r}{\lambda}$, Mie-factor,

β_{sc}: volume scattering coefficient.

The Legendre coefficients $L_{\ell+1}^{(i)}$ have been treated in detail by Dave (1970). The expression (37) requires explicit knowledge of the size distribution function $n(r)$ and the scattering coefficient β_{sc}. As discussed in Section 4.3, we showed that Deirmendjian's (1969) Silicate Haze M model is best suited to represent a dust load consistent with the quantitative information on vertically integrated column number density N, and mass density m as offered by Conrath et alii (1973; Sect. E, Table XX-4). The particulate size distribution function is thereby modelled as

$$n(r) = 5.3333 \times 10^{4} \cdot r \cdot \exp\left\{-8.9443 \cdot r^{1/2}\right\} \tag{38}$$

with the total number per cm^3 of particulates being N = 100.

Due to Deirmendjian, the volume scattering coefficient may be written as

$$\beta_{sc}(\lambda, n(r)) = \pi \int_{0}^{\infty} r^2 \cdot n(r) K_{sc}(r)\, dr \tag{39}$$

where K_{sc} designates the scattering efficiency factor (called Q_{sc} by van de Hulst, 1957). Incidentally, the integral on the right-hand side creates the bias (r^2) in favor of the larger sizes in the spectrum. For Mie-factors $x \geq 5$, $K_{sc}(r)$ under the integral may be replaced by $K_{sc} \simeq 2$. Thus, one obtains

$$\beta_{sc}(\lambda, n(r)) = 2\pi \int_{0}^{\infty} r^2 n(r)\, dr \tag{40}$$

with

$$\int_{0}^{\infty} n(r)\, dr = N \quad . \tag{41}$$

Since (r^2) is a non-decreasing function of r, we may write

$$(42) \qquad \int_0^\infty r^2\, n(r)\, dr = \overline{(r^2)} \int_0^\infty n(r)\, dr = \overline{(r^2)} \cdot N$$

Finally, this procedure renders

$$(43) \qquad \beta_{sc}(\lambda, N) = 2\pi \overline{(r^2)} N$$

This relationship will be utilized later on.

In order to improve on our first-order dust transmission function which we formerly attached by multiplication to the gaseous transmission function, we developed an analytical expression taking up the additional absorption of radiative energy via multiple scattering by dust. The underlying concept is that multiple scattering by dust enhances the radiative path length through the atmosphere increasing thereby the amount of radiative energy refracted into the particulates and, subsequently, absorbed. The imaginary portion of the complex index of refraction regulates the portion being absorbed.

We start with the scalar equation of radiative transfer within the spectral increment $(\nu, \nu+d\nu)$

$$(44) \qquad \mu \frac{dI_\nu(\tau_\nu; \mu, \phi)}{d\tau_\nu} = I_\nu(\tau_\nu; \mu, \phi) - \omega_\nu(\tau_\nu) \cdot J_\nu(\tau_\nu; \mu, \phi)$$

The notation is standard; for convenience, see Section 2.2 of this report. The source function

$$(45) \qquad J_\nu(\tau_\nu; \mu, \phi) = \frac{1}{4} e^{-\tau_\nu/\mu_0} P(\tau_\nu; \mu, \phi; -\mu_0, \phi_0) \cdot F + \frac{1}{4\pi} \int_{-1}^{+1} \int_0^{2\pi} P(\tau_\nu; \mu, \phi; \mu', \phi') \cdot I_\nu(\tau_\nu; \mu', \phi)\, d\mu'\, d\phi'$$

is composed of two terms. The first term on the right-hand

side represents the portion of the solar beam, in the direction $(-\mu_o, \phi_o)$, attenuated over the slant optical range (τ_ν / μ_o) and subsequently scattered into the direction (μ, ϕ). The second term represents scattered "self-illumination", that is to say, the fraction of radiative quanta impinching as diffuse radiation <u>from</u> all directions (μ', ϕ') which becomes scattered <u>into</u> the direction (μ, ϕ). The function $\omega_\nu(\tau_\nu)$ is equal to $\left(\beta_{\nu,sc}(\tau_\nu) / \beta_{\nu,ex}(\tau_\nu)\right)$.

With the prevalent size of the Martian dust particle being between 1 μm (Pang et alii, 1976) and 2 μm (Pang and Hord, 1973), a rather pronounced forward scatter is present. Each layer passes on to the next lower layer through this maximum of scatter most of the scattered energy. Given a manifold layer structure of dust load and multiple scattering therein, the diffused radiation field gradually approaches axial symmetry such that the diffuse intensity near the local zenith is just a few times larger than that near the horizon (see Sobolev, 1963; his chapt. 3). If we approximate this characteristic by the condition of isotropy, based on the principle of energy conservation, we are able to specify the analytical form for the dust transmission function.

The radiative transfer equation for $I^{(o)}$ is multiplied by $d\omega$ and integrated over all solid angles. We obtain for an isotropic source function (Goody, 1964; p. 52: Eddington's

approximation)

$$\frac{1}{\beta_{ex}} \cdot \frac{dF_\nu}{dx} = -2\pi \left(I_\nu^{\uparrow} - I_\nu^{\downarrow} \right) + 4\pi J_\nu , \tag{46}$$

x: geometric depth.

For computational purposes, we adopt here a two-stream model. A split of the flux function into $F^{\uparrow}$ and $F^{\downarrow}$ appears applicable for a scattering and absorbing source function because of the initially pronounced forward scatter of Mie theory. We find

$$dF_\nu^{\downarrow} = -2\pi I_\nu^{\downarrow} \beta_{ex} dx + 4\pi \beta_{ex} dx \left\{ \frac{\beta_{sc}}{\beta_{ex}} \cdot p(\theta_0, \phi_0) \cdot \frac{F_0}{4\pi} e^{-\tau_\nu/\mu_0} + \frac{\beta_{sc}}{\beta_{ex}} \int_{\text{foreward}} \tilde{p}(\cos\Theta) \cdot I_\nu^{\downarrow} \frac{d\omega'}{4\pi} \right\} \tag{47}$$

(see also Deirmendjian, 1969; p. 94).

For isotropic conditions, $F_\nu^{\downarrow} = \pi I_\nu^{\downarrow}$, and p = const.

Thus, one obtains

$$\frac{dF_\nu^{\downarrow}}{F_\nu^{\downarrow}} = -2\beta_{ex} dx + \left[\beta_{sc} \tilde{p}(\theta_0, \phi_0) \frac{F_0}{F_\nu^{\downarrow}} e^{-\tau_\nu/\mu_0} + 2\beta_{sc} \right] dx \tag{48}$$

On the right-hand side, the first term represents the hemispherical downward flux extinction, the second and third terms the attenuation due to primary and multiple scattering, respectively.

Integrating over a finite depth range Δx and inverting the natural logarithm yields

$$\frac{F_\nu^{\downarrow}}{F_{\nu,0}^{\downarrow}} = \mathcal{T}_F^{\downarrow} = \exp\left\{ -2\beta_{ex} \Delta x \right\} \cdot \exp\left\{ [\cdots] \Delta x \right\} \tag{49}$$

The second exponential factor on the right-hand side stands for the component transmission function due to primary and higher order scattering. Since the first exponential factor previously represented the only dust absorption function used in our model (Pallmann, 1974), the second factor has been taken up to account for the additional absorption of radiative energy due to multiple scattering. The replacement of the scattering coefficient β_{sc} by an effective dust absorption coefficient will be dealt with in sections 4.2 and 4.3 of this report.

4.2 BUDGETING IN BULK OF ENERGY ABSORPTION IN GROUND-ATMOSPHERE SYSTEM

With a model silicate haze M (Section 4.1) and an albedo of single scattering ϖ_o = .8 for visible solar radiation (Deirmendjian, 1969; Table T.99), we find a 20% absorption in the dust extinction process. In the top 10 km of the model atmosphere, from 50 to 40 km of height, there is no dust. The dust spreads out from 40 km down to the surface in accordance with a Gaussian distribution centered at ground level. Because of the proportionality between the number density N of dust and the effective dust absorption coefficient, a plot of the latter function versus height may represent the shape of the distribution curve.

A tabular account may elucidate the budgeting procedure:

50-40 km	No dust	
40-0 km	Dust layer	
40-35 km	Reflectivity of downward solar radiation: (.05) per 1 km total fraction reflected: (.23)	Transmissivity of downward solar radiation: (.95) per 1 km transmitted: $(.95)^5 = .77$
35-0 km	Per 1-km layer: (.9934) transmitted or finally at ground, $(.9934)^{35}$ = (.793) of impinchment (.77) transmitted: .6107	(.0066) absorbed in 35 km layer: (.77) - (.6107) - .1593 absorbed

For solar radiation impinching at the ground:

Surface Albedo: (.3)

0 km	(.6107) x (.3) = .1832 reflected;	(.6107) x (.7) = .4275 absorbed by ground;
0-35 km	$(.9934)^{35}$ = (.793) of ground-reflected portion (.1832) transmitted: (.1453)	absorbed by atmosphere: (.1832) - (.1453) = (.0379)
40 km	Transmitted outward: (.1453)	

Total fraction of solar radiation absorbed in the down- and up-sweep:

.1593

+ .0379

.1972

or close to 20%. This is a satisfactory match to the value of $(1 - \tilde{\omega}_o)$ of the model silicate haze M whose complex index of refraction is m = 1.55 - i·0.0155. The planetary albedo amounts to (.3753) which is rather high.

A second budget with a planetary albedo value of (.29) yields the following fractions of reflection, transmission and absorption:

50-40 km	No dust	
40-0 km	Dust layer	
40-35 km	Reflectivity of downward solar radiation: (.05) per 1 km	Transmissivity of downward solar radiation: (.95) per 1 km
	total fraction reflected: (.23)	transmitted: (.77)
35-0 km	Per 1-km layer (.98094) transmitted	(.01906) absorbed
	or finally at ground: $(.98094)^{35}$ = (.5099)	in 35 km layer (.77) - (.3926) = (.3774)
	of impinchment (.77) transmitted: (.3926)	absorbed

For solar radiation impinching at the ground:

		Surface Albedo: (.3)
0 km	(.3926) x (.3) = (.1178) reflected;	(.3926) x (.7) = (.2748) absorbed by ground;
0-35 km	$(.98094)^{35}$ = (.5099) of ground-reflected portion (.1178) is transmitted: (.0601)	absorbed by atmosphere: (.1178) - (.0601) = (.0577)
40 km	Transmitted outward: (.0601)	

This time, the total fraction of solar radiation obsorbed in the down- and up-sweep through the atmosphere is

$$\begin{array}{r} (.3774) \\ \underline{+\ (.0577)} \\ (.4351) \end{array}$$

or close to about 44%.

In summarizing the two bulk budgets of energy absorption in the ground-atmosphere, we have in percent of solar radiation impinching at the top of the atmosphere:

Case with Transmissivity between 35 and 0 km being	Diffuse Reflectivity	Absorptivity	
1-	37.5%		Outer Space
2-	29. %		
1-(.99340)/km	23.% + 14.5%	19.8%	Atmosphere
1-(.98094)/km	23.% + 6.%	43.7%	
1-	30.%	42.7%	Ground
2-	30.%	27.3%	

Balance:

1- (37.5 + 19.8 + 42.7)% = 100%

2- (29.0 + 43.7 + 27.3)% = 100%

4.3 EFFECTIVE ABSORPTION BY MARTIAN DUST PARTICLES

Although the value for atmospheric absorption given in the previous section seems rather high, it is consistent with the extinction optical depth of 3, offered by Ajello et alii (1976). Furthermore, the vertically integrated column number density of 1.21×10^{7} for $r = 1\,\mu m$, as given by Conrath et alii (1973), yields, when inserted in equation (43)

$$\beta_{sc}(\lambda, N) = 2\pi \overline{(r^2)} N$$

a value for the volume scattering coefficient β_{sc} of about 1.2×10^{-6} cm^{-1}. In this context, one has to remember that $\overline{(r^2)}$ must satisfy the relationship $\overline{(r^2)} = \frac{1}{N} \cdot \int r^2 n(r) dr$.

This expresses the characteristic of a polydisperse dust particle size spectrum (Deirmendjian, 1969).

The previously adopted principle that, via multiple scattering within an optically-thick dust layer, the likelihood increases for photons to become absorbed, mostly by the particulates, has led to a numerical estimation of the percentage involved in this additional absorption. Formerly, we had just accounted for an average slant solar beam absorption in the mode of single scattering (Pallmann et alii, 1973; Pallmann, 1974; Dannevik and Pallmann, 1974). Based on calculations of the brightness of the sky in the case of multiple scattering (Atroshenko et alii, 1963), it was determined that multiple scattering takes up about 25% of the total scattering leaving 75% of the diffuse sky radiation at the surface for primary scattering. With an albedo of single scattering value of (.63), the ratio of the coefficient of multiple scattering to the extinction coefficient is close to (.21).

Deirmendjian (1969) obtained for model silicate haze M and various values of the imaginary part of the complex index of refraction the rather even numerical figure of about $1. \times 10^{-6}$ cm^{-1} for the volume extinction coefficient. With this particular value and adopting an approximate 50% efficiency for multiple scattering to generate further absorption, one arrives at $(.5) \times (.21) \simeq (.10)$. Together with the relative dust absorption coefficient, previously incorporated into the model, we have

$$(50)\quad \frac{\beta_{ab}(\text{direct})}{\beta_{ex}} + \frac{\beta_{ab}(\text{mult. sc.})}{\beta_{ex}} = (.26)$$

or with $\beta_{ex} = 1. \times 10^{-6}\ \text{cm}^{-1}$

$$(51)\quad \beta_{ab}^{\text{Dust}} = 2.6 \times 10^{-7}\ \text{cm}^{-1}$$

This value of the effective absorption coefficient due to dust should be considered as representative of atmospheric conditions close to the maximum dust-load in space and time. However, it has been derived from a vertical impinchment of solar radiation rather than time-dependent slant incidence. The diurnal cycle of the apparent march of the sun in the local sky covers a zenith angle range from $(\pi/2)$ to noon zenithal distance, equal to the difference between latitude and solar declination. If one takes in the average a zenith angle of (0.3π) the corresponding value of sec (0.3π) for the slant range is close to (1.6). Therefore, a somewhat enhanced value for the maximum of the effective absorption coefficient may be allowed. Also, the gradual dissipation of the dust phase through November and December 1971 calls for a persistent decline of the absorption of radiative energy by dust.

The circumstances just described suggested a series of simulations for the effective dust absorption coefficient EP in order to determine the numerical values of A and B in the expression

$$EP(Z) = A \exp\{-B \cdot Z^2\} \tag{52}$$

In an earlier report (Pallmann, 1974) the compatibility of this analytical form with other forms (see Conrath, 1974) was discussed. A series of computer runs with our R.C.C.T. and F/O models was undertaken. The numerical values for the amplitude parameter A ranged from (0.5×10^{-7}) cm^{-1} to (3.0×10^{-7}) cm^{-1}. The parameter B was held at (1.11×10^{-9}) cm^{-2}. In chapter 7 of this report, several CALCOMP plots of the simulation are presented.

5.0 IRIS, IRR AND S-BAND OCCULTATION DATA

In order to perform a multiple attunement of our time-dependent radiative-convective-conductive heat transfer (R.C.C.T.) model to various types of Mariner 9 measurements, IRIS, IRR-, and S-band occultation-data were requested from the National Space Science Data Center (N.S.S.D.C.) at Goddard-Space Flight Center in Greenbelt, Maryland 20771.

The Data Center made two sets of magnetic tape available which held the measured information of IRIS and IRR for several hundred spacecraft revolutions. In addition, the N.S.S.D.C. sent a set of microfilms of tabulated and plotted S-band occultation data for both the standard and extended missions.

Because of the extensive volume of data on the tapes, a rather time-consuming computer sorting became necessary. Some problems with the retrievability of IRIS data blocks had to be overcome before the excerpts of the desired data were put on about 20,000 cards. We found that the actual IRIS measurements had been arranged in an excellent fashion. The N.S.S.D.C. Information Packet had been carefully prepared serving efficiently its purpose of explaining the code of the IRIS Reduced Data Record, Type 7— Calibrated Martian Spectrum.

Similarly, the IRR tape data had been very well arranged. The aforementioned problem did not exist here

since the data blocks were labeled such that excerpting was straight forward. The microfilms with the S-band occultation data were handled with standard reader-printer equipment available in the Department of Earth and Atmospheric Sciences at Saint Louis University.

A brief word on cost concerning the tape data sorting and excerpting procedure. Because of the unlabeled formats used for the IRIS sequences, about $250— at University rate— had to be expanded on an IBM 360/65. The cost of the IR-radiometric data handling was about $170—whereas microfilm printing cost was minor.

Furthermore, the attention of the reader is directed toward a peculiarity in the data, which is related to the absence of coincident observations among S-band occultation, IRIS, and IRR measurements. Orbital conditions of the spacecraft caused, for a given region and local time, the IRIS observations to lag behind the occultation measurements by 15 to 45 days (Leovy, 1973). However, S-band occultation data can be used in conjunction with IRIS or IRR measurements if larger-scale Martian characteristics within limited latitude belts are of prime interest.

An additional complementarity may be found in that occultation measurements, although noisier, generally possess a better vertical resolution than the IRIS information which offers reliable results over deeper layers. In fact, Conrath (1974b) determined the vertical resolution of the technique

for the IRIS-inverted Martian temperature profiles. He offered a value of about 6.5 km in the lowest 10 km increasing gradually to slightly more than 20 km above the height of 33 km.

The data card bank, generated from the magnetic tape and film material, served as the base for an extended simulation procedure. It was finally decided to concentrate on the following dates for the purpose of representing the gradual transition in the S.H. mid-latitude from the dust-laden to the dust-free condition:

— November 22, 1971 (revolution 17).

— December 03, 1971 (revolution 39),

— December 24, 1971 (revolution 79),

— January 08, 1972 (revolution 111),

— February 16, 1972 (revolution 189).

For the last 2 dates, no S-band occultation data were available. They reappear after May 6, 1972 when the tracking station at Goldstone, California received occultation signals during the even-numbered revolutions from 352 to 450.

6.0 REFINED MODEL AND ITS ATTUNEMENT TO DUST-LADEN AND DUST-FREE CONDITIONS

In the present chapter, the governing mathematical equations of the model are presented in section 6.1 as they have been refined on the basis of our former radiative-conductive model. A specific amplification of this model is given by the incorporation of convective heat transfer anywhere in the atmospheric stratification, not just near the ground. The principal refinement, however, should be seen in improving the CO_2 and dust transmission functions. The former makes allowance now for intermediate-line strengths as well as strong- and weak-line absorption whereas the latter includes indirect absorption by optically thick dust via multiple scattering, adding to direct dust extinction. Some procedural guidelines of the overall attunement of the model follow in section 6.2. This discussion deals also with the tuning problem for dust-laden conditions.

6.1 GOVERNING ANALYTICS OF THE MODEL

The solution of the radiative transfer equation for the planetary problem leads, when integrated over the full range of (4π) steradian, to an expression of the spectral radiative net flux (Pallmann et alii, 1973). If additionally integrated over all wave numbers, the total

net flux results which may be inserted in the atmospheric heating rate equation to render

$$\rho_m c \frac{\partial T_m}{\partial t} = \frac{\partial}{\partial x}\left\{ k \frac{\partial T_m}{\partial x} - 2\pi \sum_i \left[S_i(0) \cdot \mathcal{T}_i(x_m, \bar{\mu}^{-1}) \cdot \mathcal{T}^D(x_m, \bar{\mu}^{-1}) \right.\right.$$

$$- \bar{\mu}^{-1} G_i(x_s) \cdot \mathcal{T}_i[b(x_m - x_M)] \cdot \mathcal{T}^D[b(x_m - x_M)]$$

(52)

$$+ \sum_{m'=1}^{m} \mathcal{B}_{i,m'} \cdot b^{-1} \frac{\partial}{\partial \xi_{m'}} \left(\mathcal{T}_i[b(x_m - \xi_{m'})] \cdot \mathcal{T}^D[b(x_m - \xi_{m'})] \right) \Delta\xi_{m'}$$

$$\left. \left. + \sum_{m'=m}^{M} \mathcal{B}_{i,m'} \cdot b^{-1} \frac{\partial}{\partial \xi_{m'}} \left(\mathcal{T}_i[b(\xi_{m'} - x_m)] \cdot \mathcal{T}^D[b(\xi_{m'} - x_m)] \right) \Delta\xi_{m'} \right] \Delta\nu_i \right\}$$

for $0 \leq x_m, \xi_{m'} \leq x_M$; $t > 0$.

In this equation, the subscript "m" designates the index for a given level between the top of the atmosphere (at 50 km) and the surface, and the subscript "i" indicates a particular radiative wave-number increment. Furthermore, $S_i(0)$ is the solar spectral irradiance at the top of the atmosphere, $G_i(x_s)$ is the upwardly directed spectral flux, emitted by the ground, at depth x_s, $\mathcal{B}_{i,m'}$ is the Planck's function, $\mathcal{T}_i$ is the flux transmission function for CO_2, $\mathcal{T}^D$ is the dust transmission function (grey absorption), and k

is the thermal conductivity. The derivatives in this equation are replaced by finite differences. A simple forward difference is used for the time derivative, while modified centered differences are employed in the space derivatives. The resulting equation is quite lengthly and will not be reproduced here.

The sub-surface heating-rate equation in its finite difference form is given by

$$\rho_m c \frac{T_{s_m}^{n+1} - T_{s_m}^{n}}{\Delta t} = \frac{k}{\Delta x^2}\left(T_{s_{m+1}}^{n} - T_{s_m}^{n-1} - T_{s_m}^{n+1} + T_{s_{m-1}}^{n}\right) \tag{53}$$

$$\text{for } m = M+1, M+2, \ldots M_d .$$

where the superscript "n" refers to the time step, and M_d is the lowest soil level under consideration.

The ground-atmosphere interface condition at $x = x_s$ which expresses the continuity of the total heat flux across the interface, is stated as

$$k_s \frac{T_{s_{M+1}}^{n+1} - T_{s_M}^{n+1}}{\Delta x_s} - k \frac{T_{M-1}^{n+1} - T_M^{n+1}}{\Delta x_m} -$$

$$4\varepsilon\sigma\left(T_{s_M}^{n}\right)^3 \cdot \left(T_{s_M}^{n+1} - \frac{3}{4} T_{s_M}^{n}\right) +$$

$$2\pi \sum_i \sum_{m'=1}^{M} \mathcal{B}_{i,m}^{n} \frac{\Delta \mathcal{T}_i}{\Delta x_{m'}} \left[\ell(x_M - x_{m'})\right] \cdot \mathcal{T}\left[\ell^D(x_M - x_{m'})\right] \Delta x_{m'} + \tag{54}$$

$$2\pi \sum_i (1 - \alpha_s) S_i^n \cdot \mathcal{T}_i(x_M \bar{\mu}^{-1}) \cdot \mathcal{T}^D(x_M \bar{\mu}^{-1}) = 0$$

or $$T_s(x_s+0,t) = T(x_s-0,t) \quad ; t \geq 0.$$

In equation (54), k_s designates the soil thermal conductivity, ε the bulk surface emissivity, σ the Stefan-Boltzmann constant, and T_s the soil temperature.

In equation (53), as well as equation (54) and the finite difference form of equation (52), the DuFort-Frankel two-level explicit differencing method has been employed (Carnahan, Luther and Wilkes, 1969). This procedure is computationally unconditionally stable.

The upper boundary condition for the ground-atmosphere system reads

(55) $$T(0,t) = T_0 \quad ; \quad \text{for } t \geq 0.$$

The lower boundary condition is

(56) $$T_s(x_d,t) = T_d \quad ; \quad \text{for } t \geq 0.$$

The initial conditions are given by

(57) $$T_s(x,0) = T_{s_\ell}(x) \quad ; \quad \text{for } x_s < x < x_d$$

$$T(x,0) = T_\ell(x) \quad ; \quad \text{for } 0 \leq x \leq x_s$$

as a discrete input.

The system of equations (52) - (57) suffices to establish a unique solution at 81 grid points in the vertical throughout the region $x_d \leq x \leq 0$, for any time $t > 0$ (30 grid point in the soil, and 10 in the lowest 6.5 km of the atmosphere).

The built-in convective heat transfer capability is based on Kraichnan's turbulent thermal convection theory (1962). Thereby, the convective heat flux at the top of the constant flux layer (CFL) is given as

$$F^{*} = 8.9 \times 10^{-2} \cdot (\rho_{CFL} \cdot c_p) \cdot 2^{4/3} \cdot \kappa \cdot (T_s - T_c)^{4/3} \cdot \left(\frac{g}{T_c \cdot \kappa \cdot \nu}\right)^{1/3} \tag{58}$$

with

$c_p = 8.2 \times 10^{6}$ ergo $g^{-1}\ k^{-1}$

$\kappa = 8.$ $cm^2\ sec^{-1}$

$\nu = 10.$ $cm^2\ sec^{-1}$

$g = 3.76 \times 10^{2}$ $cm\ sec^{-2}$

$\rho_{CFL} = 1.12 \times 10^{-5}$ $g\ cm^{-3}$

The mathematical forms of the CO_2 and dust transmission functions have been presented in chapters 3 and 4 respectively. Attention is called to the fact that each of the transmission functions ($\mathcal{T}_i$) in equations (52) and (54) is approximated by a product which may be written as

$$\mathcal{T}_i(x_1 - x_2) = \prod_{j=1}^{J} \mathcal{T}_i(x_j - x_{j-1}) \tag{59}$$

such that the product index "j" extends over all J intervening segments $(x_j - x_{j-1})$ between the end points of the depth interval (x_1, x_2). For convenience, these segments are taken so as to coincidence with the atmospheric layers labeled by the index "m".

Questions as to the size of space and time increments as well as remarks concerning the previous model have been treated elsewhere (Pallmann et alii, 1973).

6.2 HIGHLIGHTS OF ATTUNEMENT

The procedure of fitting our refined band model to the CO_2 absorption capabilities was covered in section 3.5 for an inhomogeneous radiative path. As indicated earlier, one of the goals of the simulation was to achieve a fitting as close as possible for the dust-free condition. The particular date chosen to represent this condition was February 16, 1972. IRIS and IRR measurements for the midlatitudes of the Southern Hemisphere had to be compared and adjusted on the basis of their respective resolution. Our R.C.C.T. model had to generate a sequence of simulation runs which produced temperature-soundings cyclically balanced over a period of 24 hours (diurnal cyclic balance). Between 288 and 432 time-steps of integration or 2 to 3 days were needed. A cyclically balanced temperature sounding which coincided with the time of the IRIS measurement, served as input for F/O-model runs whose output was a simulated IRIS spectrum over the wave-number range from 200 to 2,000 cm^{-1}. Depending on how close a match was obtained, the numerical values of various scaling parameters had to be adjusted. We refer here to the K parameter in equation (14), the modified u- and y-parameters and the Curtis-Godson scaling factors of

section 3.5. Additional runs of both the R.C.C.T. and F/O programs with adjusted values for these parameters were undertaken. This iterative mode of attunement finally led us to accomplish a close match to the measured IRIS spectrum produced under dust-free conditions over the midlatitudes of the Southern Hemisphere.

In turning next to the dust storm dissipation phase we selected the IRIS, IRR, and S-band occultation measurements of December 24, 1971 as input data for another series of runs with both programs. This time, a dust transmission function had to be inserted to model a moderate dust impact on the solar and planetary radiation fields. By carefully evaluating the outputs of time-dependent T-soundings, temperature lapse rates, and convective overturn from the R.C.C.T. model, and upward spectral flux, emitted by ground and atmosphere and transmitted to the top (50 km), from the F/O-program, we adjusted the value for the effective dust absorption coefficient, atmospheric layer absorptivities, and cumulative reflectivity at the top. For numerical detail, reference is made to chapter 4.

For a treatment of the optically-thick dustload in the Martian atmosphere, the day November 22, 1971 was chosen. Again, IRIS, IRR and S-band occultation data were scrutinized to be used as input for our simulation procedure. It became apparent that the amplitude value of the effective dust absorption coefficient had to be quite large. We adopted

values as high as (3.0×10^{-7}) cm^{-1} which corresponds to an absorption optical depth of (1.2) or an extinction optical depth of about (3.0). More detail may be found in chapter 4.

7.0 DISCUSSION OF RESULTS

With the attuned computer model, as discussed in chapter 6, a series of outputs was generated via the time-dependent MARSTEMP (M/T) and adjunct FLUXOUT (F/O) programs. The M/T program produced, for each time-step (between 4 and 10 min) over a total of 36 to 60 hours of simulated time, the following outputs as printouts:

- IR-flux emitted by the ground and transmitted to 52 explicit atmospheric reference levels;
- solar flux, downwardly directed, and transmitted to these 52 levels;
- solar flux, diffusely reflected by the ground, and transmitted upward to these 52 levels;
- IR-flux, emitted upward by 51 atmospheric source layers, and transmitted to 51 reference levels;
- IR-flux, emitted downward by 51 atmospheric source layers, and transmitted to 51 reference levels.
- upward total flux at 52 levels;
- downward total flux at 52 levels;
- net flux at 52 levels;
- new temperature at 52 levels;
- rate of temperature change at 52 levels;
- temperature lapse rate at 52 levels; and
- subsurface soil temperature at 30 depths.

The F/O program generated for a given time (generally identical to the indicated MARINER 9 measurement hour) the spectral flux value within 360 increments of 5 cm^{-1} between 200 and 2,000 cm^{-1} (IRIS range). These fluxes were available as

— IR-flux emitted upward by the ground, and transmitted to the top of the atmosphere;

— IR-flux emitted upward by an individual atmospheric source layer, subsequently attenuated by the intervening layers, and then integrated over all source layers; and

— sum of the previous two fluxes for all spectral increments.

From this broad variety of outputs, mostly the temperature soundings of the MARSTEM simulation and the F/O-outputs will be discussed. In addition, some plotted input functions will be presented as they relate to the findings .

7.1 ATTUNED MODEL OUTPUTS, DUST FREE CASE

The first basic step of attuning the model to Mariner 9 data was to fit the refined gaseous CO_2 band transmission function (chapter 3) to IRIS measurements taken under the condition of a dust-free Martian atmosphere. By means of an iteration of gradually improving computative F/O attunements, a rather close fit of the upwelling flux output to the measured IRIS spectrum was achieved. For February 16, 1972,

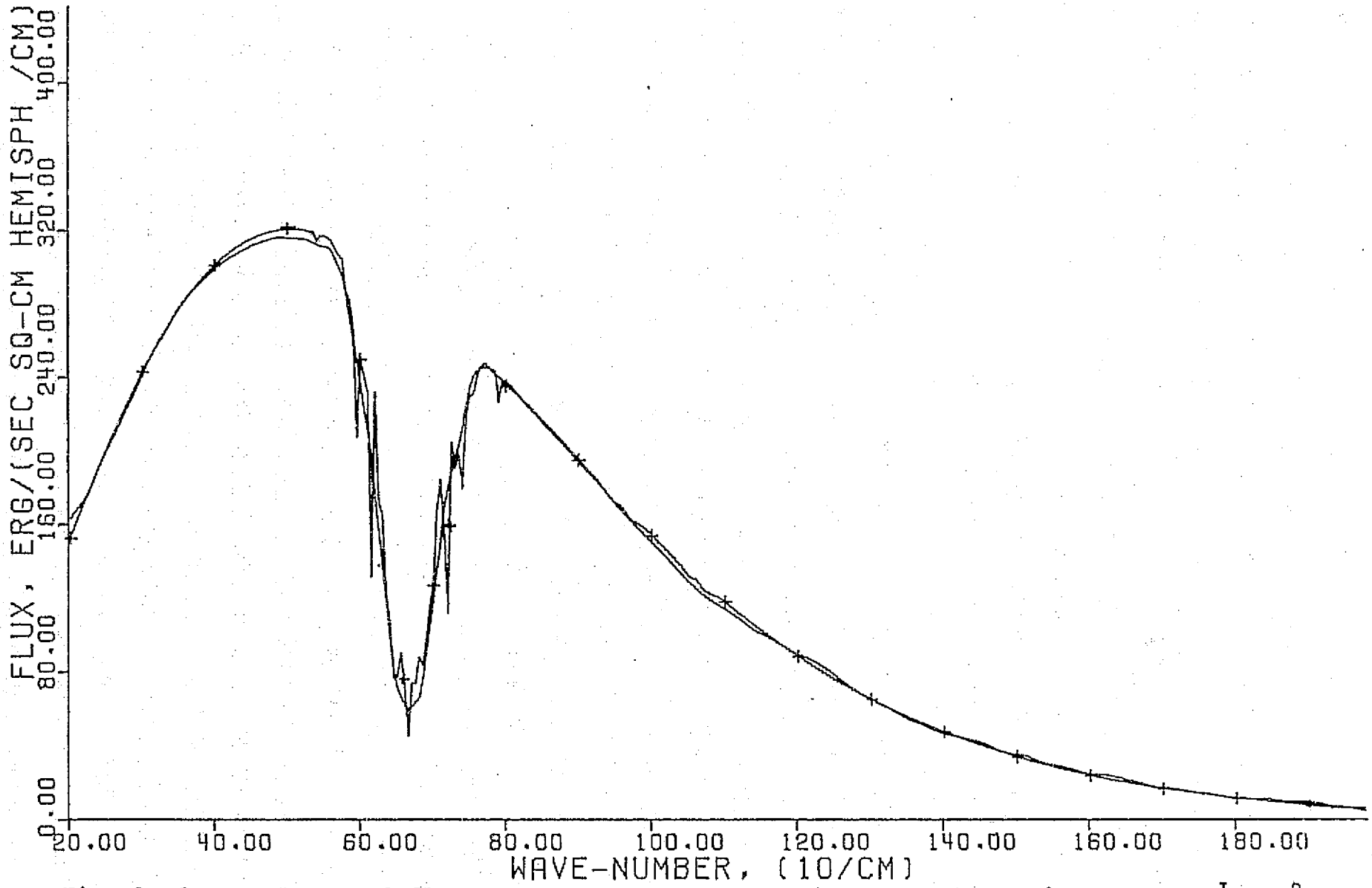

Fig. 1: Spectral upward flux, at the top of the Martian atmosphere, in erg. sec^{-1} cm^{-2} $(hemisph.)^{-1}/cm^{-1}$, versus wave number in cm^{-1} for February 16, 1972, 12.72 LMST, at -41.4 deg. lat. and 327.7 deg. long., as simulated by unabridged F/O program on the CDC 6600 System 175 (marked by "+" sign). Flux is the sum of ground and atmospheric layer emission, duly attenuated.—Solid curve: average of 3 measured IRIS spectra in degraded mode.

the quality of the attunement is illustrated in figure 1. The matching upward flux was computed by an unabridged F/0 program in which the series expansion for the modified Bessel function of zeroth and first order held 99 terms (see equations (16), (17), (18) and (19)). As mentioned earlier, the representation of CO_2 band absorption for intermediate line strength became necessary, since our simulation study demonstrated that neither a strong-line model alone, nor strong-line-weak-line models rendered sufficiently accurate numerical attunement. It is exactly the attunement procedure which provides a sufficiency criterion.

The temperature sounding used as an input for the F/0 run of figure 1 was a cyclically balanced T-sounding generated by the unabridged M/T program on the CDC 6600/System 175. (This computing system of United Computing Systems, Inc., St. Louis is about 13 times faster than the CDC 3300 at Yalem Computer Center, Saint Louis University, as far as our particular program is concerned. Because of limited computing funds, the simulation study with the system 175 was kept to 4.5 hours. Additional computing was performed through the easily accessible Yalem Center at Saint Louis University).

In order to throw more light on the question of how the number of terms in the aforementioned series expansion of the Bessel functions affected the output, some additional

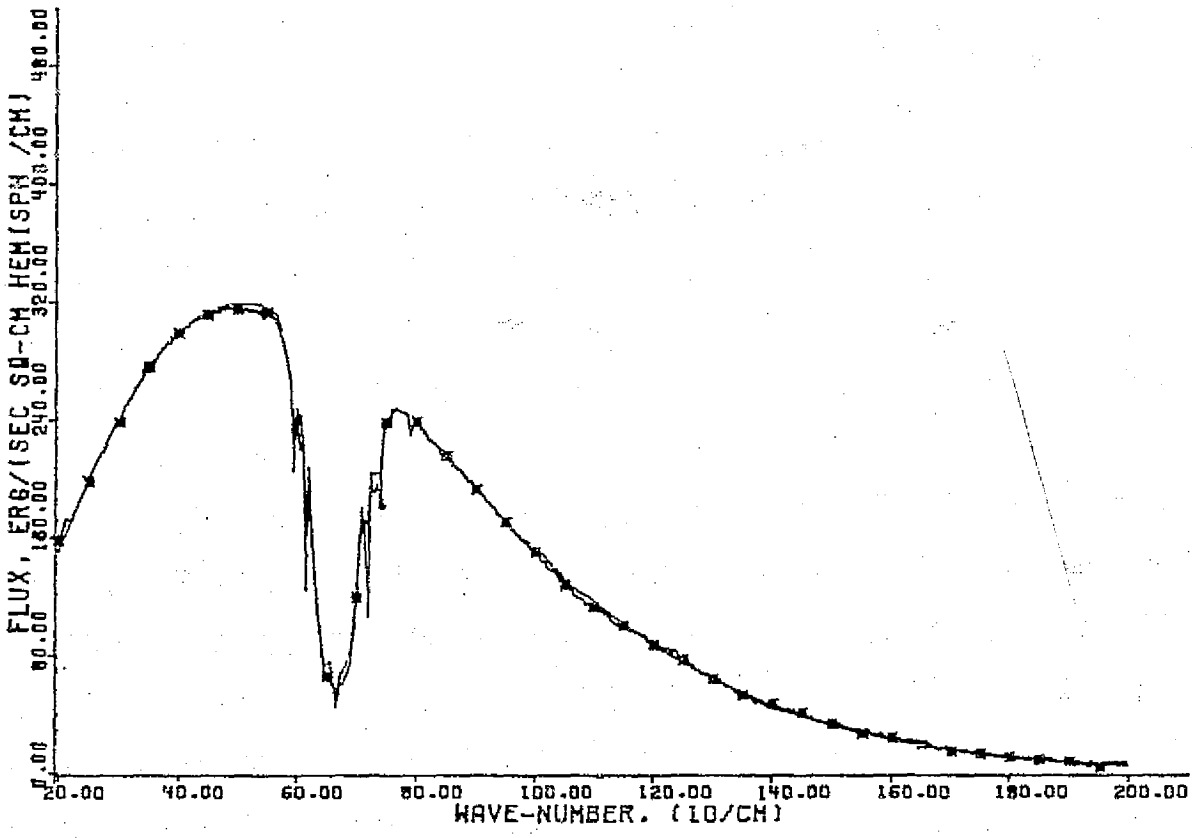

Fig. 2: Same as Fig. 1 except that this output was simulated by the abridged form (33 terms) of the F/O program on the CDC 3300/YALEM; the measured data are an individual IRIS spectrum in a non-degraded mode. This time, the curve of the measured spectrum is marked by an asterisk; the simulation is given a solid line.

runs with just 33 terms were carried out. With this particular modification, we combined some variations in the temperature input. Thus, instead of feeding into the F/O run a T-sounding which was generated by a run of 48 hours of the M/T model (cyclical balance), we used the original IRIS inverted temperature sounding in our F/O simulation. Figure 2 shows the result.

It is apparent that the matching is of good quality. Only minor differences exist due to the adoption of the abridged form for the series expansion of the modified Bessel function. The surface temperature and the T-sounding for the simulation was the same as that of the measured IRIS spectrum as shown in figure 3. Attention is called to the steep drop of temperature near the surface. Otherwise, there is nowhere a lapse rate close to the adiabatic value (5.2K/km).

As an additional variation, the IRIS-inverted T-sounding, with the mean IRR brightness temperature of 259.5K for the surface, was inserted in the abridged F/O program. The output is presented in figure 4 which clearly shows the influence of the surface temperature on the spectral flux welling up at the top of the atmosphere. The respective input sounding is shown in figure 5.

From the illustrations, previously shown, it is evident the surface temperature is a controlling factor in any

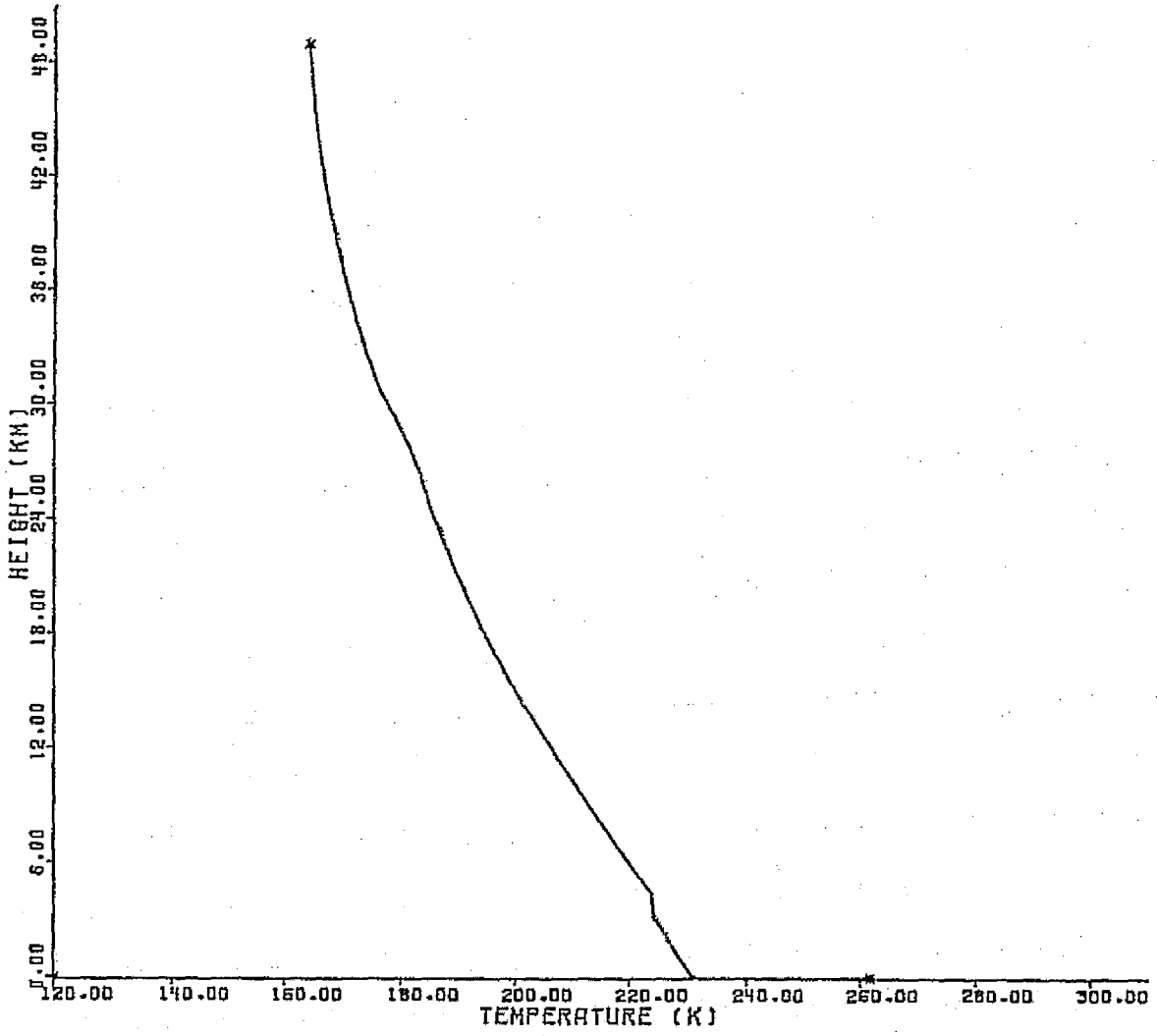

Fig. 3: The temperature sounding used as input for the simulation whose output appears in Fig. 2.

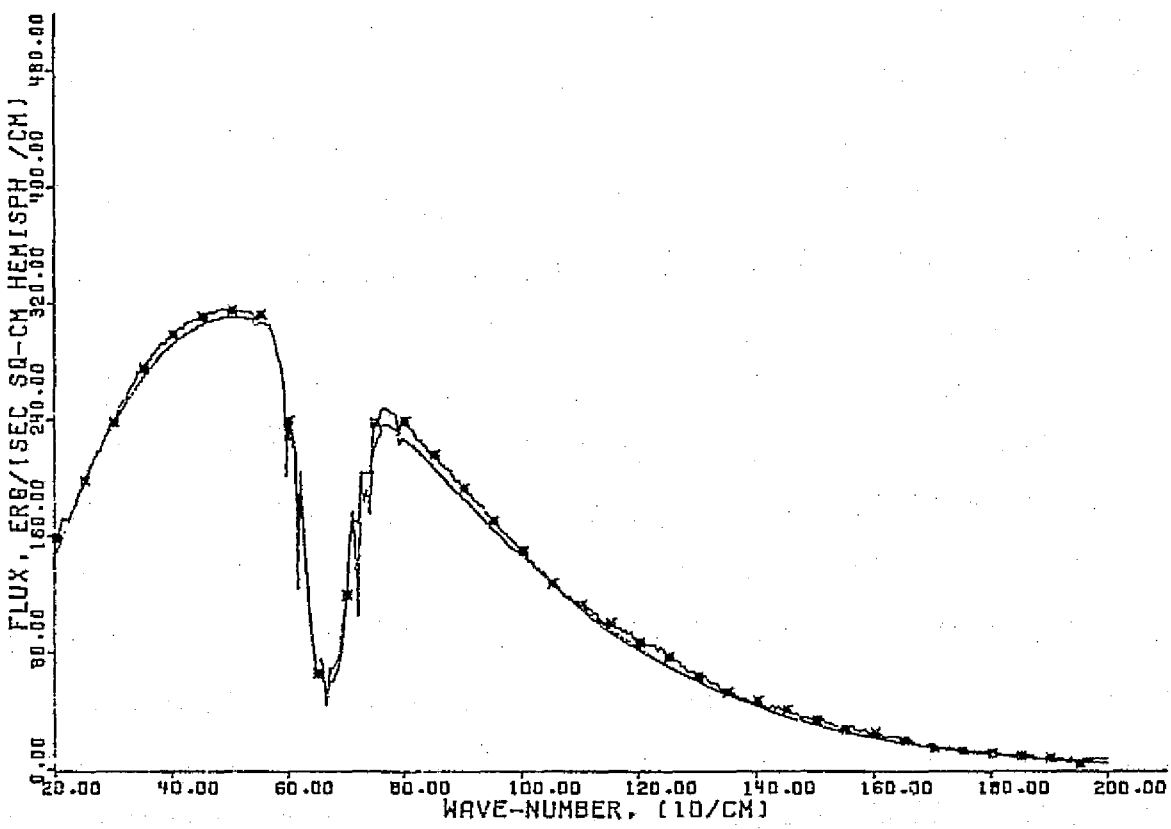

Fig. 4: Spectral upward flux, at the top of the Martian atmosphere, in erg sec^{-1} cm^{-2} (hemisph)$^{-1}$/cm^{-1}, versus wave-number in cm^{-1} for February 16, 1972, 12.72 LMST at -41.4 deg. lat. and 327.7 deg. long., as simulated (solid curve) by the abridged F/O program with T-sounding of Fig. 5 as input (T_s = 259.5K). Curve with (*) is the measured IRIS spectrum.

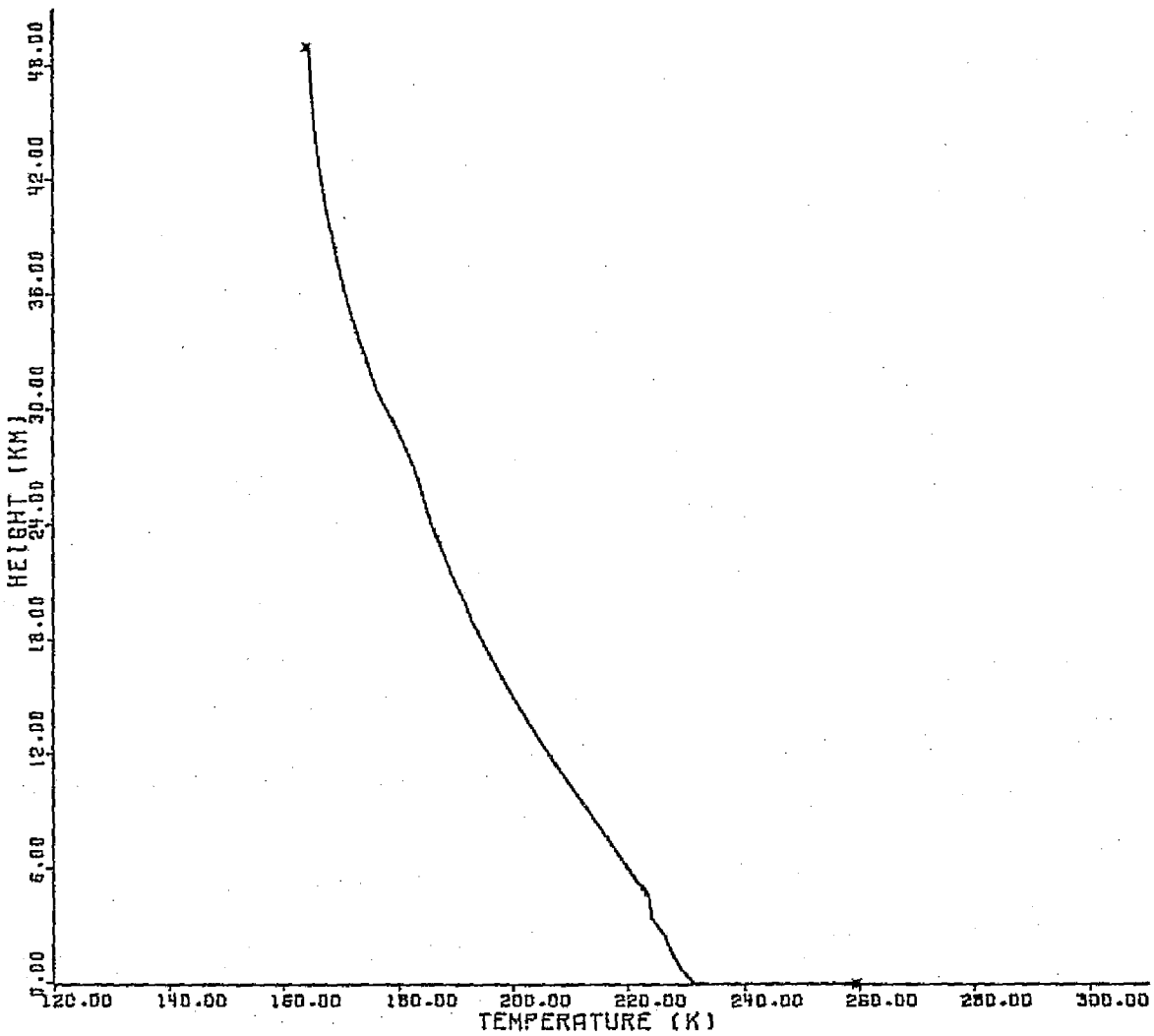

Fig. 5: Temperature sounding used as input for simulation whose output is given in Fig. 4. Curve is identical to T-sounding of Fig. 3 except for T_S = 259.5K.

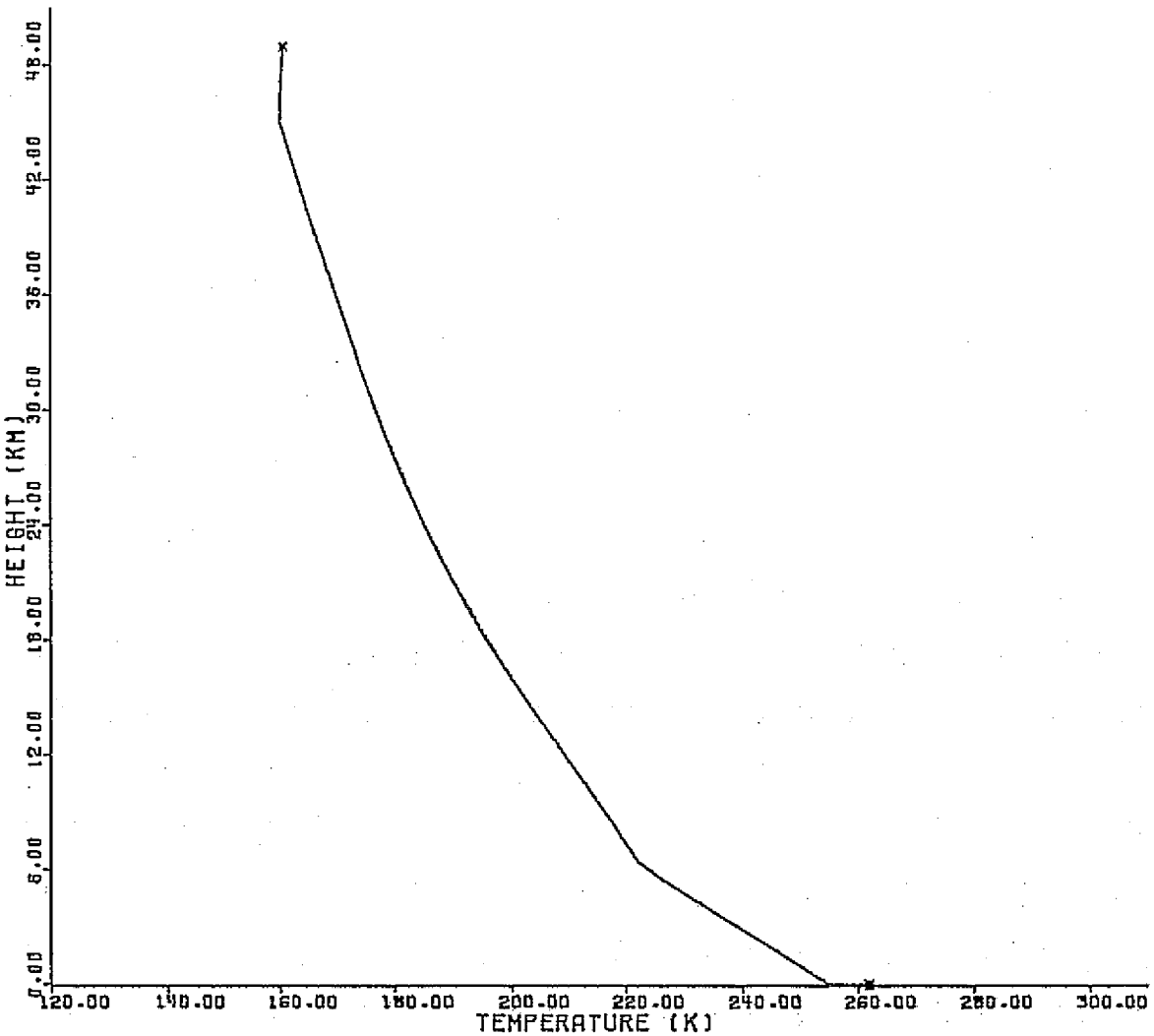

Fig. 6: M/T-model generated temperature sounding versus height used as input for a F/O-simulation under dust-free conditions on February 16, 1972; 12.72 LMST. Areographic location: -41.4 deg. lat. and 327.7 deg. long.; temperature lapse rate up to 6 km: adiabatic or steeper.

simulation procedure. It is for this reason that we have developed an analytical interface condition (see chapter 6) which is highly sensitive to all heat fluxes except advection considered contributory to the thermal setting at the surface. A justification for the omission of advective heat flux has been offered elsewhere (Pallmann et alii, 1973).

In the subsequent paragraphs of the section, some of the characteristic output of the attuned F/O- and M/T-models will be presented as they pertain to the dust-free case (February 16, 1972). In choosing a M/T-generated temperature sounding, given in figure 6, as input to a F/O-simulation instead of the IRIS-inverted T-sounding, we obtained again a high quality match with the measured IRIS data. The matching result is shown in figure 7. For both curves, the pertinent surface temperature is T_s = 261.8K.

A decomposition of the simulated spectral flux, welling up to the top of the atmosphere, has permitted us to illustrate the contributions of all atmospheric layers to that flux in the lower curve of figure 8. It is evident that the highest thermal level was achieved in the middle of both wings of the bulk CO_2 absorption band centered at 667 cm^{-1}. This atmospheric contribution to the spectral flux at the top was compared with the measured IRIS spectrum of February 16 in figure 9.

The simulated emission from the ground, subsequently attenuated by the atmosphere, has been related to the IRIS

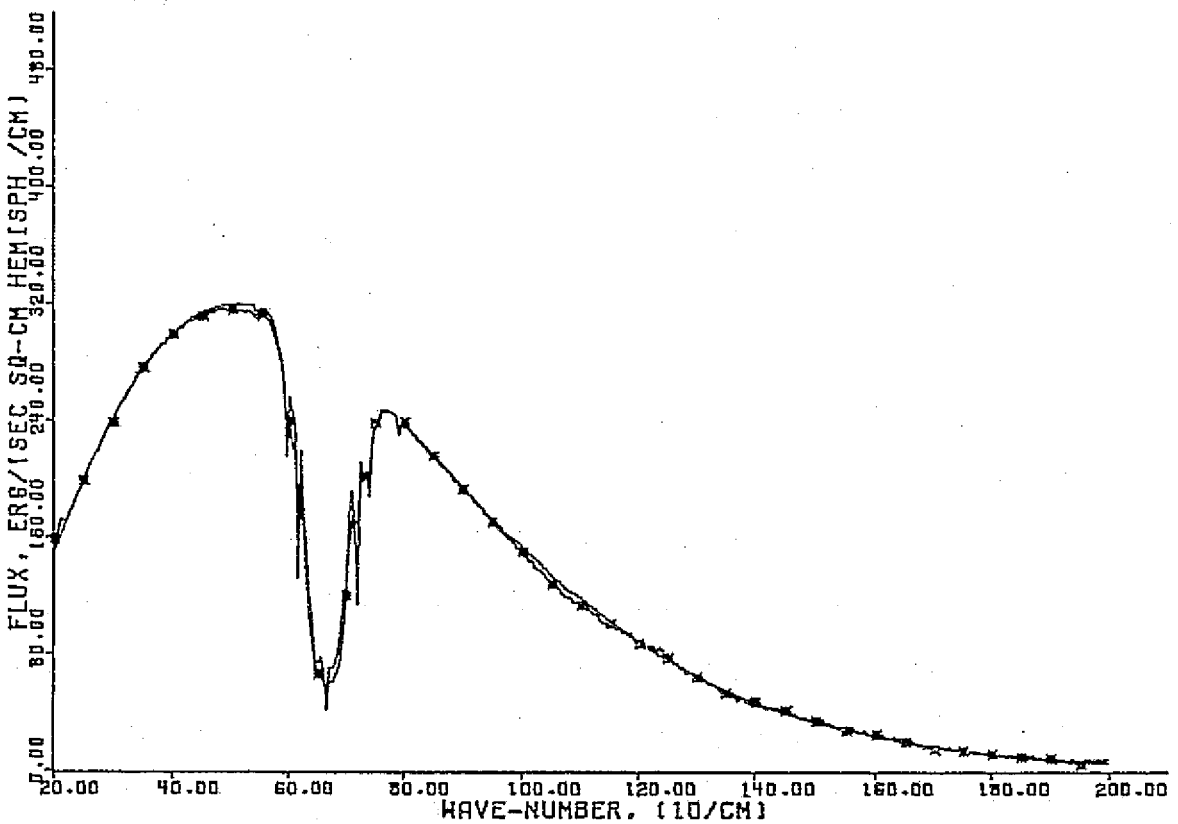

Fig. 7: Simulated flux and measured IRIS flux versus wave-number; the latter flux curve is marked by (*). F/O input: T-sounding, date and location of Fig. 6.

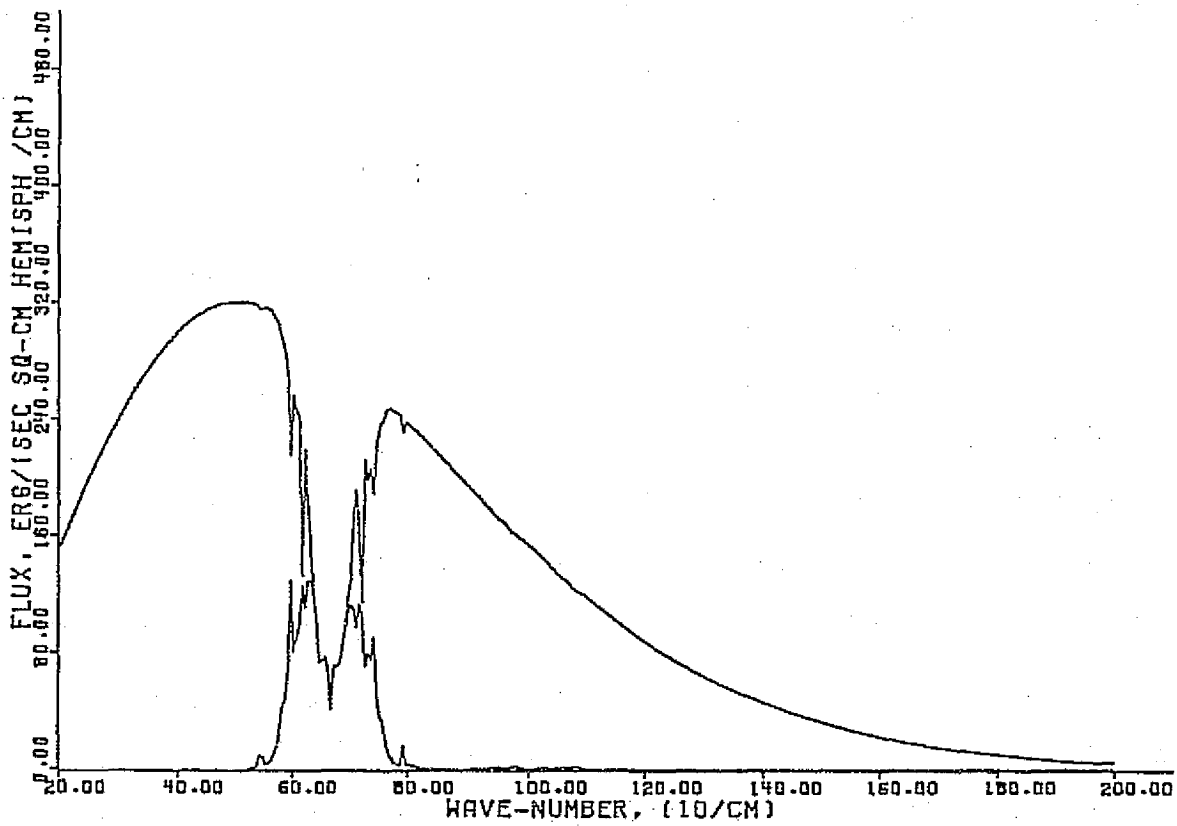

Fig. 8: Simulated flux originating from ground and atmospheric layers (upper curve) and strictly atmospheric contributions to flux at the top of Martian atmosphere (lower curve) versus wave-number; date and location: see Fig. 6.

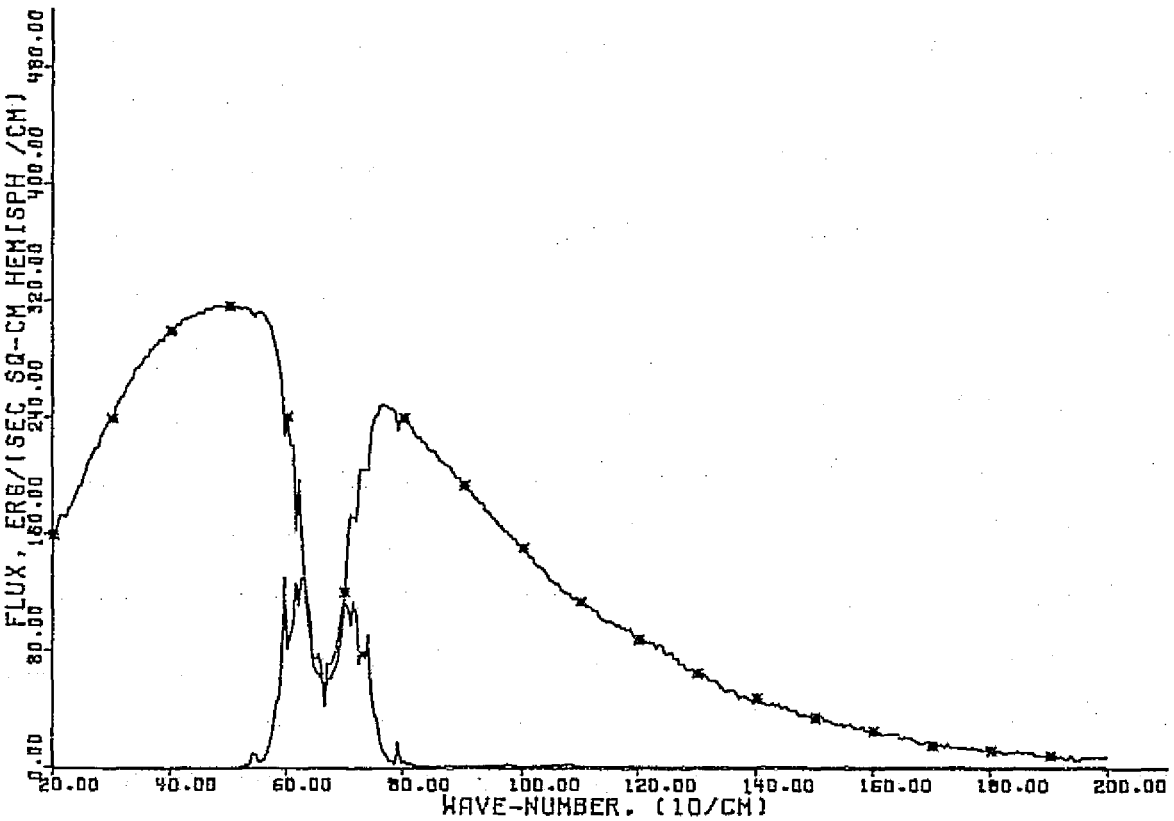

Fig. 9: Atmospheric component flux (lower curve) as simulated, and measured IRIS flux (*) versus wave number; date and location: see Fig. 6.

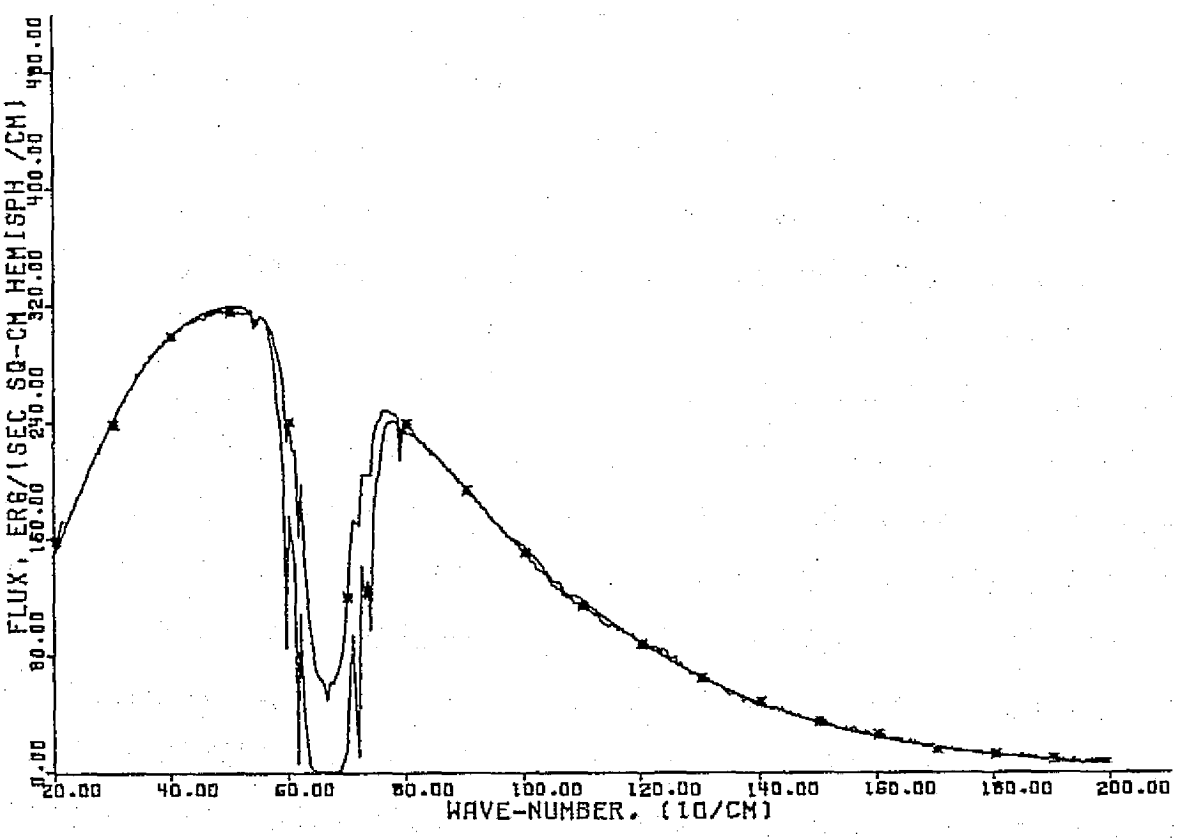

Fig. 10: Simulated ground flux, subsequently attenuated by atmosphere (solid curve) and measured IRIS flux (*) versus wave-number; date and location: see Fig. 6.

data in figure 10. The area between the 2 curves is equal to that under the lower curve of the previous figure. Outside the CO_2-absorption band, the IR radiation is almost completely transmitted to the atmospheric top. This is a sensible result if one keeps in mind that the model does not accommodate photon-matter interactions with minor constituents and the spectral dependence of emissivity of silicate dust at the ground.

In figure 11, the spectral flux transmissivity through the total depth of the atmosphere has been plotted. The decline of the curve below the value (1.0) is strictly dependent on atmospheric CO_2. Particular attention is called to the opacity from about 640 to 690 cm^{-1}.

In the remaining paragraphs of section 7.1, we will discuss some typical outputs, generated by our time-dependent M/T model, either used further as an input into the F/O-simulation or simply presented in their own right. The former procedure permits us to elucidate more the dependence of the F/O simulation on particular input data, whereas the latter may indicate the inherent capabilities of the M/T model. The program input parameters are given in Table 1.

After a time-integration over more than 300 time-steps, the M/T model produced temperature soundings (tautochrones) for atmosphere and soil in balance for a 24-hour cycle (cyclical balance). The atmospheric sounding which evolved

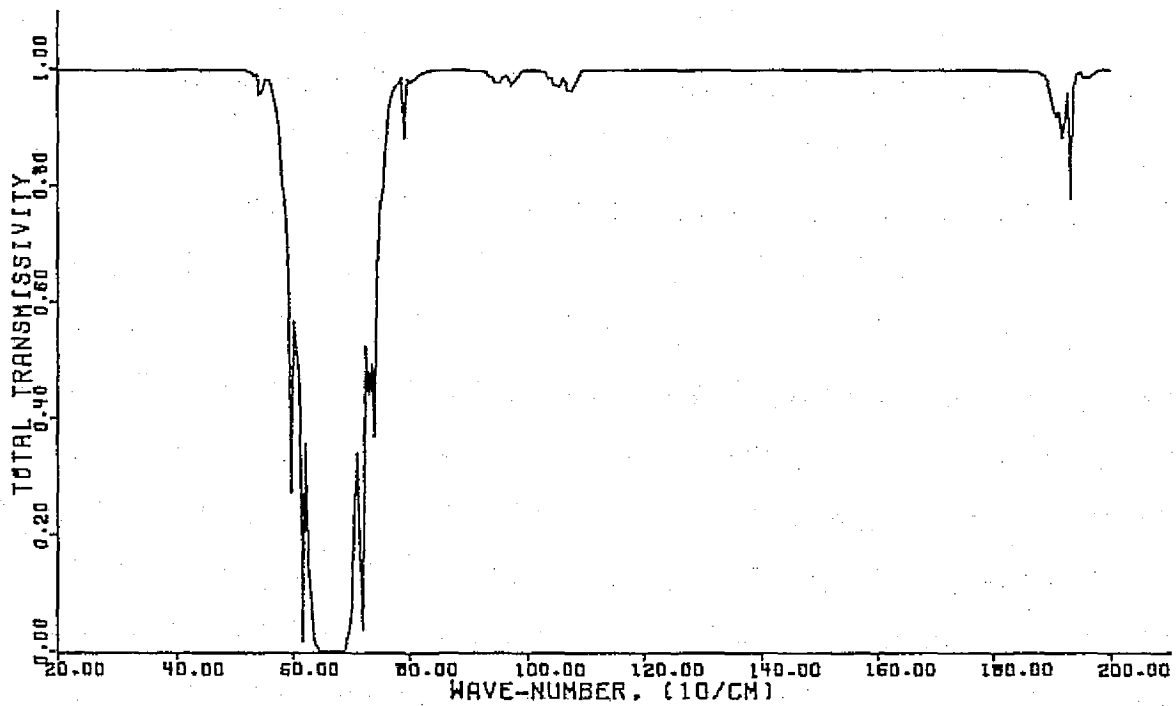

Fig. 11: Spectral transmissivity of IR flux, through total depth of atmosphere, versus wave-number. Further specifications: Fig. 6.

TABLE 1

FEBRUARY 16, 1972

MARTIAN ATMOSPHERE RAD-COND-CONV HEAT TRANSFER SIMULATION

PROGRAM PARAMETERS:

INITIAL TIME	12.720 LOCAL MARTIAN SOLAR TIME
NUMBER OF TIMESTEPS	400
TIMESTEP INTERVAL	10.000 MINUTES (MARTIAN)
	4.000 MINUTES (MARTIAN) FROM 13.00 TO 17.00
SURFACE ALBEDO	.300
SOIL DENSITY	1.500 GR/CU-CM
SOIL CONDUCTIVITY	2.300E 04 ERGS/(SEC CM DEG)
SOIL HEAT CAPACITY	1.005E ERGS/(CU-CM DEG)
CO2 CONDUCTIVITY	1.330E 03 ERGS/(SEC CM DEG)
LATITUDE	-41.40 DEG
DECLINATION OF SUN	-5.80 DEG
DURATION OF SUNSHINE	760.8 MINUTES (MARTIAN)
RATIO OF MEAN/ATUAL.	
SOLAR DISTANCE	1.0002
SURFACE PRESSURE	4.6 MB
DUST AMPLITUDE	0 /CM

ONE MARTIAN SOLAR DAY = 24 MARTIAN HOURS - 1440 MARTIAN MINUTES

ONE MARTIAN MINUTE = 61.6491 SECONDS

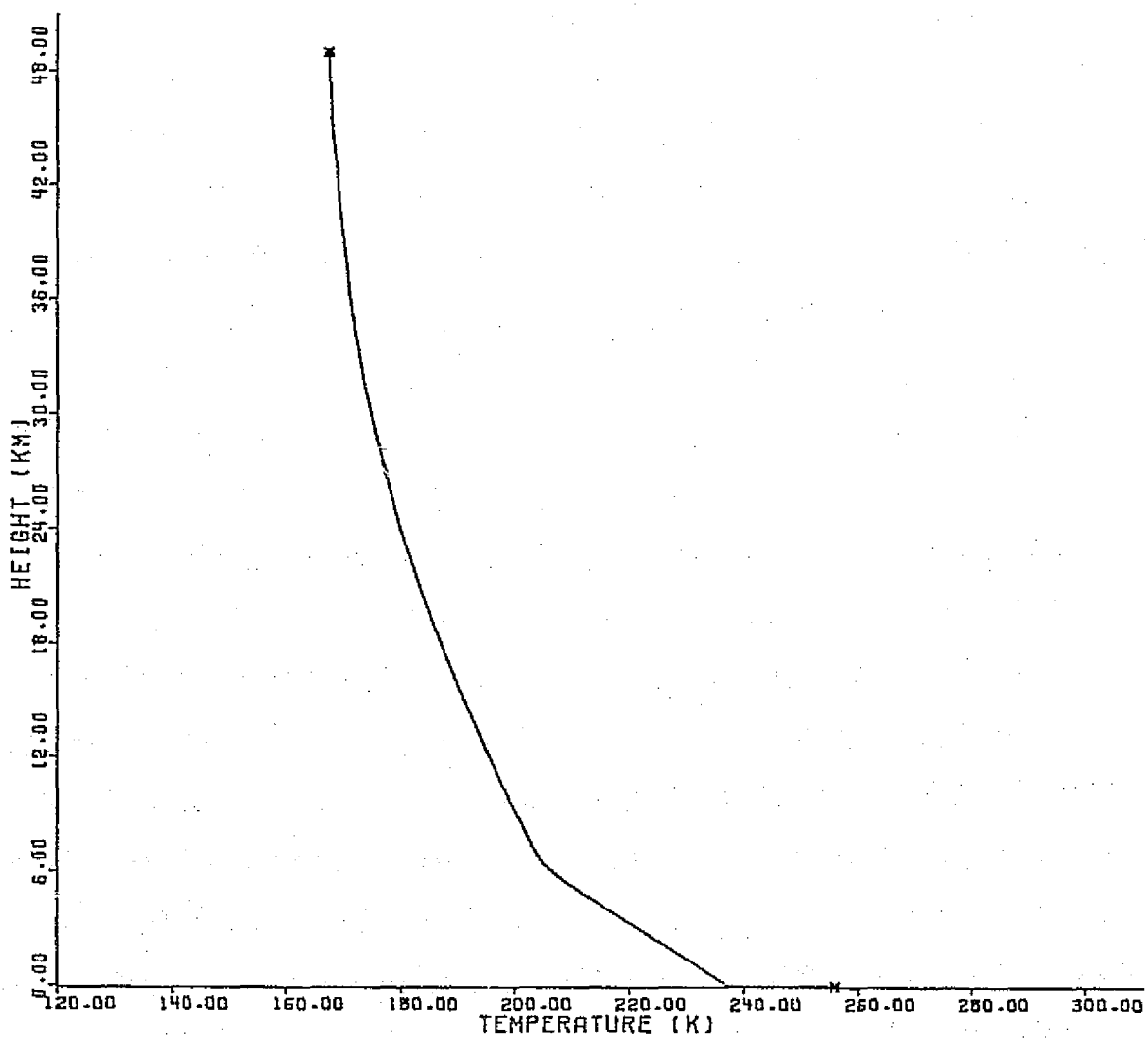

Fig. 12. Cyclically balanced temperature sounding vs. height, in simulation for February 16, 1972, 12.72 LMST, as input to the F/O program. For additional parameters, see table 1.

for simulation day 3, 12.72 LMST as cyclically balanced has been plotted in figure 12. Three distinct characteristics appear in the temperature distribution. First, in the surface boundary layer of 12.5 m of thickness, the temperature drops by about 19 K with a balanced T_s = 256K. By comparison, the drop in the IRIS-inverted temperature sounding of the same local time is steeper.

The second characteristic in figure 12 is the convective layer which extends with its adiabatic lapse rate to a height of about 6 km. This sublayer is not discernible in the IRIS-inverted temperature curve. Thirdly, the uppermost branch of the simulated T-function in figure 12 has the typical shape of temperature distribution for a layer in which radiative transfer is the predominant heat transport mechanism.

The dependence on wave-number of simulated spectral flux welling up at the top of the atmosphere, is illustrated in figure 13. The upper curve represents the contributions from ground and atmosphere duly attenuated by the intervening layers. The exclusive contribution to outward flux by the atmospheric strata is shown by the lower curve. The difference between the two curves at any wave-number indicates how much of the IR radiation, emitted by the ground surface, reaches the top of the atmosphere.

Figure 14 mainly demonstrates the consequence of different surface temperatures implicit in the IRIS spectrum (261.8K)

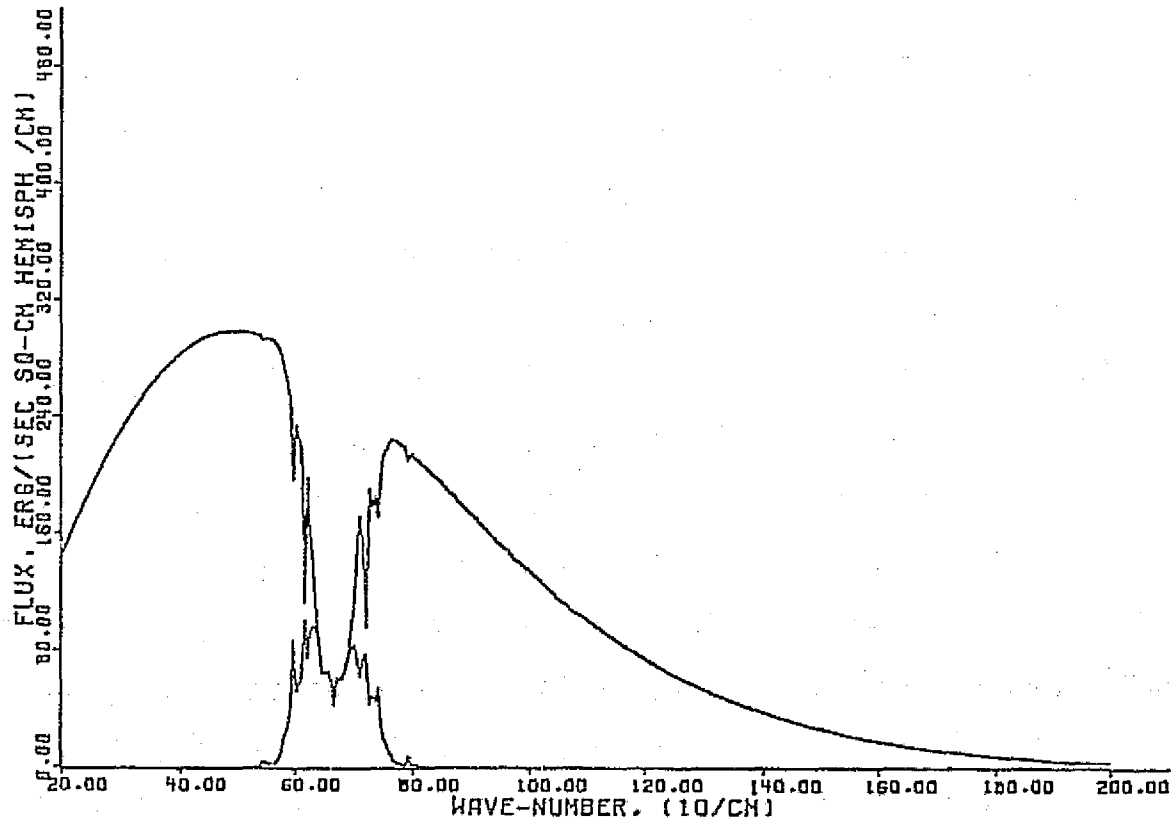

Fig. 13. F/O-simulated upwelling flux in ergs/(sec cm^2 hemisph/cm) vs. wave number in (10/cm) for February 16, 1972, 12.72 LMST. Upper curve: flux from ground and atmosphere combined; lower curve: exclusively atmospheric contribution to flux. For additional parameters, see table 1.

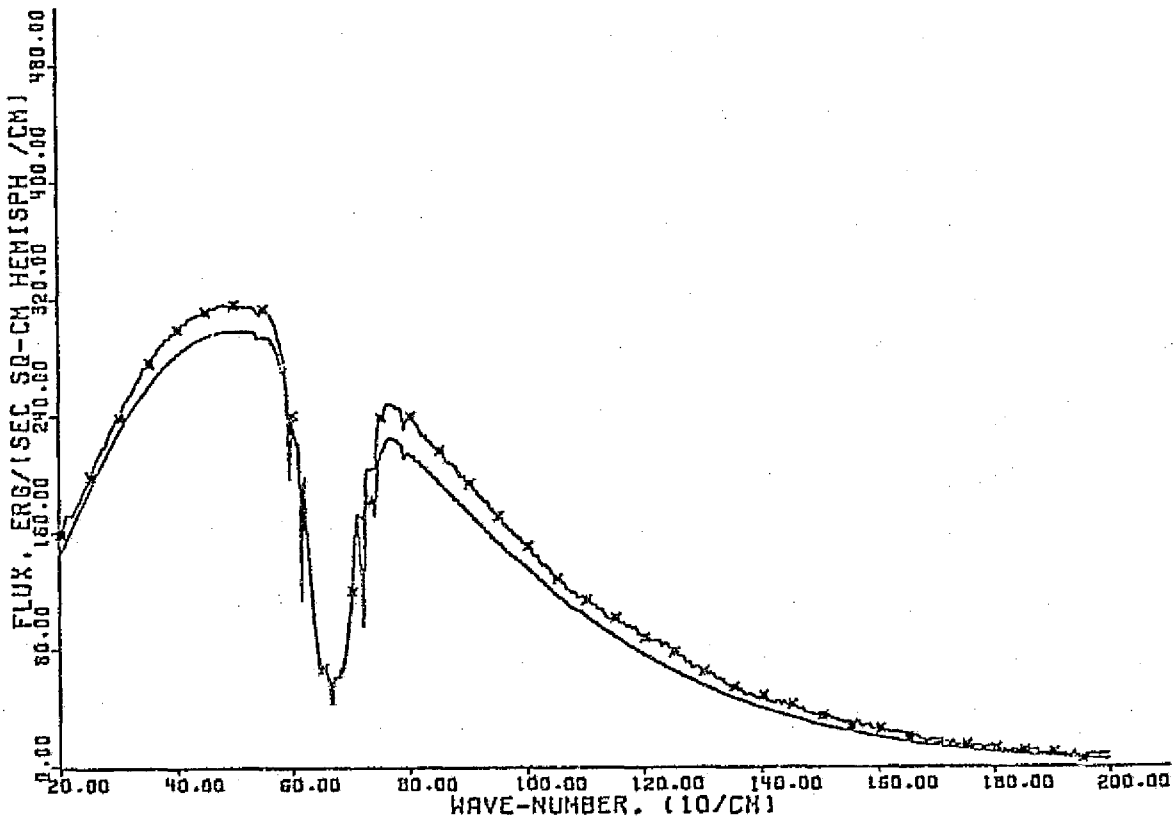

Fig. 14. F/O simulated (solid curve) and IRIS-measured (*) upwelling flux, in ergs/(sec cm^2 hemisph/cm) vs. wave number in (10/cm) for February 16, 1972, 12.72 LMST. For additional parameters, see table 1.

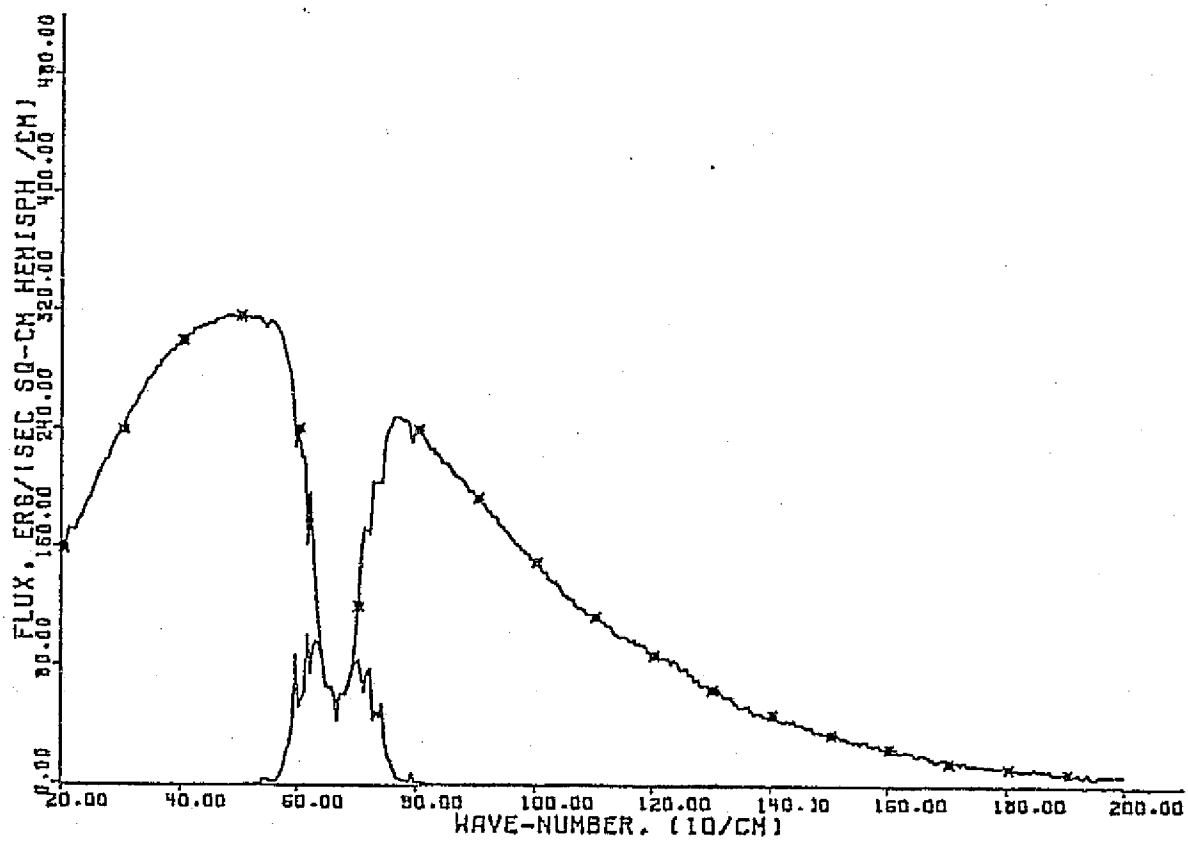

Fig. 15. F/O-simulated atmospheric contribution (lower curve) and IRIS-measured (*) upwelling flux in ergs/(sec cm^2 hemisph/cm) vs. wave number in (10/cm) for February 16, 1972, 12.72 LMST for additional parameters, see table 1; T_s = 256K.

and the cyclically balanced simulation spectrum (256K). In the center of the CO_2 absorption band, the two curves coincide. A comparison of the simulated atmospheric component flux with the measured IRIS flux spectrum is facilitated in figure 15. Between about 640 and 690 cm^{-1}, the upwelling radiation is strictly originating from the atmosphere. No ground emission reaches the top of the atmosphere.

As to the direct M/T model outputs for the dust-free condition of the southern-hemispheric midlatitudes, the gradual evolution toward cyclical balance may be recognized in figures 16 and 17. In both figures, four-hourly atmospheric temperature soundings are presented. The sequence begins with the IRIS-inverted T-sounding at 12.72 LMST of February 16, 1975 and T_s = 259.5K (IRR brightness temperature) as input.

Figure 16 shows as the last four-hourly sounding the curve at 12:00 LMST of day 2. Figure 17 is the continuation completing the second diurnal cycle at 12.72 LMST. It is evident that the curves of the second cycle stay closer together, particularly between 4 and 10 km. The surface temperature spread covers about 70K. The greatest thickness of the convective layer is reached at 12.72 LMST of day 3 with 6 km.

The first and last T-sounding may be compared in figure 18. Since the sounding of day 3 is close to the 24-hour cyclical balance, we submit that it is more representative of

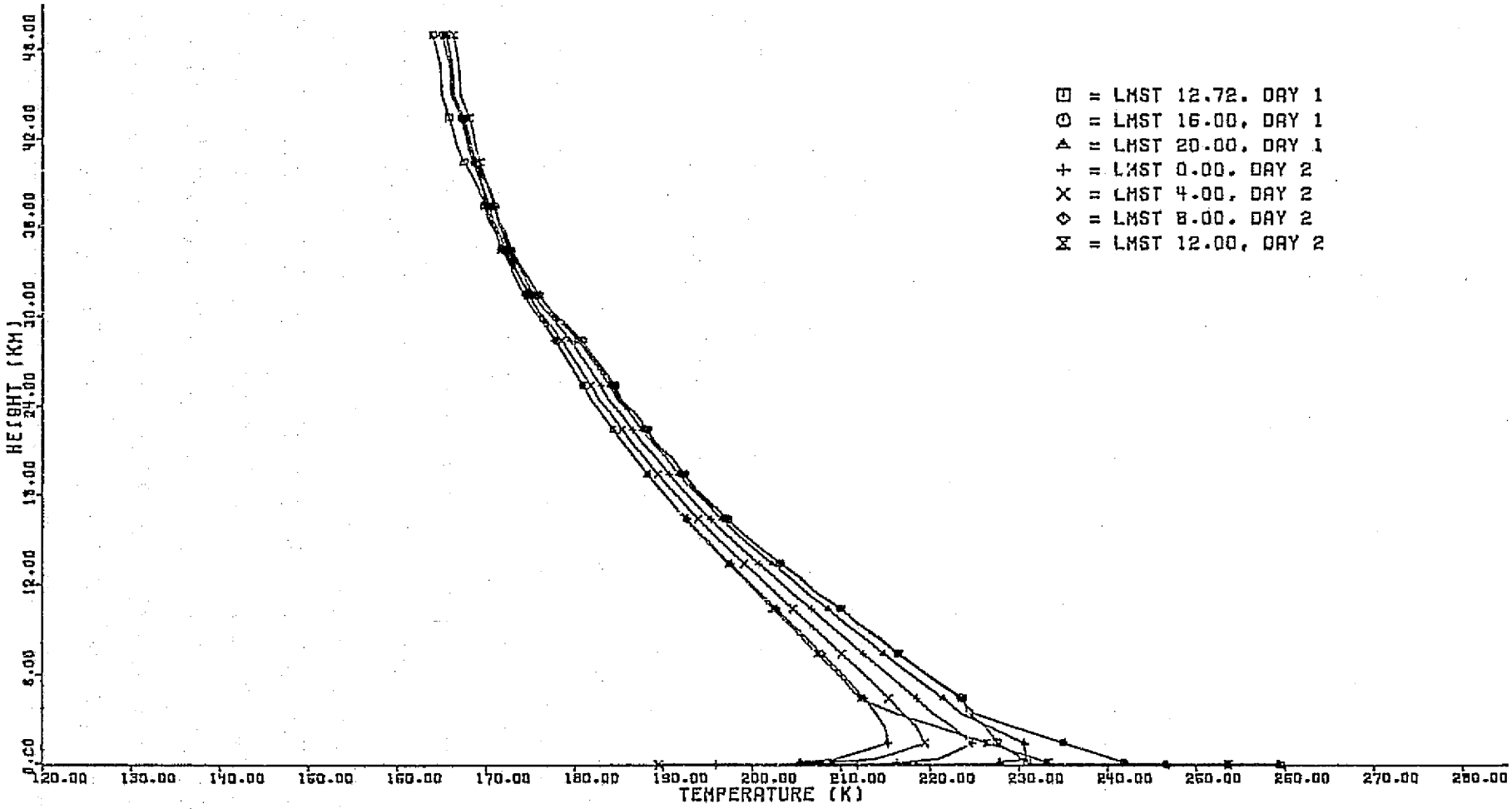

Fig. 16. M/T-simulated four-hourly atmospheric temperature soundings in degrees K vs. height in km for February 16, 1972, 12.72 LMST. Sequence of 24 hours begins with IRIS-inverted sounding and proceeds as indicated by markers (upper right). For additional parameters, see table 1.

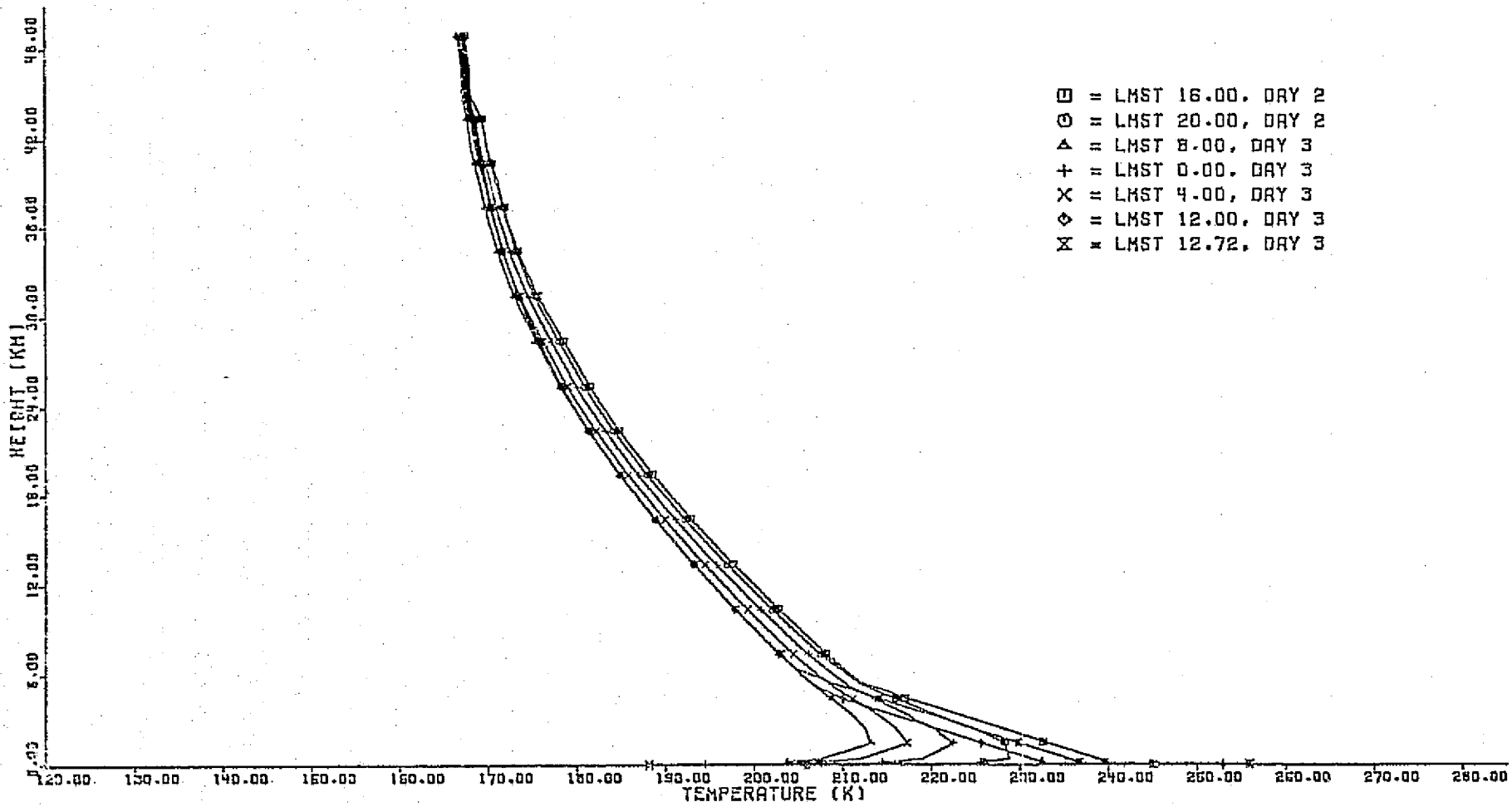

Fig. 17. Continuation of M/T-simulated four-hourly atmospheric temperature soundings in degrees K vs. height in km for February 16, 1972, 12.72 LMST. Sequence of 24 hours begins with IRIS-inverted sounding and proceeds as indicated by markers (upper right). For additional parameters, see table 1.

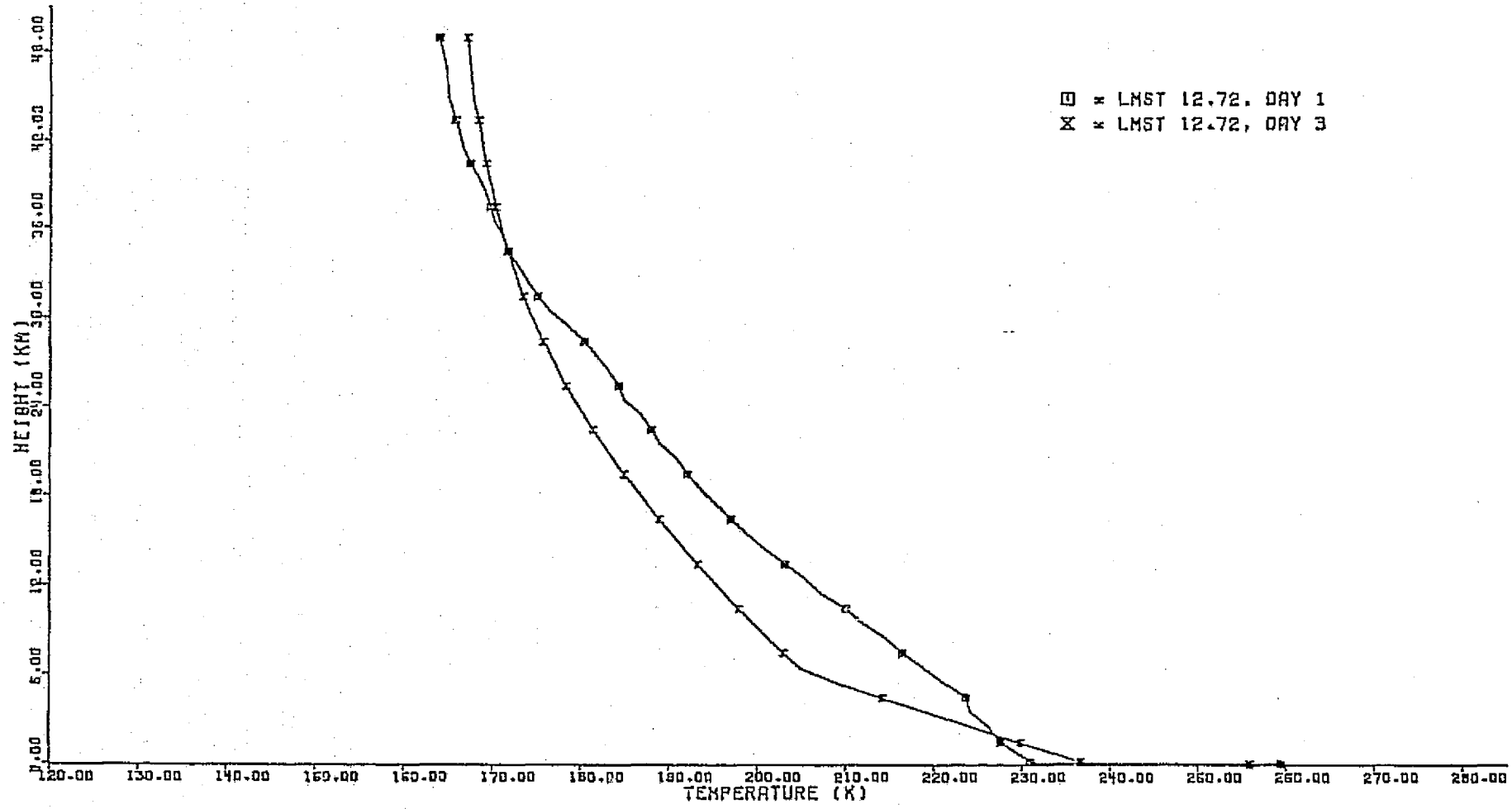

Fig. 18. Initial and final soundings from the 48 hour M/T simulation, in degrees K vs. height in km, for February 16, 1972, 12.72 LMST. Markers (upper right) specify the times. For additional parameters, see table 1.

the thermal stratification in the southern-hemispheric mid-latitudes near the end of the summer season. The largest differences of temperature for these two soundings are between 4 and 25 km of height with up to 15K. As mentioned earlier, the temperature spread in the surface boundary layer, from 0 to 12.5 m, is about one third smaller for the M/T simulated sounding or about 20K.

In figures 19 and 20, the four-hourly tautochrones (see Geiger, 1966) are presented for the period of 48 hours. The higher vertical resolution in scale reveals more detail. Steep near-surface inversions of up to 30K are discernible near sunrise. During the afternoon, the thickness of the convection layer clearly goes beyond 1,500 m. As to the subsurface strata, below 60 cm the temperatures are assumed constant and equal to 222K. Figure 21 facilitates comparison between the initial and the final tautochrone. One may be mindful of the limited vertical resolving power of the integral inversion technique which was applied to measured IRIS spectra in order to obtain temperature soundings (Conrath, 1974; see also chapter 5).

7.2 ATTUNED MODEL OUTPUTS, MODERATE DUST-LOAD

By inserting the height-dependent effective dust absorption coefficient for December 24, 1971 (chapter 4) in the transmission function of both the F/O- and the M/T-simulation programs, we generated a variety of appropriate outputs which

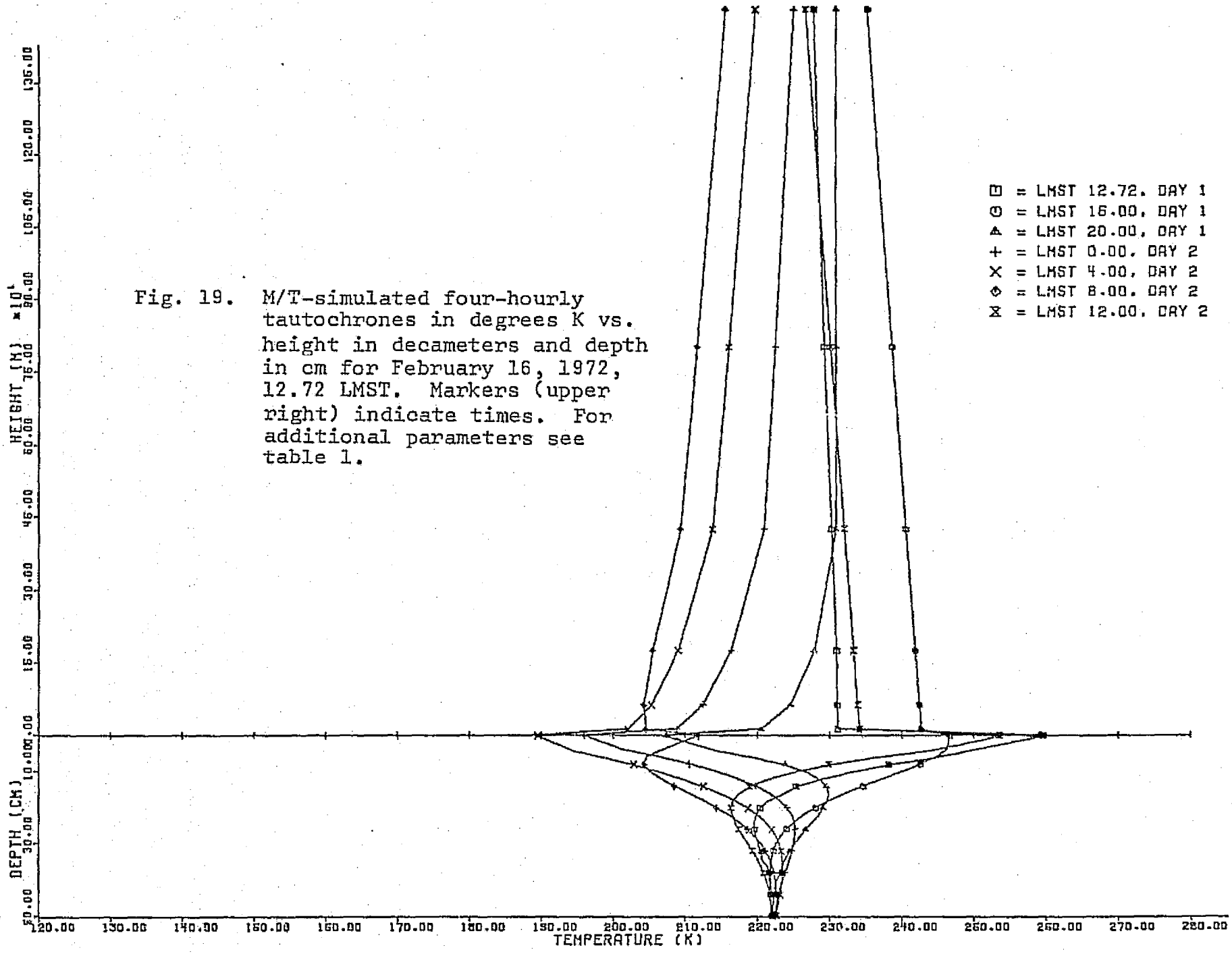

Fig. 19. M/T-simulated four-hourly tautochrones in degrees K vs. height in decameters and depth in cm for February 16, 1972, 12.72 LMST. Markers (upper right) indicate times. For additional parameters see table 1.

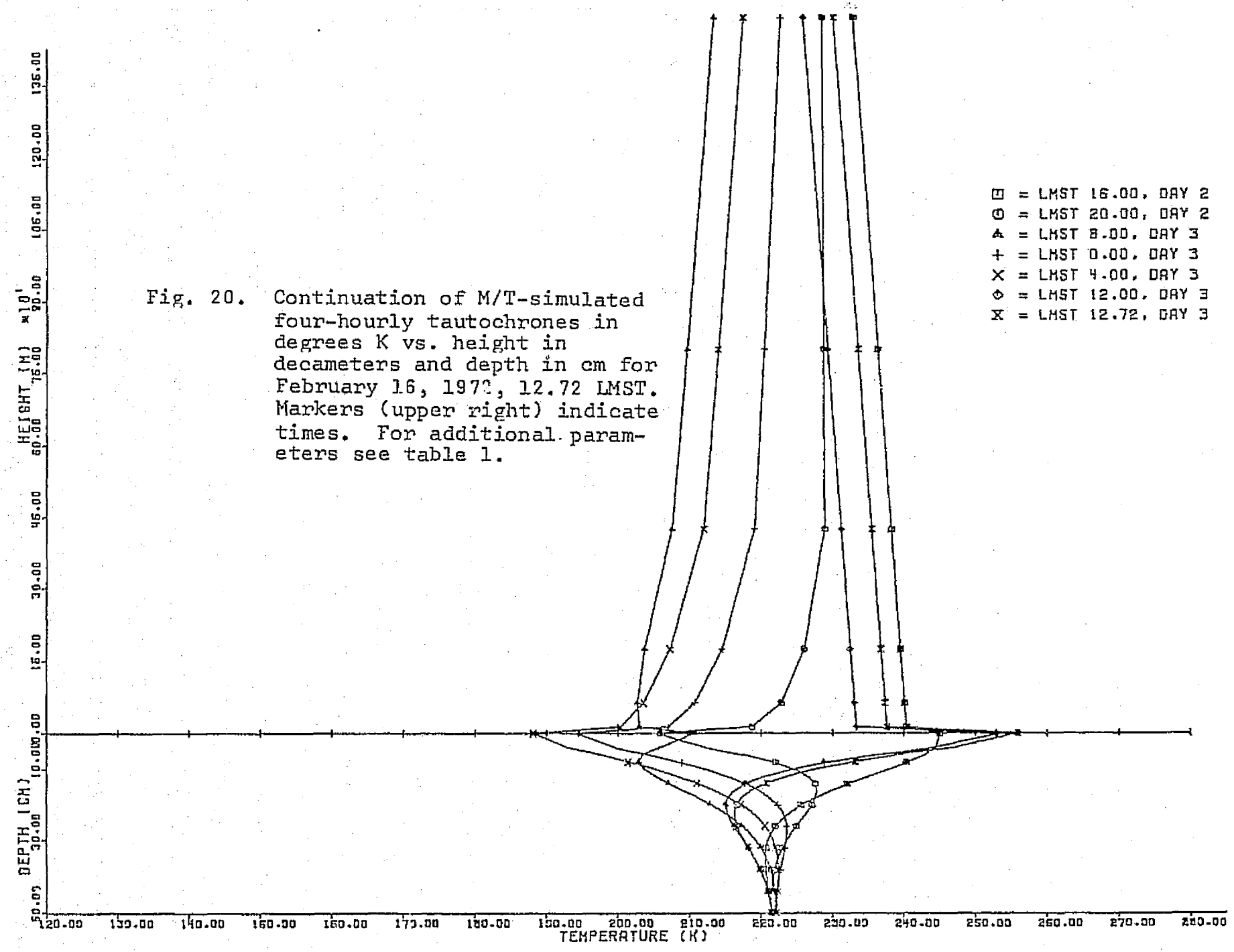

Fig. 20. Continuation of M/T-simulated four-hourly tautochrones in degrees K vs. height in decameters and depth in cm for February 16, 1972, 12.72 LMST. Markers (upper right) indicate times. For additional parameters see table 1.

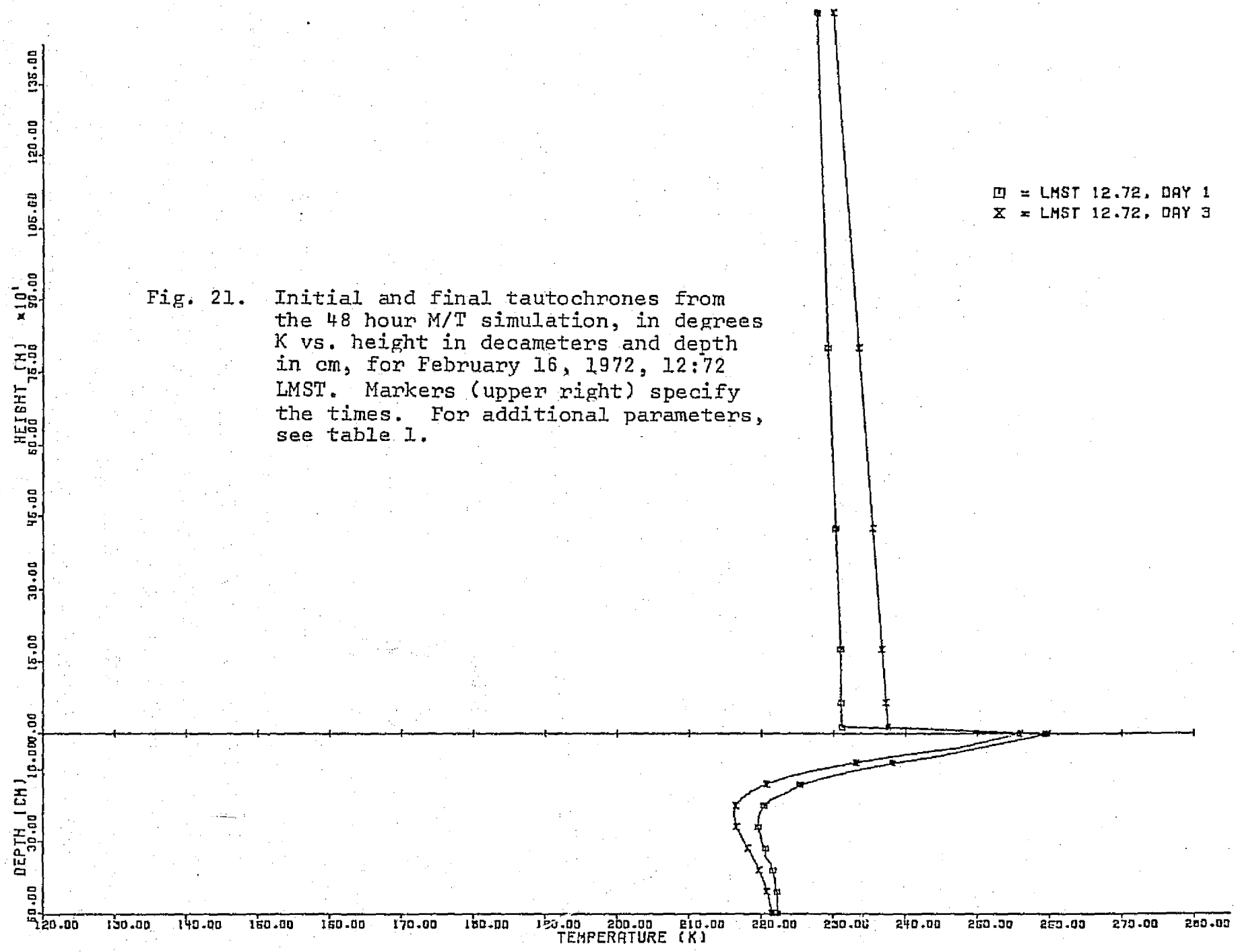

Fig. 21. Initial and final tautochrones from the 48 hour M/T simulation, in degrees K vs. height in decameters and depth in cm, for February 16, 1972, 12:72 LMST. Markers (upper right) specify the times. For additional parameters, see table 1.

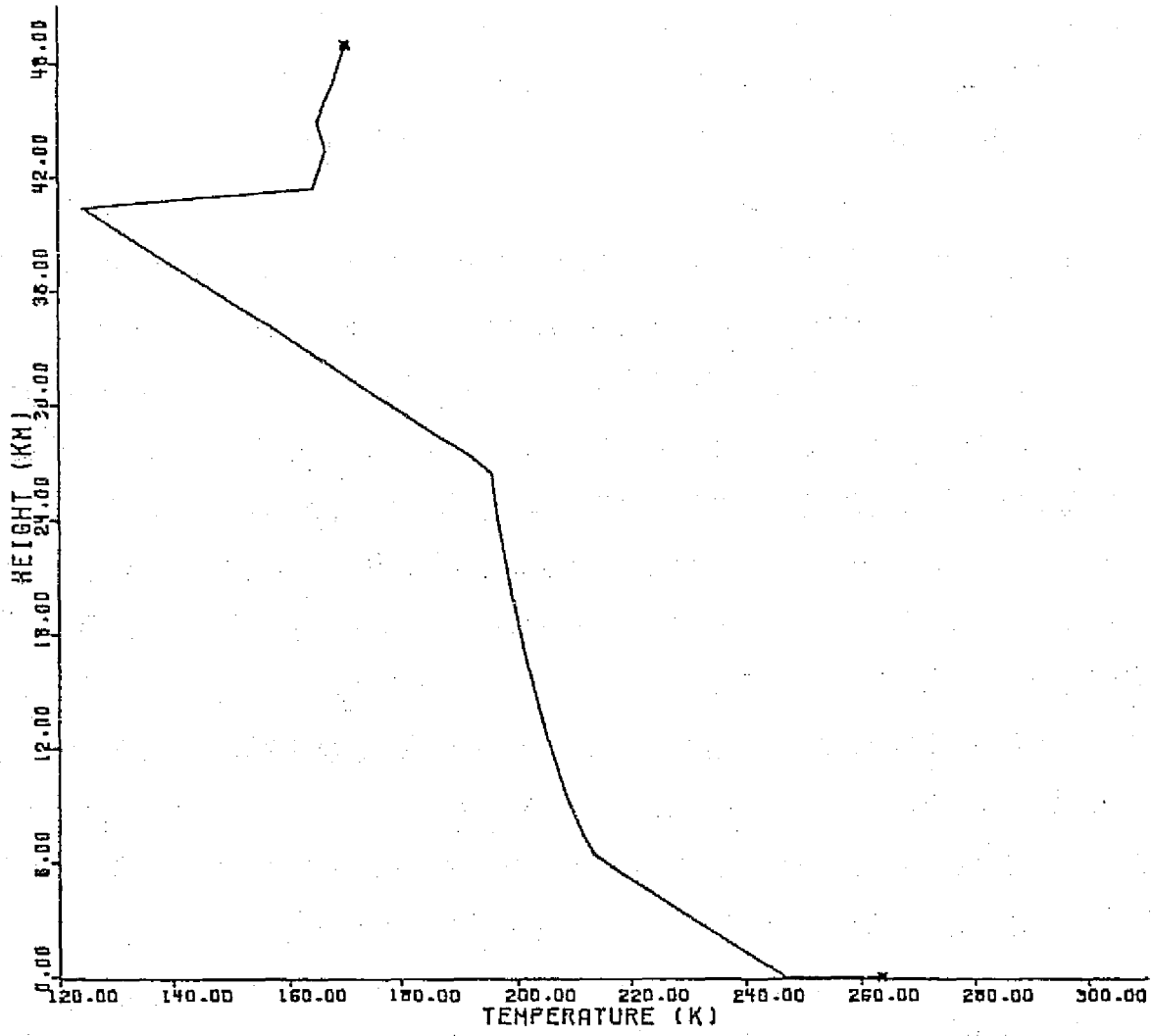

Fig. 22. Cyclically balanced temperature sounding vs. height, in simulation for December 24, 1971, 14.05 LMST, as input to the F/O program. For additional parameters, see table 2.

were plotted via CALCOMP. The coefficient used to describe the effective absorption by dust was $(1.2 \times 10^{-7} \cdot \exp(-1.11 \times 10^{-9} \cdot Z^2))$ cm^{-1}. For further detail, see section 4.3 of this report.

In the subsequent paragraphs, we will again present first some results generated by the F/O-program followed by outputs pertinent to the M/T-model. The temperature sounding used as input for the F/O-simulation is given by figure 22. It is as before a cyclically balanced sounding at 14.05 LMST The surface temperature reads T_s = 264K; and, within the surface boundary layer, a decline of 14K is discernible. There are two layers of convective overturn, one up to about 6.5 km and the other from the top of the dust layer at 40 km down to about 27 km or twice as deep. At the top of the dust layer, the temperature is only 124K, a value gradually reached by the model in its trend toward a balance over a 24-hour cycle.

The effective dust absorption coefficient is presented in figure 23. As stated earlier, the mathematical form of this function is Gaussian with a drop-off at 40 km (top of dust layer). In figure 24, the simulated flux is compared with the measured IRIS spectrum for this date. It is evident that the thermal level of the simulation curve is lower as a consequence of the reduced surface temperature in cyclical balance. Details of comparison within the CO_2 absorption band will be offered in section 7.3 which covers the optically thicker dust condition.

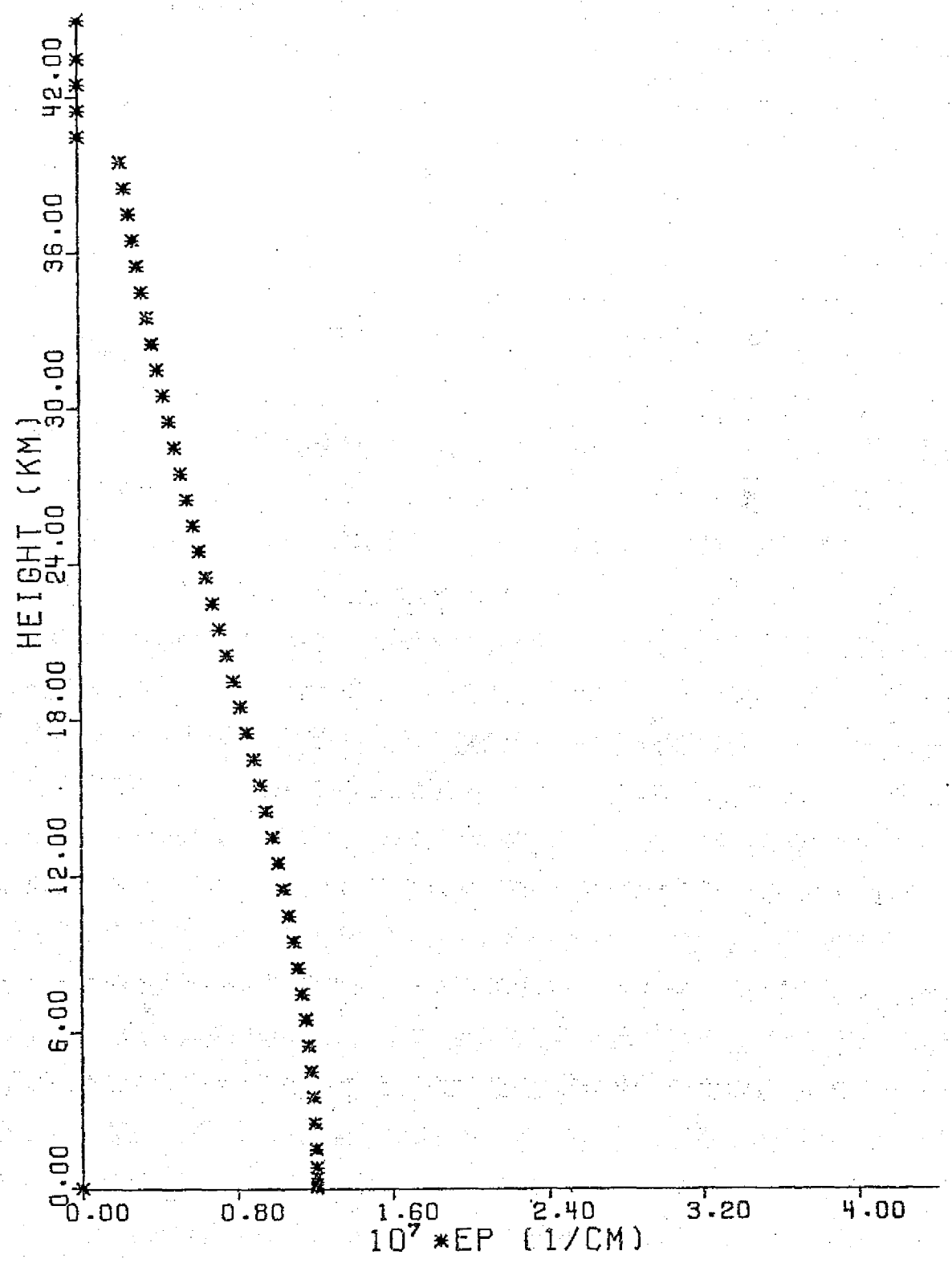

Fig. 23. Effective dust absorption coefficient in 10^{-7} cm^{-1} vs. height in km, for December 24, 1971, 14.05 LMST. Top of the dust layer located at 40 km. For additional parameters, see table 2.

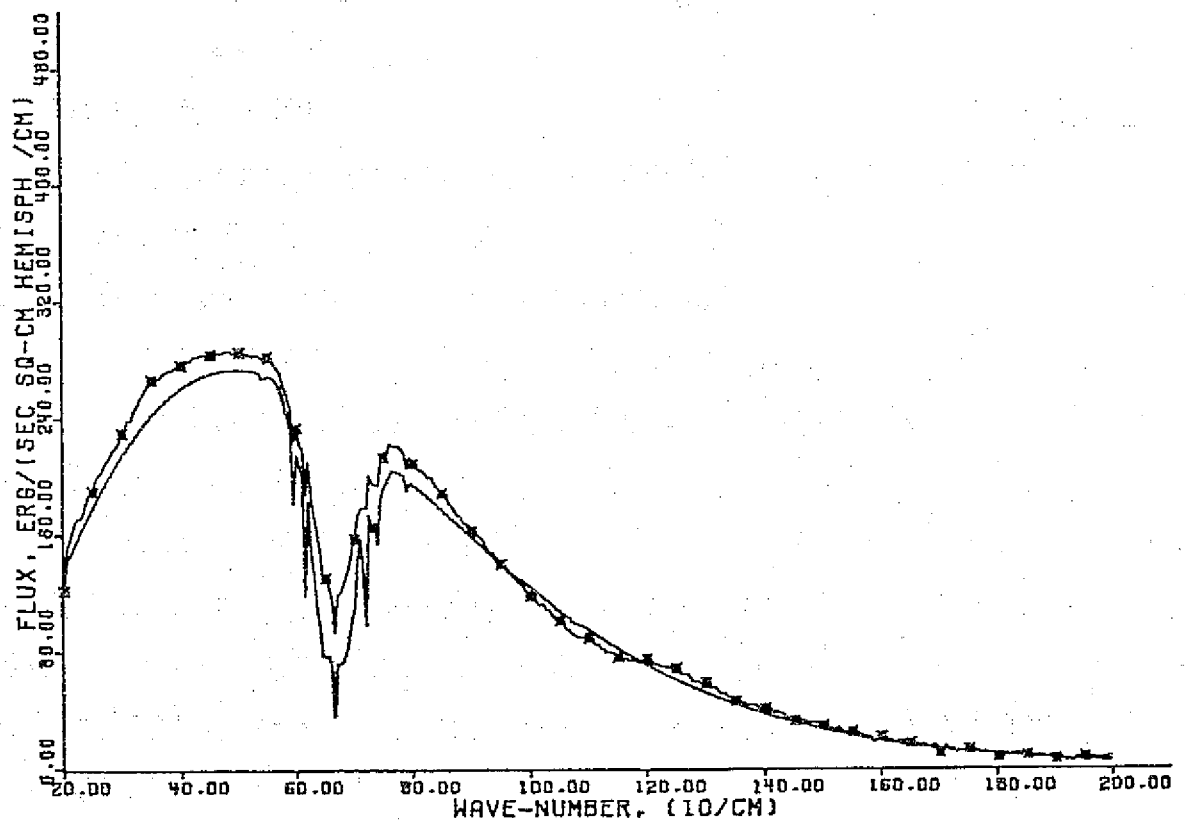

Fig. 24. F/O-simulated (solid curve) and IRIS-measured (*) upwelling flux, in ergs/(sec cm^2 hemisph/cm) vs. wave number in (10/cm) for December 24, 1971, 14.05 LMST. For additional parameters, see table 2.

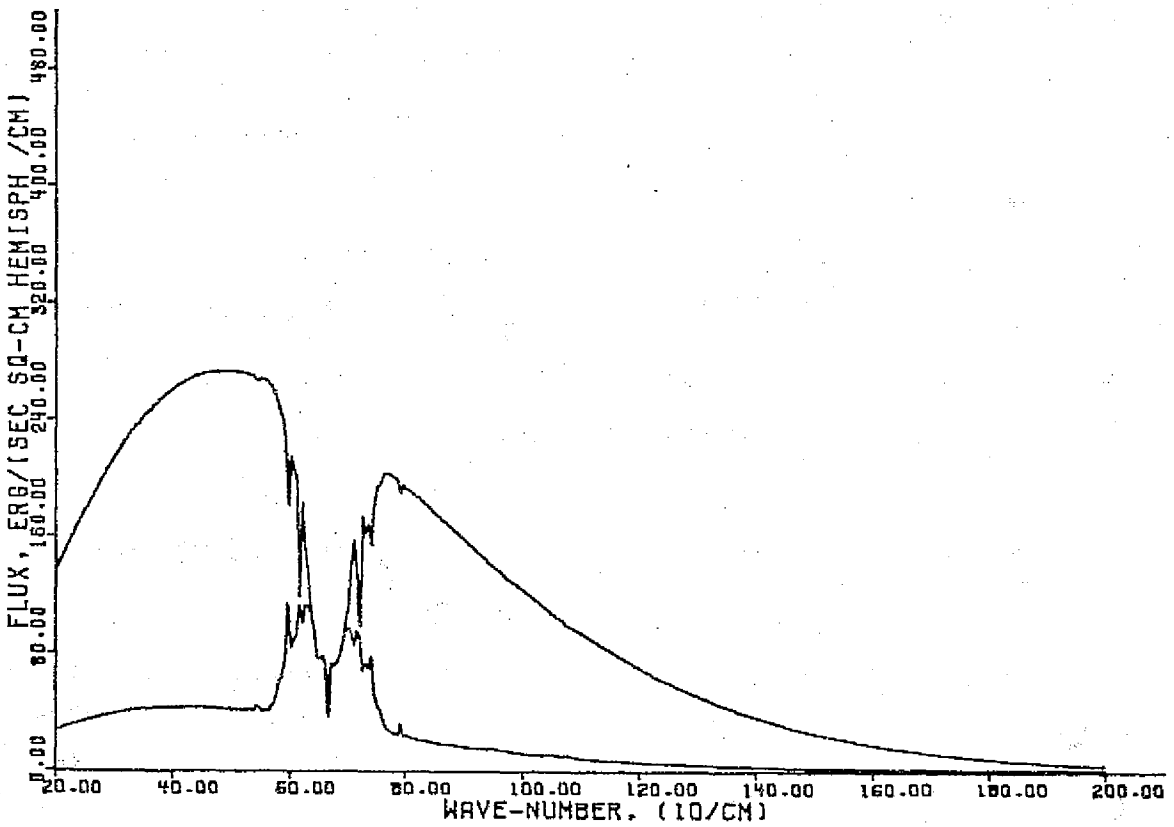

Fig. 25. F/O-simulated upwelling flux in ergs/(sec cm^2 hemisph/cm) vs. wave number in (10/cm) for December 24, 1971, 14.05 LMST. Upper curve: flux from ground and atmosphere combined; lower curve: exclusively atmospheric contribution to flux. For additional parameters, see table 2.

In figure 25, the simulated flux from ground and atmosphere together with just the atmospheric contribution are shown. Outside the CO_2 absorption band, centered at 667 cm^{-1}, the involvement of the dust is clearly evident. A Planckian function of low temperature can be found to represent effectively the dust emissions. Again the highest thermal levels of the atmospheric emission upward may be recognized in the middle of the two wings of the CO_2 band. The transmission capability, integrated over the entire depth of the atmosphere is shown in figure 26 as a function of wave number.

In the remaining paragraphs of the section, typical outputs of the M/T-simulation are to be presented. The program input parameters are given in Table 2. The four hourly temperature soundings over a time period of 48 hours are illustrated in figures 27 and 28. Similar to the dust-free condition on February 16, 1972 (figures 16 and 17), a trend toward cyclical balance is discernible. The evolving temperature sounding was discussed above in conjunction with the F/O-simulation of December 24, 1971.

Four regimes may be distinguished in figure 28, i.e., the planetary boundary layer with either nocturnal inversions or convection around local noon, the layer from 6.5 to 27 km with hydrostatic stability, the second convection layer between 27 and 40 km, and finally a very stable layer topping the dust stratum. By comparing the thermal characteristics between 12 and 30 km with those for the dust-free situation

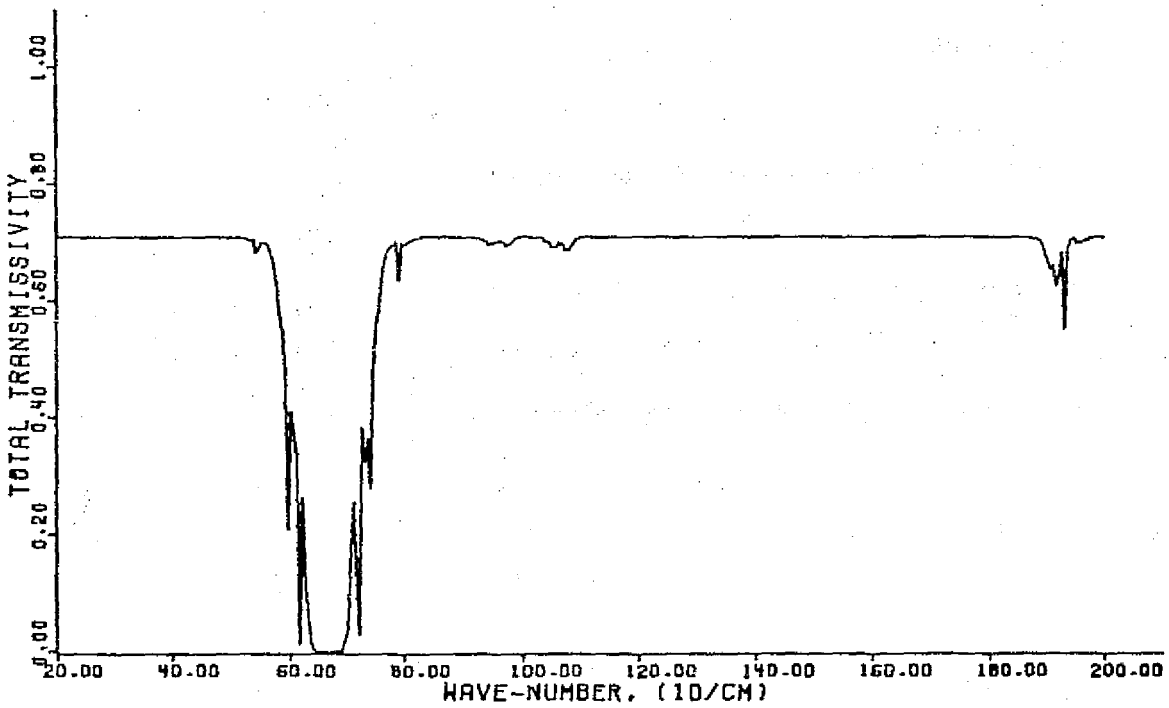

Fig. 26. Spectral transmissivity, for the entire depth of the atmosphere, vs. wave number in (10/cm) for December 24, 1971, 14.05 LMST. For additional parameters, see table 2.

TABLE 2

DECEMBER 24, 1971

MARTIAN ATMOSPHERE RAD-COND-CONV HEAT TRANSFER SIMULATION

PROGRAM PARAMETERS:

INITIAL TIME	14.050 LOCAL MARTIAN SOLAR TIME
NUMBER OF TIMESTEPS	300
TIMESTEP INTERVAL	10.000 MINUTES (MARTIAN)
	4.000 MINUTES (MARTIAN) FROM 13.00 to 17.00
SURFACE ALBEDO	.300
SOIL DENSITY	1.500 GR/CU-CM
SOIL CONDUCTIVITY	2.300E 04 ERGS/(SEC CM DEG)
SOIL HEAT CAPACITY	1.005E ERGS/(CU-CM DEG)
CO2 CONDUCTIVITY	1.330E 03 ERGS/(SEC CM DEG)
LATITUDE	-54.00 DEG
DECLINATION OF SUN	-16.20 DEG
DURATION OF SUNSHINE	913.1 MINUTES (MARTIAN)
RATIO OF MEAN/ATUAL.	
SOLAR DISTANCE	1.0483
SURFACE PRESSURE	4.8 MB
DUST AMPLITUDE	1.200F-07 /CM

ONE MARTIAN SOLAR DAY = 24 MARTIAN HOURS - 1440 MARTIAN MINUTES

ONE MARTIAN MINUTE = 61.6586 SECONDS

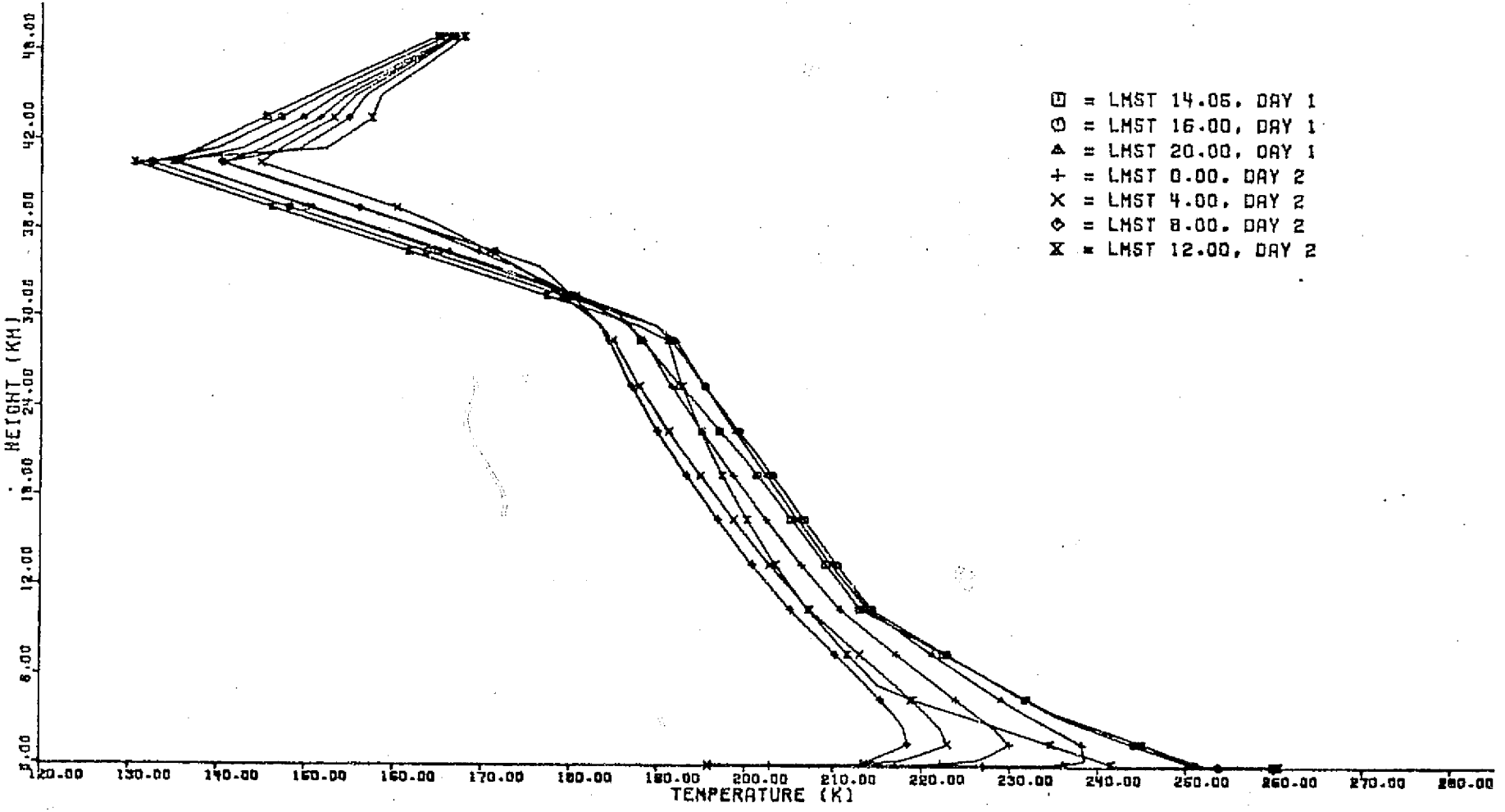

Fig. 27. M/T-simulated four-hourly atmospheric temperature soundings in degrees K vs. height in km for December 24, 1971, 14.05 LMST. Sequence of 24 hours begins with IRIS-inverted sounding and proceeds as indicated by markers (upper right). For additional parameters, see table 2.

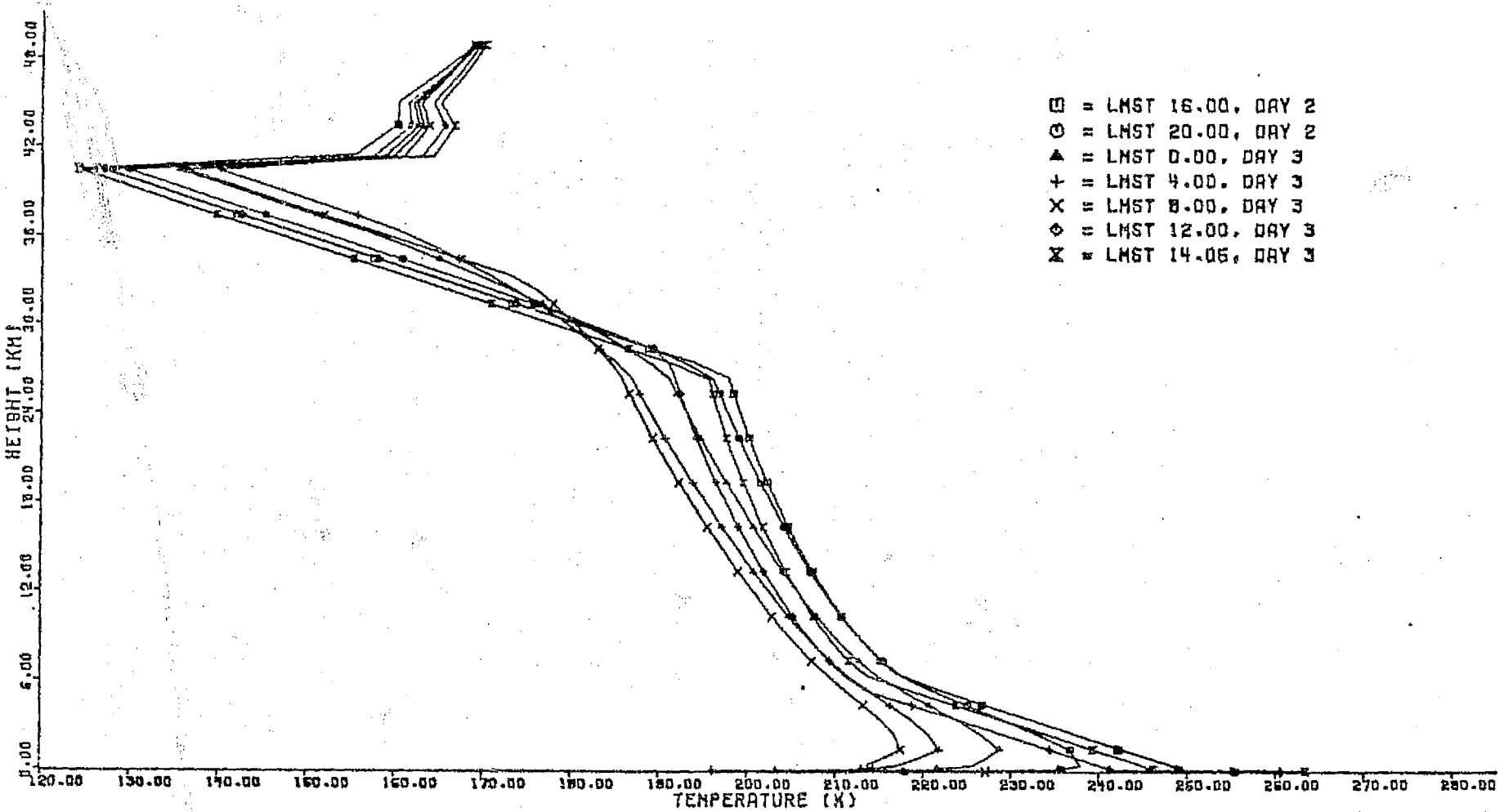

Fig. 28. Continuation of M/T-simulated four-hourly atmospheric temperature soundings in degrees K vs. height in km for December 24, 1971, 14.05 LMST. Sequence of 24 hours begins with IRIS-inverted sounding and proceeds as indicated by markers (upper right). For additional parameters, see table 2.

to 20K due to the presence of dust. The intense cooling near the dust top which is related to the discontinuity of the radiatively active material concentrations, may be partially caused by the particular modeling procedure about that level.

In figures 29 and 30, the four-hourly tautachrones for December 24 are plotted. Because of the higher vertical resolution, detailed structure characteristics of the nocturnal temperature inversions or convective stratification appear. The thermal conduction in the soil depends on the values of various related parameters, given in TABLE 2. Initial and final soundings of this time-dependent run are fairly similar because a simulated sounding was used as input.

7.3 ATTUNED MODEL OUTPUTS, OPTICALLY-THICK DUST-LOAD

The day of November 22, 1971 was chosen to represent the condition of the optically-thick dust-load in the southern-hemispheric mid-latitudes. The particular value chosen for the height-dependent coefficient of effective absorption by dust particulates was $(3.0 \times 10^{-7}.\exp(-1.11 \times 10^{-9}.Z^2))$ cm^{-1}. It determined the effective dust transmission, as discussed in chpt. 4 of this report. Its height-dependence is illustrated in figure 31. A sharp drop-off is discernible at 40 km marking the adopted top of the dust-layer.

The input sounding for the F/O-simulation is shown in figure 32. This temperature sounding is the result of more than 300 time-integrations with the M/T-program. Cyclical

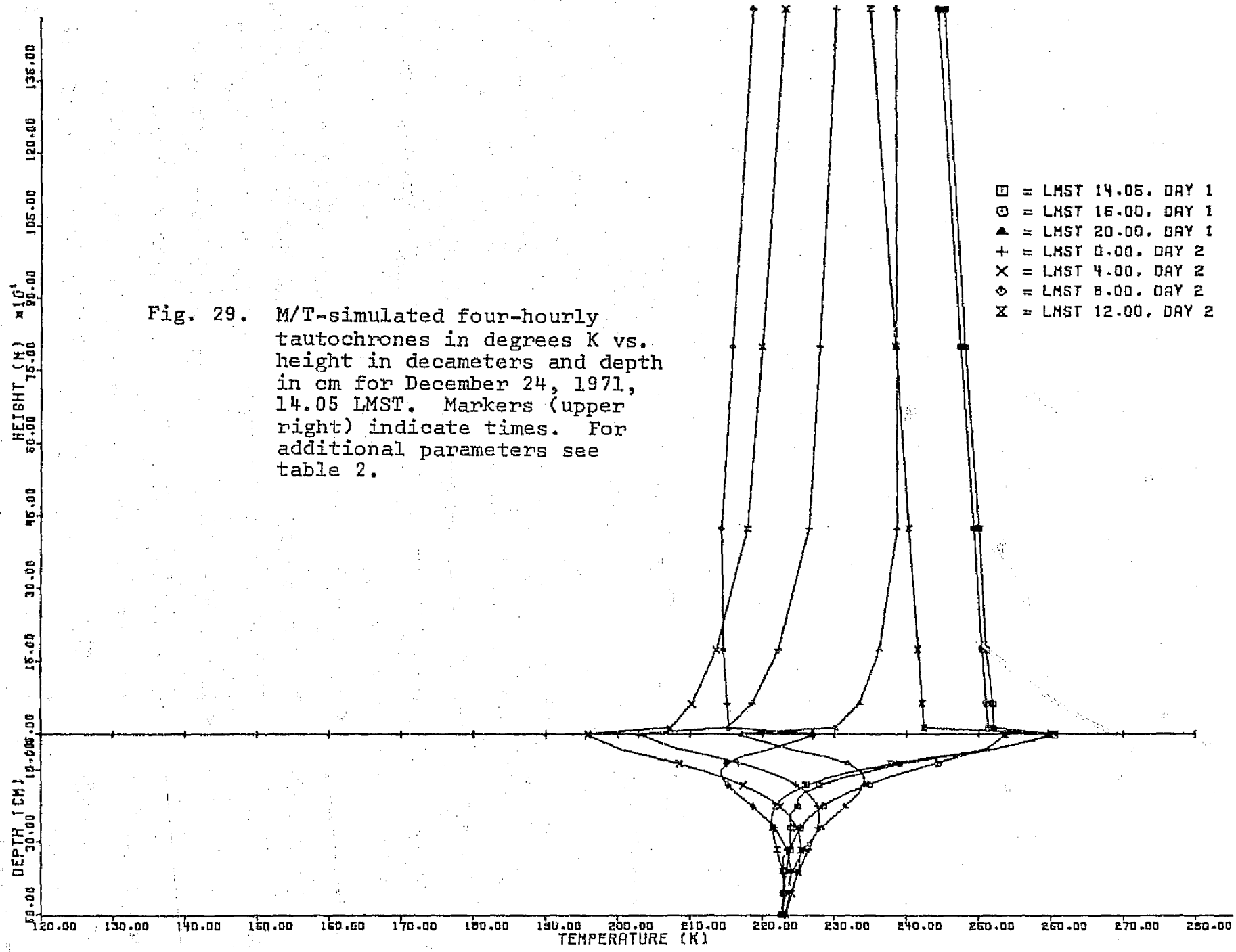

Fig. 29. M/T-simulated four-hourly tautochrones in degrees K vs. height in decameters and depth in cm for December 24, 1971, 14.05 LMST. Markers (upper right) indicate times. For additional parameters see table 2.

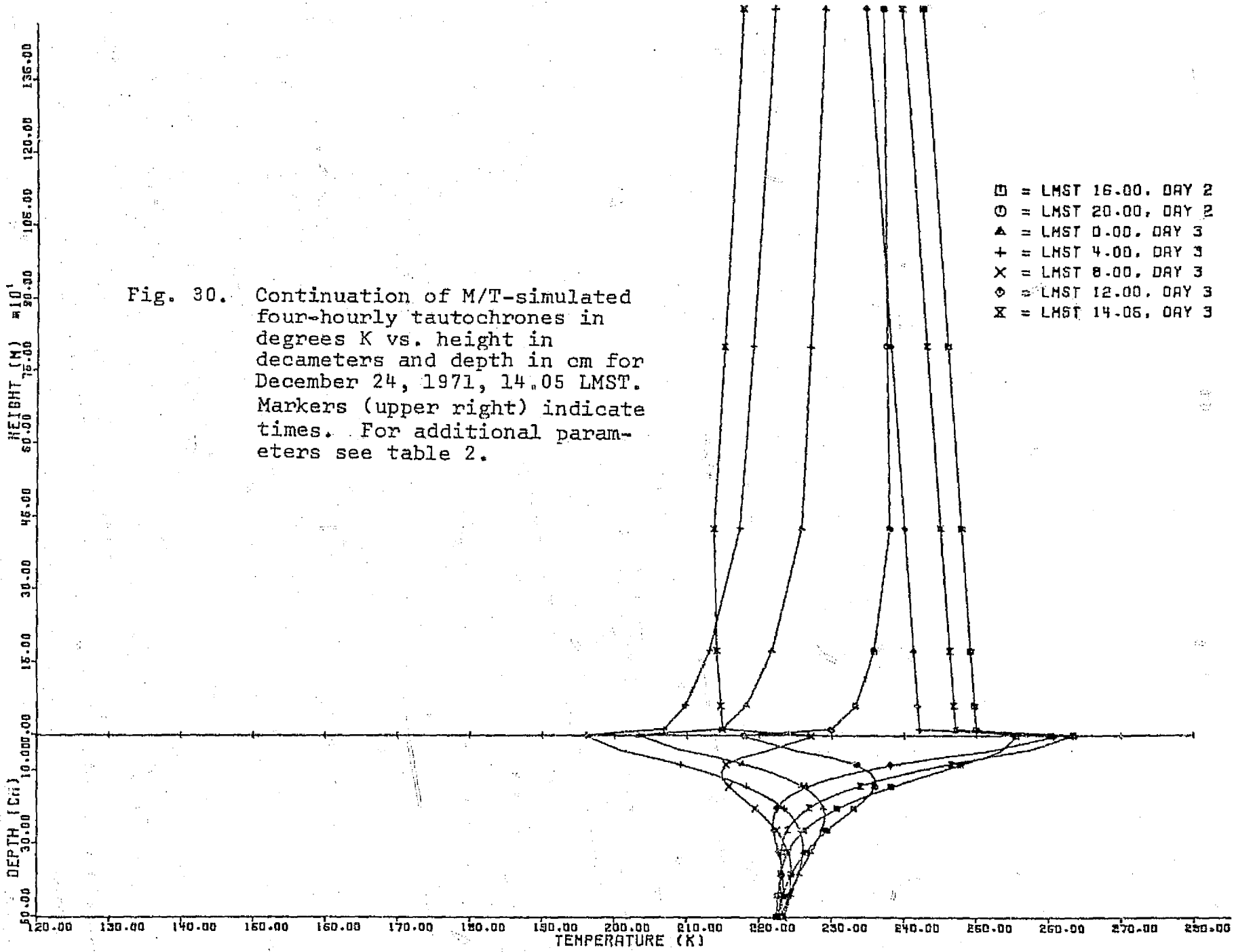

Fig. 30. Continuation of M/T-simulated four-hourly tautochrones in degrees K vs. height in decameters and depth in cm for December 24, 1971, 14.05 LMST. Markers (upper right) indicate times. For additional parameters see table 2.

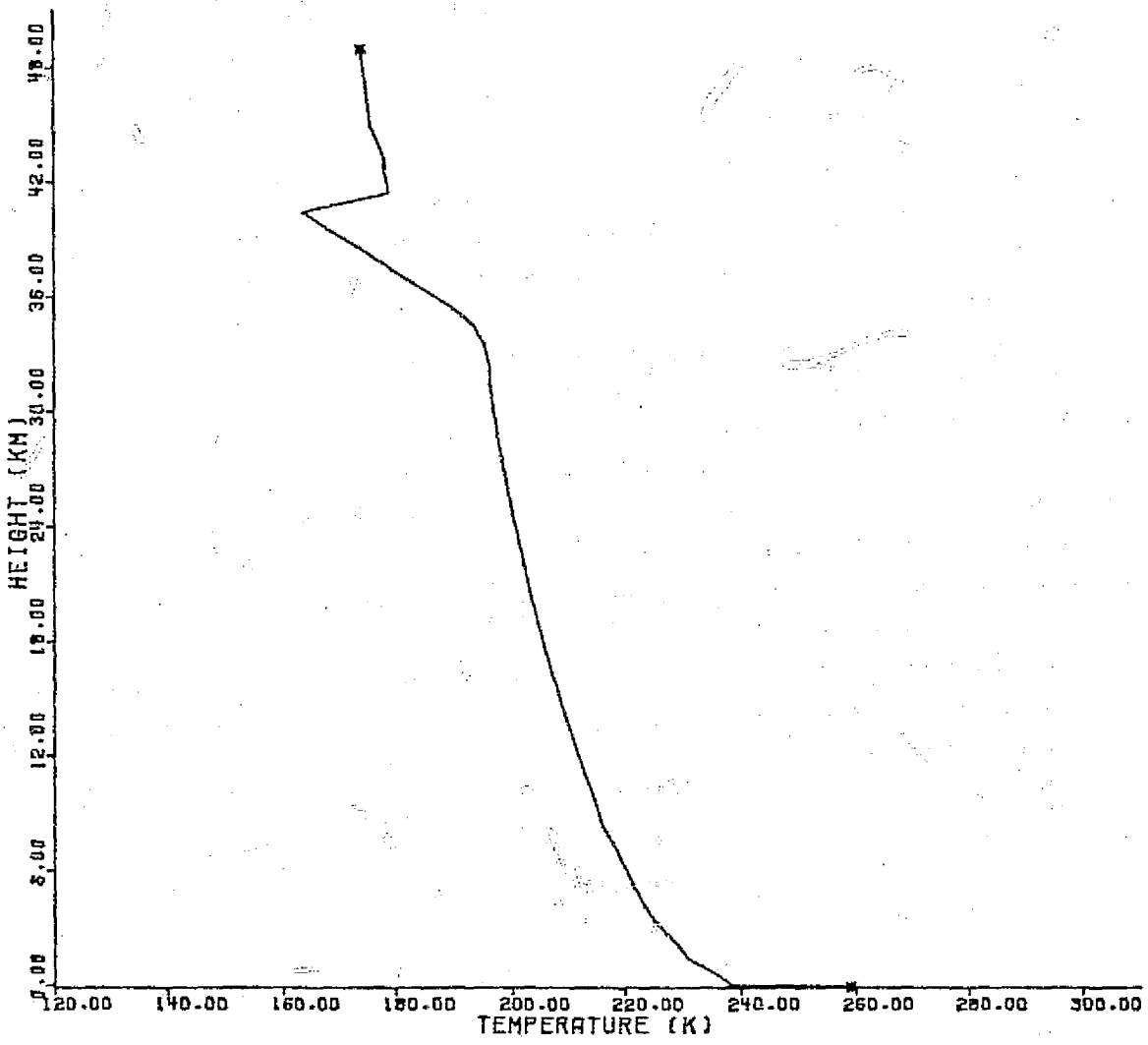

Fig. 31. Cyclically balanced temperature sounding vs. height, in simulation for November 22, 1971, 9.52 LMST, as input to the F/O program. For additional parameters, see table 3.

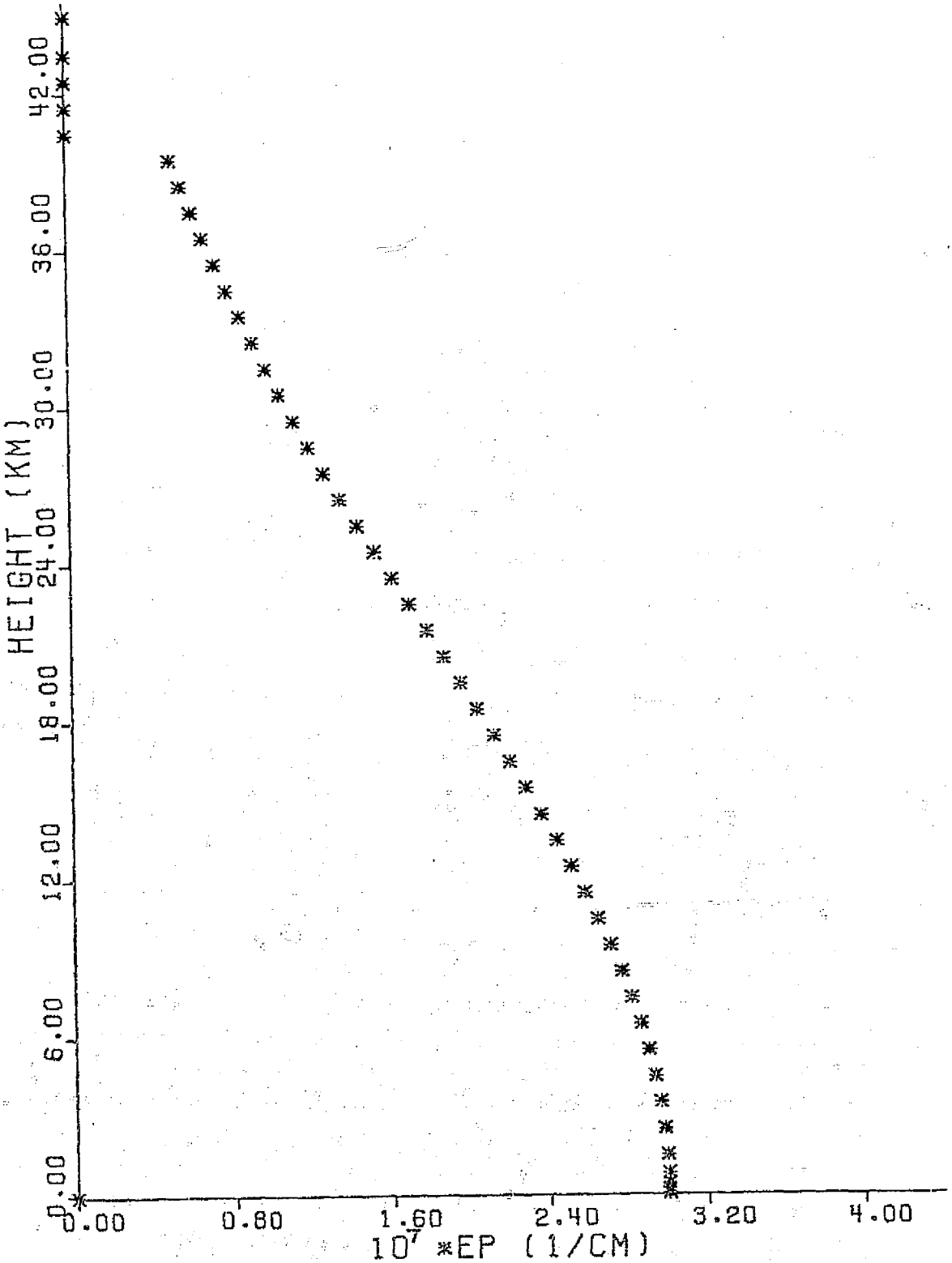

Fig. 32. Effective dust absorption coefficient in 10^{-7} cm^{-1} vs. height in km. for November 22, 1971, 9.52 LMST. Top of the dust layer located at 40 km. For additional parameters, see table 3.

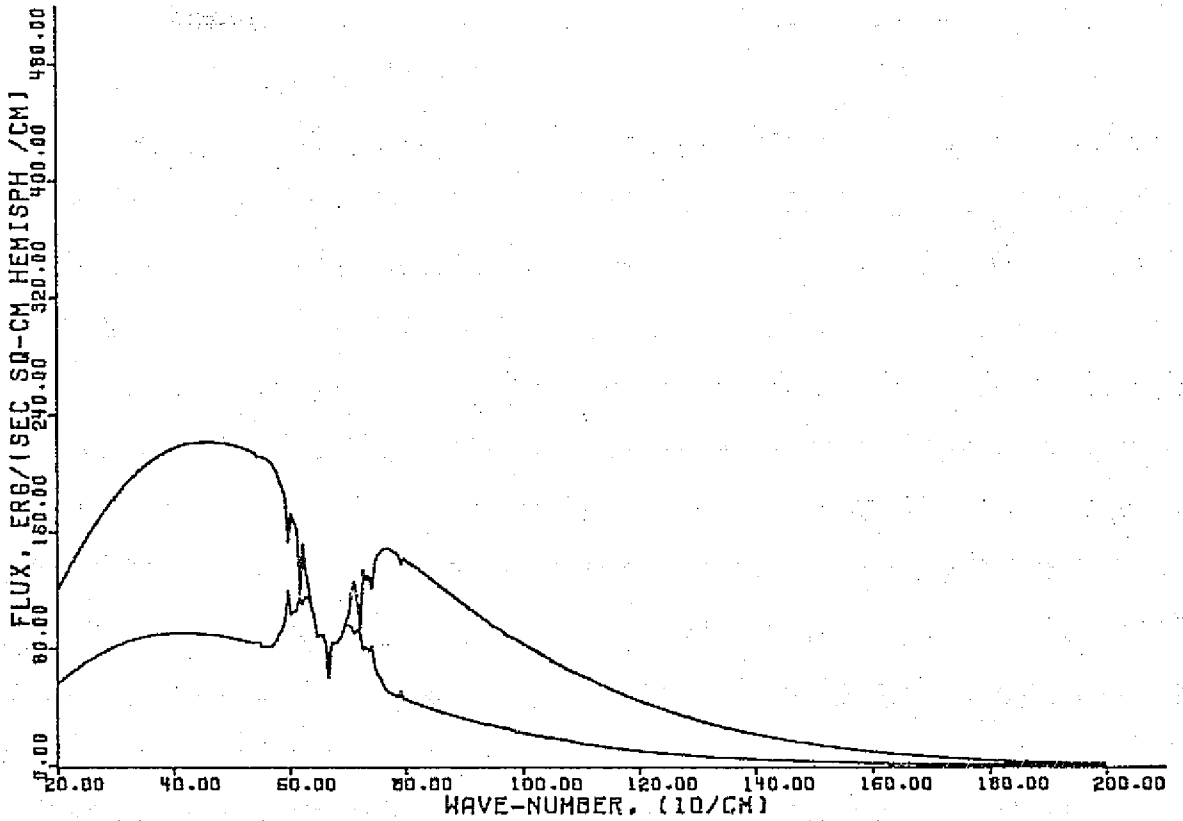

Fig. 33. F/O-simulated upwelling flux in ergs/(sec cm^{-2} hemisph/cm) vs. wave number in (10/cm) for November 22, 1971, 9.52 LMST. Upper curve: flux from ground and atmosphere combined; lower curve: exclusively atmospheric contribution to flux. For additional parameters, see table 3.

balance over 24 hours is satisfactorily approximated. More details of its structure will be presented in conjunction with the discussion on the 4-hourly soundings over a 2-day period, near the end of this section. In figure 33, the F/O-simulated flux, emitted by ground/atmosphere and subsequently transmitted to its top (upper curve), as well as the strictly atmospheric contribution (lower curve) are depicted as a function of wave-number. The percentual fraction of the atmospheric spectral flux appeared to be doubled when compared with that of December 24, 1971. The difference between the 2 curves, shown in figure 33, is a measure of the ground emission which arrives at the top of the atmosphere. Clearly, near 667 cm^{-1}, no surface emanation reaches the top. The dust-laden CO_2-atmosphere has effectively absorbed all photons near this wave-number.

A comparison between the simulated and measured upwelling fluxes is offered in figure 34. The difference in the levels of the curves outside the CO_2-bands is chiefly related to the difference in surface temperatures T_s. The IRIS-T_s = 238K is more than 20K lower than that of the cyclically balanced sounding. As will be seen in figure 38, the IRIS-inverted temperature sounding is not in cyclical balance. Within the CO_2-bands around 667 cm^{-1}, the simulated flux spectrum shows too low a temperature level. Various interpretations for this phenomenon can be offered. One relates it to the omission of the Doppler shape factor (see sect. 3.3). This shape factor makes a better allowance for gappiness between CO_2 absor-

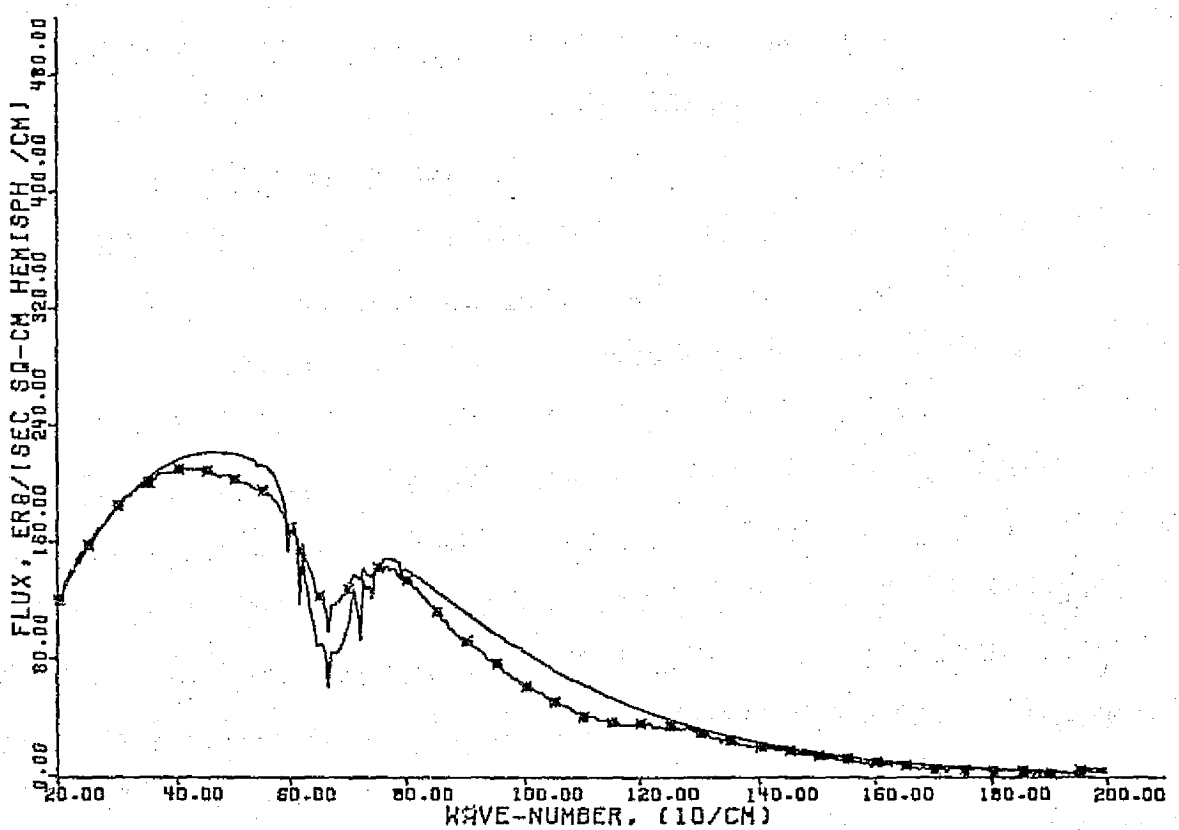

Fig. 34. F/O simulated (solid curve) and IRIS-measured (*) upwelling flux, in ergs/(sec cm^2 hemisph/cm) vs. wave number in (10/cm) for November 22, 1971, 9.52 LMST. For additional parameters, see table 3.

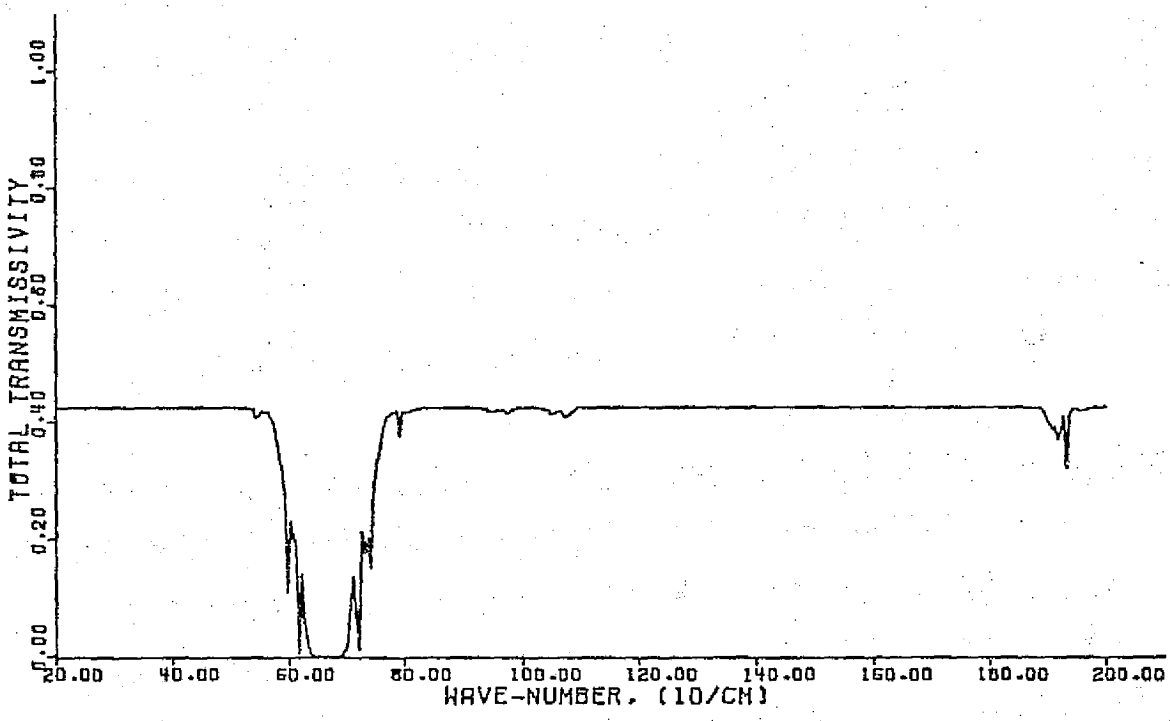

Fig. 35. Spectral transmissivity, for the entire depth of the atmosphere, vs. wave number in (10/cm) for November 22, 1971, 9.52 LMST. For additional parameters, see table 3.

ption lines. Wider spectral gaps permit a larger number of IR-photons from lower, therefore warmer, regions to leave the atmosphere. This intensified transmission would lead to a lift of the simulated flux curve within the CO_2 bands.

Another interpretation makes reference to a study of terrestrial mesopheric dust granule temperatures by Fiocco et alii (1975) who deduced dust temperatures (up to 100K) higher than the ambient temperature. If a similar condition exists on Mars we would be dealing with hotter particulate emitters embedded in a colder environment. This would generate an enhanced emission measurable as a higher upward flux value.

The spectral transmissivity for the total depth of the atmosphere (50 km) is depicted in figure 35 as a function of wave-number. A total opacity from 640 to 690 cm^{-1} is again discernible. Outside the CO_2- bands, about 42 % of the IR-radiation from the ground arrives at the top of the atmosphere. Minor vacillations near 1,000 and 1,920 cm^{-1} stem from CO_2-absorption.

In the remaining paragraphs of section 7.3, M/T-simulated time-dependent outputs will be discussed. The adopted values of the program parameters are shown in Table 3. The time evolution of the atmospheric temperature stratification over 48 hours has been plotted in figures 36 and 37. The sequence of 4-hourly temperature soundings starts with the IRIS-inverted T-sounding whose surface temperature was set to T_s = 238K. Its temperatures between 15 and 30 km remain the lowest over the entire period of time integration. This suggests

TABLE 3

NOVEMBER 22, 1971

MARTIAN ATMOSPHERE RAD-COND-CONV HEAT TRANSFER SIMULATION

PROGRAM PARAMETERS:

INITIAL TIME	9.520 LOCAL MARTIAN SOLAR TIME
NUMBER OF TIMESTEPS	300
TIMESTEP INTERVAL	10.000 MINUTES (MARTIAN)
	4.000 MINUTES (MARTIAN) FROM 13.50 TO 16.50
SURFACE ALBEDO	.300
SOIL DENSITY	1.500 GR/CU-CM
SOIL CONDUCTIVITY	2.300E 04 ERGS/(SEC CM DEG)
SOIL HEAT CAPACITY	1.005E 07 ERGS/(CU-CM DEG)
CO2 CONDUCTIVITY	1.330E 43 ERGS/(SEC CM DEG)
LATITUDE	-40.10 DEG
DECLINATION OF SUN	-21.90 DEG
DURATION OF SUNSHINE	878.1 MINUTES (MARTIAN)
RATIO OF MEAN/ACTUAL.	
SOLAR DISTANCE	1.0737
SURFACE PRESSURE	5.3 MB
DUST AMPLITUDE	3.000E-07 /CM

ONE MARTIAN SOLAR DAY = 24 MARTIAN HOURS = 1440 MARTIAN MINUTES

ONE MARTIAN MINUTE = 61.6625 SECONDS

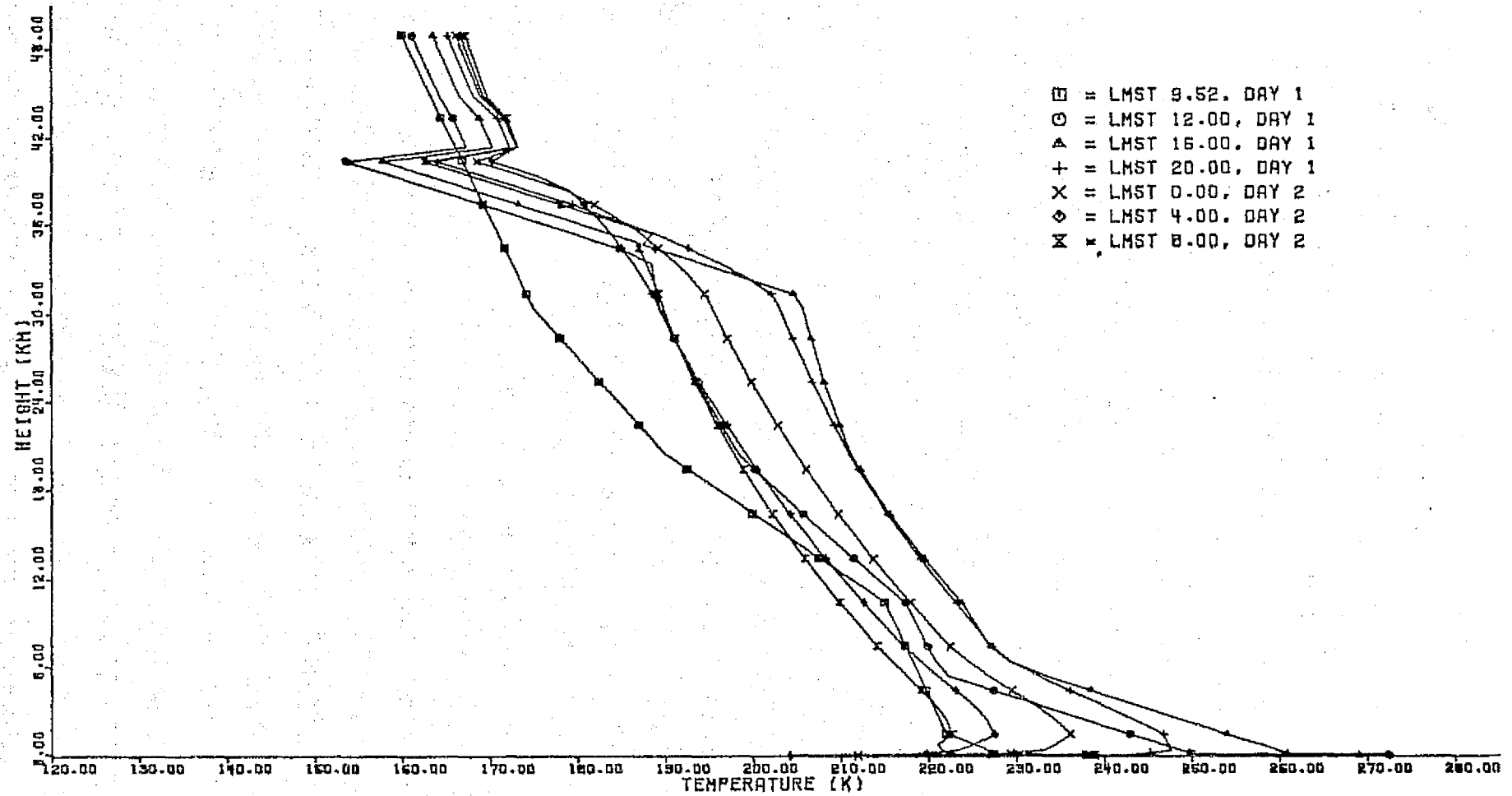

Fig. 36. M/T-simulated four-hourly atmospheric temperature soundings in degree K vs. height in km for November 22, 1971, 9.52 LMST. Sequence of 24 hours begins with IRIS-inverted sounding and proceeds as indicated by markers (upper right). For additional parameters, see table 3.

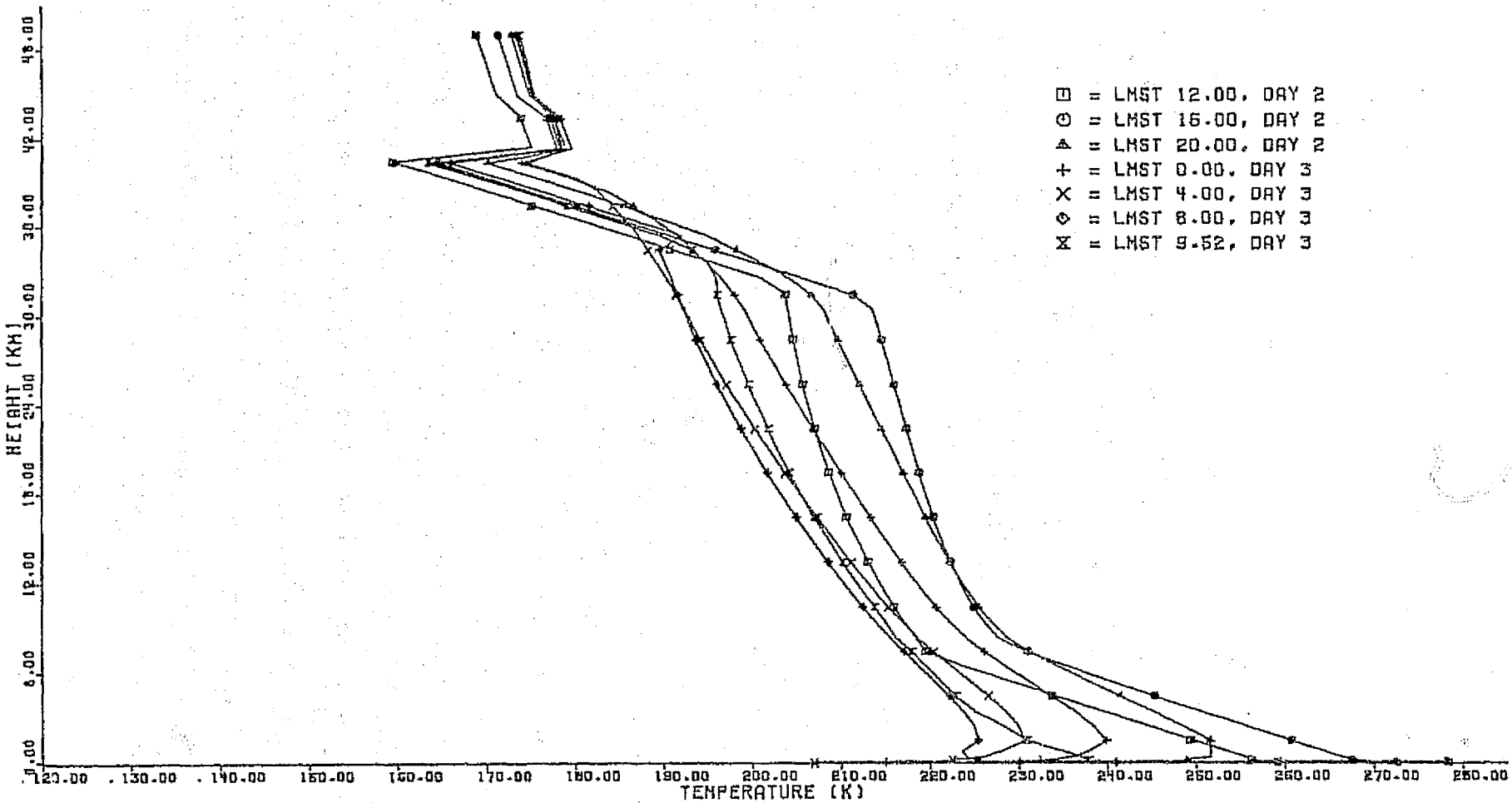

Fig. 37. Continuation of M/T-simulated four-hourly atmospheric temperature soundings in degrees K vs. height in km for November 22, 1971, 9.52 LMST. Sequence of 24 hours begins with IRIS-inverted sounding and proceeds as indicated by markers (upper right). For additional parameters, see table 3.

that radiative heat transfer mechanisms maintain in this layer temperature levels incresed by up to 30K. Above and below this layer, additional heat transport accurs by means of convective overturn, characterized by the adiabatic lapse rate of 5.2K/km (straight lines slanting from the upper left to the lower right).

Again, temperature inversions are discernible in the lowest atmosphere around sunrise, and above the dust-layer top (at 40 km) with variable strength over the diurnal cycle. In figure 37, the approach toward the cyclical balance may be recognized. Diurnal temperature ranges are the following:

- at the surface, about 71K;
- in the lowest 2 km, about 40K;
- at the top of the planeatry boundary layer, about 15K;
- near 30 km, about 22K; and
- in the uppermost atmospheric layer above the dust, about 6K.

If a comparison is made between these simulated temperature characteristics and the S-band occultation soundings of temperature, it is apparent that similar basic features exist in the occultation data. For instance, the S.H. midlatitudinal occultation temperature profile of revolution 17 (Kliore et alii, 1972; fig. VI-3) shows a temperature minimum of about 160K at Martian radius 3,418 km, with a quasi-adiabatic stratification, several km deep, below this level. Furthermore, the lapse rate of the occultation profile in the lowest kilometers appears to be quasi-adiabatic, whereas the rate of

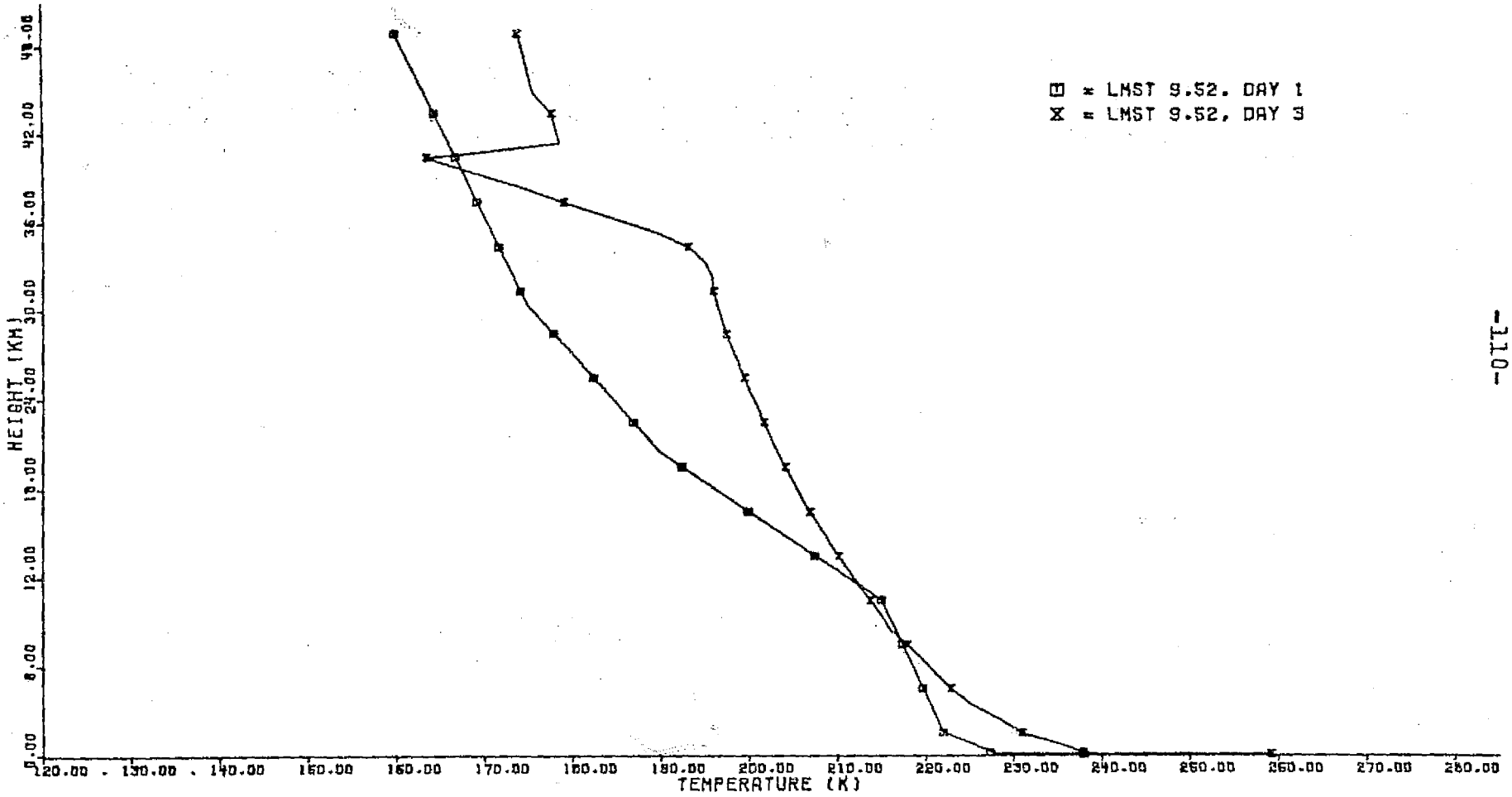

Fig. 38. Initial and final soundings from the 48 hour M/T simulation, in degrees K vs. height in km, for November 22, 1971, 9.52 LMST. Markers (upper right) specify the times. For additional parameters, see table 3.

temperature change in the intermediate layers is just a small fraction of the adiabatic lapse rate.

This coincidence of some features in the simulation and occultation soundings appears to be repeated for profiles of revolution 1, 3, 7, and 15 (Kliore's fig. VI-2). Although it is recognized that the occultation data are noisier, in principal they have a higher vertical resolution than IRIS-inverted temperature soundings (see chapter 5 of this report).

In figure 38, the approach toward the cyclical balance is illustrated by showing the initial (IRIS-inverted) and the final (simulation) temperature soundings for the period of 48 hours. It is obvious that a rather large discrepancy exists between 10 and 35 km. This is a consequence of the simulated heating by dust, which is incorporated into the M/T-model. If we assumed that the minimum in the upper portion of the occultation temperature profile is at about 40 km, the profile would follow more closely the final sounding. Conversely, if the height of the dust layer had been simulated at 32 km, the M/T-generated final sounding would have appeared similar to the smoothed occultation sounding.

In figures 39 and 40, the M/T simulated four-hourly tautochrones are depicted for November 22, 1971. The initial sounding at 9.52 LMST is the IRIS-inverted temperature distribution. The higher spatial resolution of the height-scale permits us to discern more easily the near-sunrise thermal inversions up to 1,500 m and the near-noon adiabatic

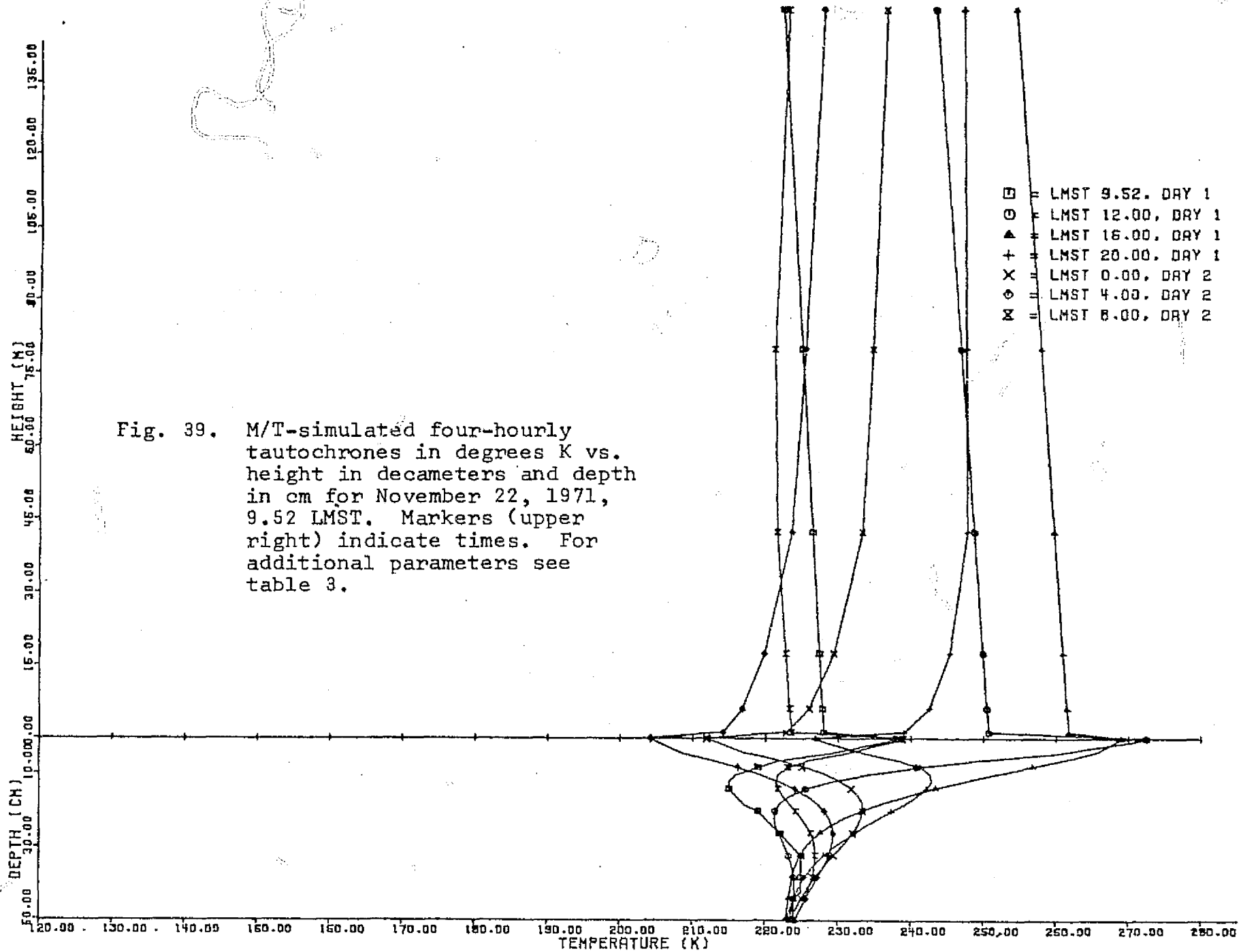

Fig. 39. M/T-simulated four-hourly tautochrones in degrees K vs. height in decameters and depth in cm for November 22, 1971, 9.52 LMST. Markers (upper right) indicate times. For additional parameters see table 3.

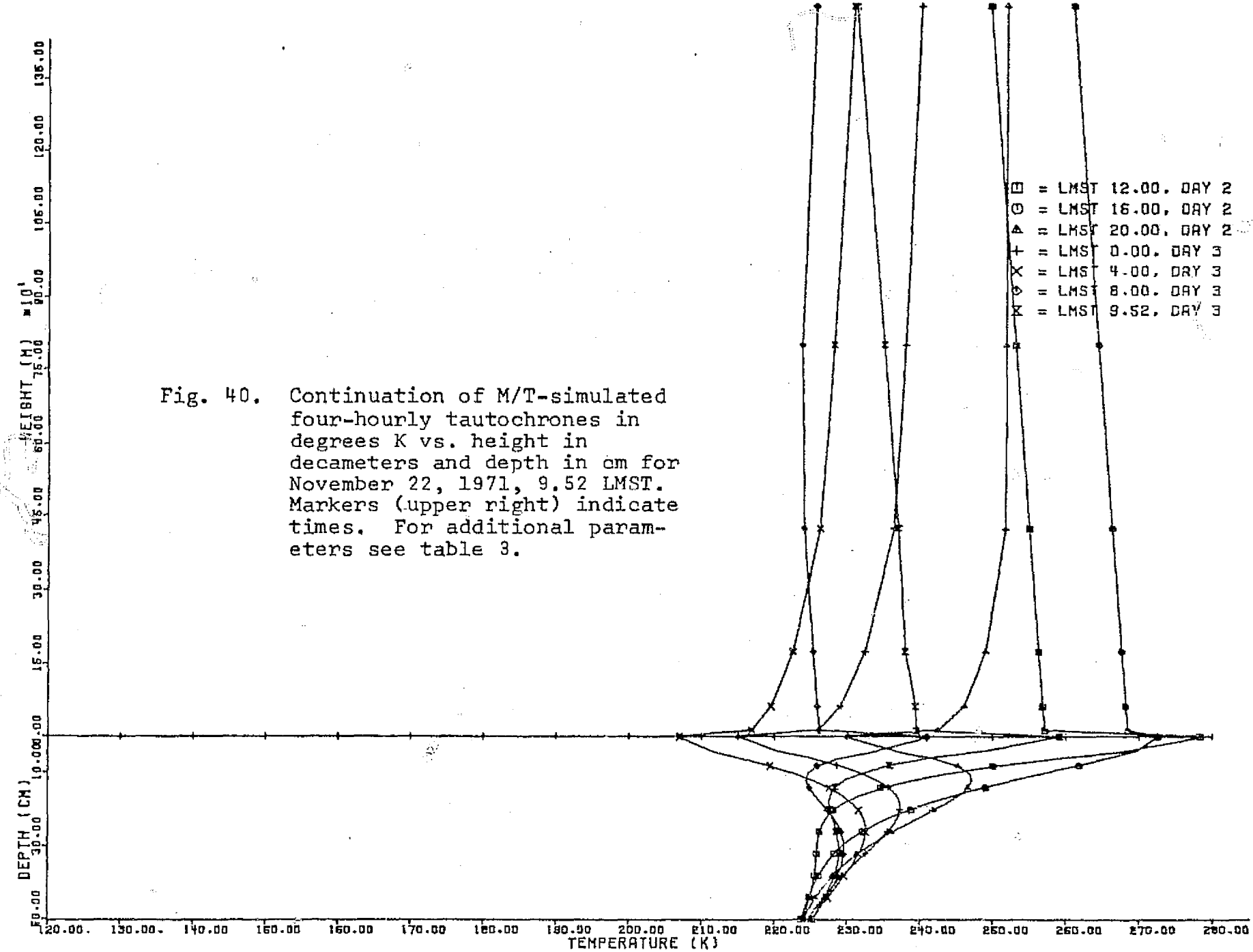

Fig. 40. Continuation of M/T-simulated four-hourly tautochrones in degrees K vs. height in decameters and depth in cm for November 22, 1971, 9.52 LMST. Markers (upper right) indicate times. For additional parameters see table 3.

stratification due to convection. Again, the second simulation day (Fig. 40) illustrates the approach toward cyclical balance with the last sounding at 9.52 LMST of simulation-day 3 being taken to be sufficiently balanced.

The sub-surface temperature variations of simulation day 2 and 3 clearly indicate that changes comparable in magnitude to the range of T_s are limited to the first 10 to 20 cm below the surface. This feature depends on the numerical values chosen for the thermal parameters of the silicate-soil (Table 3). For very steep subsurface temperature gradients, the flux of thermal conduction assumes just below the surface rather large values which are a major fraction of those for the noon insolation. This indicates the heat storage and discharge capability of the Martian soil over the 24-hour cycle. The area embraced by the two tautochrones with highest and lowest temperatures may be taken as a measure of the oscillatory heat transports of the soil.

For easier comparison, the initial and final tautochrones are shown in figure 41. The trend toward cyclical balance increased both the atmospheric and soil temperatures by more than 10K almost everywhere. The tautochrones of figure 41, taken together with the soundings of figure 38, delineate the temperature distributions of the ground-atmosphere for cyclically balanced and unbalanced conditions.

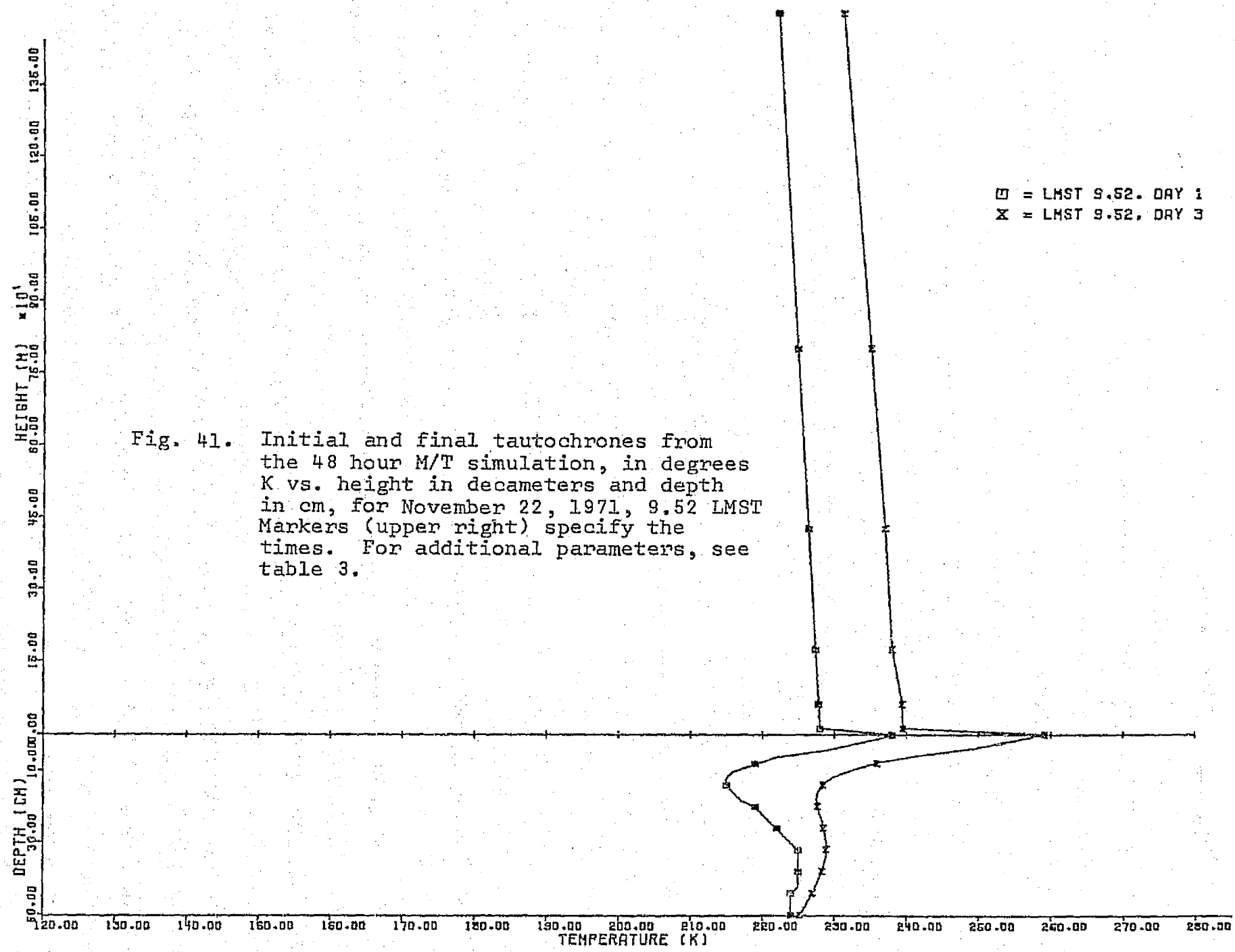

Fig. 41. Initial and final tautochrones from the 48 hour M/T simulation, in degrees K vs. height in decameters and depth in cm, for November 22, 1971, 9.52 LMST Markers (upper right) specify the times. For additional parameters, see table 3.

8.0 SUMMARY OF FINDINGS

The attunement of the refined model to IRIS, IRR and S-band occultation data facilitated the creation of a broad spectrum of outputs (chapter 7) which has been serving as an information pool for interpretation. With respect to the atmospheric dust-load, it permitted us to generate inferences into the representativeness of IRIS-inverted temperature soundings, the significance of IR-radiometric brightness temperatures, and the usefulness of S-band occultation data.

The underlying principle for our time-dependent heat transport simulation was that atmospheric and soil temperature fields are the result of free exchange of heat through radiative, convective and conductive transfers. In this context, advection was not explicitly modeled into our program. If given sufficient time, the temperature fields generated by the R.C.C.T. model will tend to approximate a balance over the 24-hour cycle.

In the following paragraphs, some of the more basic findings of the data-attuned simulation effort are given:

1) In the dust-free atmosphere, a very close attunement of the combined M/T-F/O-model is attainable. It is inferred that the cyclically balanced temperature sounding, generated for the dust-free condition, is more representative of the actual thermal field than the IRIS-inverted sounding if

there is no advective interference with the cyclical balance. Conversely, one may conclude, in the presence of advective interferences, deviations from the cyclically balanced sounding are likely to occur.

2) The cyclically balanced temperature sounding basically reveals 3 regimes in the vertical structure of the Martian atmosphere, i.e., (a) a surface boundary layer in which diurnal temperature variations of up to about 70K (at the ground) occur; (b) a planetary boundary layer whose top is determined at about 5 km by intense radiative-convective heat transfer; and (c) the "free" atmosphere with predominantly radiative heat transfer in which diurnal temperature variations are less than 10K.

3) For moderate dust-loads (such as on December 24, 1971), the attunement of the combined M/T-F/0-model is fairly close. It is inferred that the cyclically balanced temperature sounding, generated for this case appears in its detail meteorologically more realistic than the IRIS-inverted sounding if advective interference with the cyclical balance is discarded. Conversely, we may conclude that advection could cause deviation from the cyclical balance.

4) For a dust layer of moderate concentration, the cyclically balanced temperature sounding shows 4 basic thermal regimes in the vertical structure of the

Martian atmosphere, i.e., (a) a surface boundary layer with a diurnal temperature variation of up to 68K (at the ground); (b) two convective-radiative transfer layers, one from 0 to 6 km and the other from the top of the dust layer (40 km) down to 27 km; (c) a layer from 6 to 27 km in which radiative transfer is the controlling transport mechanism; and (d) a rather intense (40K) inversion layer topping the dust layer.

5) For optically-thick dust-loads (November, 1971), the attunement of the combined M/T-F/0-model is fair enough to serve as a basis from which to infer. We find again that because of its higher vertical resolution the cyclically balanced temperature sounding is meteorologically more representative than the IRIS-inverted sounding unless advective heat transport interfere. Conversely, it may be concluded that, in the presence of effective advection, deviations from the balanced sounding are to be expected.

6) For an optically-thick dust layer with a diurnally balanced thermal cycle, the generated sounding indicates again 4 basic regimes in the vertical atmospheric structure, i.e., (a) a surface boundary layer with a diurnal temperature variation of up to 72K (at the ground); (b) two convective-radiative layers, one from 0-8 km and the other from the top of the dust layer (40 km) down to about 32 km; (c) a layer from 8- 32 km with radiative

transfer dominating the heat exchange and causing diurnal temperature variations of at least 15K; (d) a rather steep inversion layer of between 6 and 18 K temperature increase topping the dust layer.

7) The Martian dust particulates appear to be rather effective absorbers with a likely complex index of refraction $m = 1.55 - i\,(0.0465 \pm 0.0155)$ for the visible range.

8) The diurnal history of the cyclically balanced temperature sounding does permit us to re-interpret the IR- radiometric (IRR) brightness temperature. As an example: on November 22, 1971, 9.52 LMST, the averaged IRR-temperature was 234.7K whereas the balanced surface temperature showed $T_s = 259K$. In our sounding, the value 234.7K was reached at an elevation of about 800 m.

9) In spite of its inherent noisiness, the S-band occultation data confirm some of the features in the vertical temperature structure, as generated by our simulation. Conversely, our cyclically balanced T-soundings may be used to adjust occultation temperature soundings.

REFERENCES

Andres, R. M., 1971: The Mechanics of Dust Lifting with Particular Emphasis on the Planet Mars. Unpublished Dissertation, Saint Louis University, Ann Arbor Microfilm Center.

Atroshenko, V. S. et alii, 1963: Calculation of the Brightness of Light in the Case of Aniso Tropic Scattering. Part 2. Trudy, Inst. of Atmosph. Phys. #3. Engl. Ed. Consultants Bureau, New York, 226 pp.

Braslau, N. and J. V. Dave, 1973a: Effects of Aerosols on the Transfer of Solar Energy through Realistic Model Atmospheres. Part I: Non-Absorbing Aerosols. J. Applied Meteorology, 12, 601-615.

- - - - - - - - - - - - - - - , 1973b: Effects of Aerosols on the Transfer of Solar Energy through Realistic Model Atmospheres. Part II: Partly-Absorbing Aerosols. J. Applied Meteorology, 12, 616-619.

Canosa, J. and H. R. Pinafiel, 1973: A Direct Solution of the Radiative Transfer Equation: Applied to Rayleigh and Mie Atmospheres. J. Quant. Spectros. Rad. T. 13, 21-39.

Carnahan, B., H. A. Luther, and J. O. Wilkes, 1969: Applied Numerical Methods. New York, Wiley and Sons, Inc., pp. 604.

Chandrasekhar, S., 1960: Radiative Transfer. New York, Dover Publications, Inc., pp. 393.

Chapman, S. and T. G. Cowling, 1970: The Mathematical Theory of Non-Uniform Gases, 3rd. ed., Cambridge Univ. Press, pp. 423.

Chase, S. C. et alii, 1972: Infrared Radiometry Experiment. Mariner Mars 1971 Project Final Report, Vol. II. Preliminary Science Results. Jet Propulsion Laboratory, Pasadena, California.

Chase, S. C. et alii, 1973: Infrared Radiometry Experiment. J.P.L. Techn. Rep. 32-1550, Vol. V., 37-40.

Conrath, B. J., 1972: Vertical Resolution of Temperature Profiles Obtained from Remote Radiation Measurements, J.A.S., 29, 1262-1271.

Conrath, B. J., 1974a: Thermal Structure of the Martian Atmosphere During the Dissipation of the Dust Storm of 1971. NASA Goddard Space Flight Center, x-622-74-111. Greenbelt, Maryland. 33 pp.

- - - - - - - - , 1974b: Special Communication Involving the Plot: Vertical Resolution for Martian T-Profile Inversion. (9/18/74).

- - - - - - - - , 1975: Thermal Structure of the Martian Atmosphere during the Dissipation of the Dust Storm of 1971. Icarus, 24, 36-44.

- - - - - - - - et alii, 1973: Atmosphere and Surface Properties of Mars Obtained by T. R. Spectroscopy on Mariner 9. Mariner Mars 1971 Project Final Report, Vol. IV: Science Results, Jet Propulsion Laboratory, Pasadena, California.

Dannevik, W. P. and A. J. Pallmann, 1974: Mariner-9-Based Simulation of Radiative-Convective-Temperature Changes in the Martian Dust-laden Atmosphere-Soil System. Rivista Ital. di Geofisica XXIII, 3/4, 201-206.

Dave, J. V., 1970: Coefficients of the Legendre and Fourier Series for the Scattering Functions of Spherical Particles. Applied Optics, 9; #8, 1888-96.

- - - - - -, 1975a: A Direct Solution of the Spherical Harmonic Approximation to the Radiative Transfer Equation for an Arbitrary Solar Elevation. Part I: Theory. J. Atmosp. Sci., 32, 790-798

- - - - - -, 1975b: A Direct Solution of the Spherical Harmonics Approximation to the Radiative Transfer Equation for an Arbitrary Solar Elevation. J. Atmosp. Sci., 32, 7, 1463-74.

- - - - - - - - and B. H. Armstrong, 1974: Smoothing of the Intensity Curve Obtained from a Solution of the Spherical Harmonics Approximation to the Transfer Equation. J. Atmosph. Sci., 31, 7; 1934-37

- - - - - - - - and J. Canosa, 1974: A Direct Solution of the Radiative Transfer Equation: Application to Atmospheric Models with Arbitrary Vertical Non-homogeneities. J. Atmosp. Sci., 31, 1089-1101.

Ely, R. and T. K. McCubbin, 1970: Appl. Opt. 9, 5; 1230.

Fiocco, G. et alii, 1975: Equilibrium Temperature of Small Particles in the Upper Atmosphere (50-100 km). J. Atmos. Terr. Phys.

Geiger, R., 1966: The Climate Near the Ground. Cambridge, Mass. Harvard Univ. Pr., pp. 611.

Gierasch, P. J., and R. M. Goody, 1973: A Model of a Martian Great Dust Storm. J. Atmosp. Sci., 30, 169-179.

Godson, W. L., 1954: Spectral Models and the Properties of Transmission Functions. Proceedings Toronto Meteor. Conf. (Royal Meteor. Soc.) 1953; p. 35.

Goody, R. M., 1964: Atmospheric Radiation. Oxford, England. At the Clarendon Press, pp. 436

- - - - - - , and P. Gierasch, 1974: The Influence of Vorticity on Free Convection. J. Atmosph. Sci., 31, 4, 1021-1027.

Hanel, R. A. et alii, 1972: Infrared Radiometry Experiment. Mariner Mars 1971 Project Final Report, Vol. II. Preliminary Science Results. Jet Propulsion Laboratory, Pasadena, California.

- - - - - - - - - - - , 1973: Infrared Radiometry Experiment. Mariner Mars 1971 Final Project Report, Vol. V. Science Experiment Reports. Jet Propulsion Laboratory, Pasadena, California.

Howard, J. N. et alii, 1961: Thermal Radiation. Handbook of Geophysics, rev. ed., New York, MacMillan, Chpt. 16.

Kieffer, H. H. et alii, 1973: Preliminary Report on Infrared Radiometric Measurements from Mariner 9. From Techn. Rep. 32-1550; Vol IV of Mariner Mars 1971 Project Final Report, Pasadena, Calif., 315-38.

Kielkopf, J. F., 1973: New Approximation to the Voigt Function with Applications to Spectral Line Profile Analysis. J. Opt. Soc. Am., 3, 987-995.

Klerer, M. and G. A. Korn (eds.), 1967: Digital Computer User's Handbook. New York, McGraw-Hill.

Kliore, A. J., et alii, 1972: S-Band Occultation Experiment: Atmosphere, Ionosphere and Topography of Mars. Mariner Mars 1971 Project Final Report Vol. II. Preliminary Science Results. Jet Propulsion Laboratory, Pasadena, California.

Kliore, A. J. et alii, 1973a: S-Band Radio Occultation Measurements of the Atmosphere and Topography of Mars with Mariner 9: Extended Mission. J.P.C. Techn. Rep. 32-1550. Vol. IV, 473-494.

- - - - - - - et alii, 1973b: S-Band Occultation Experiment: A Summary. J.P.C. Techn. Rep. 32-1550. Vol. V, 33-36.

Kondrat'yev, K. Ya, 1969: Radiation in the Atmosphere. New York, Academic Press, 912 pp.

Kourgauoff, V., (1952) 1963: Basic Methods in Transfer Problems. New York, Dover Publ. Inc., pp. 281.

Kraichnan, R. H., 1962: Turbulent Thermal Convection at Arbitrary Prandtl Number. Physics of Fluids, 5, 1374.

Lewin, W. I. and J. I. Grosberg, 1952: Differential Gleichungen der Math. Physik. Berlin, Verlag Technik. pp. 520.

Marshak, R. E., 1947: Note on the Spherical Harmonic Method as Applied to the Milne Problem for a Sphere. Phys. Review, 71, 443-446.

Martin, L. J., 1974: The Major Martian Yellow Storm of 1971. Icarus, 22, 175-188.

McClatchey, R. A., et alii, 1973: AFCRL Atmospheric Absorption Line Parameters Compilation. Environmental Research Papers No. 434. L. G. Hanscom Field, Bedford, Mass.

Pallmann, A. J., 1974: Reinterpretation of Mariner 9 IRIS Data on the Basis of a Simulation of Radiative-Conductive-Convective Transfer in the Dust-laden Martian Atmosphere. NASA-Grant 26-006-042. PLATMOS-Rept. #9. Saint Louis University, V, 45 pp. with Appendix.

- - - - - - - , et alii, 1973: Martian Thermal Boundary Layers: Subhourly Variations Induced by Radiative-Conductive Heat Transfer within the Dust-Laden Atmosphere-Ground System. NASA Contractor Report, CR-2318.

Pang, K. and C. W. Hord, 1973: Mariner 9 UV Spectrometer Experiment: 1971 Mars' Dust Storm. Icarus, 18, 481-88.

- - - - et alii, 1976: Refractive Index of Martian Dust: Mariner 9 UV Observations and Interpretations. Icarus, 27, in press.

Prabhakara, C. and J. S. Hogan, 1965: Ozone and Carbon Dioxide Heating in the Martian Atmosphere. J. Atmosp. Sci., 22, 97-109.

Rodgers, C. D., 1976: Approximate Methods of Calculating Transmission by Bands of Spectral Lines. Boulder, Colo., NCAR/TN-116 + 1A, 48 pp.

Sagan, C., 1973: Sandstorms and Eolian Erosion on Mars. Mariner Mars 1971 Project Final Report, Vol. IV. Science Results. J.P.L., Pasadena, Calif.

Samuelson, R. E., 1970: Non-Local Thermodynamic Equilibrium in Cloudy Atmospheres. J. Atmosp. Sci., 27, 5, 711-720.

Sekera, Z., 1963a: Multiple Scattering in Media with Anisotropic Scattering: in Electromagnetic Scattering. Proceedings of ICES; New York, Pergamon Press, pp. 547-57.

- - - - - , 1963b: Radiative transfer in a Planetary Atmosphere with Imperfect Scattering. Report, RAND, R-413-PR; pp. 64.

Sobolev, V. V., 1963: Treatise on Radiative Transfer, New York, Van Nostrand Co., pp. 319.

Stull, V. R., P. J. Wyatt and G. N. Plass, 1963: The Infrared Absorption of Carbon Dioxide. Infrared Transmission Studies III. Rept. Contr. SSD-TDR-62-127. Space Systems Division, AF Systems Command, Los Angeles, Calif.

Van de Hulst, H. C., 1957. Light Scattering by Small Particles. New York, J. Wiley and Sons. pp.470.

Technical Reports
- J.P.L. Techn. Rep. 32-1550,
  Vol. II: February 1972; pp.66
  Vol. IV: July 1973; p. 636
  Vol. V: August 1973; pp. 104